Rapidity Dependence of Anti-Particle to Particle Ratios in d+Au Collisions at $\sqrt{s_{NN}} = 200$ GeV

Svein Lindal
University of Oslo
March 7, 2006

Thesis presented for the Cand. Scient. degree (Master of Science).

Acknowledgements

I would like to express my gratitude to my supervisor, Prof. Trine S. Tveter, for keeping my analysis on the right track and for being very helpful in the process of writing this thesis. Big thanks to my other supervisor Prof. Gunnar Løvhøiden and also to Dr. Bjørn Samset for all the help they have provided. My office mate, soon-to-be-Dr Thomas Vik, should be thanked for a good deal of laughs. Thanks to all co-collaborators in the BRAHMS-experiment, and special thanks to all my friends in the Oslo group, for good times and good beer, in Oslo and abroad.

Oslo, March 7, 2006
Svein Lindal

Contents

List of Figures

List of Tables

Chapter 1

Preface

In 1975, using the newly formulated QCD-theory, Perry and Collins [1] predicted the existence of a super dense phase of matter called the *Quark Gluon Plasma*.In the QGP state the quarks and gluons, which are normally confined within a hadron, are liberated and free to roam the volume of the plasma. This form of matter is thought to have existed in the immediate aftermath of the Big Bang and, possibly, in the center of neutron stars. To produce matter in this state one has to be able to create a relatively large volume where the energy density is extremely high. Estimates from calculations predict that the energy density would have to be of the order of $\sim 1 GeV/fm^3$. The matter produced at the extreme energy densities of an ultra-relativistic Heavy Ion Collision is expected to enter the QGP state in very first moments after the collision.

The Relativistic Heavy Ion Collider (RHIC) was constructed with the ambition of producing a sample of this ultra-dense form of matter and to explore its properties. Vast amounts of data has been collected since the startup in 2000. Mostly from collisions between gold nuclei (Au+Au), but also from protons colliding with protons (p+p), deuterons colliding with gold nuclei (d+Au) and, recently, Copper on Copper (Cu+Cu). The main focus has been the bigger system of Au+Au collisions, but the other collision systems have proved to be invaluable as reference systems, helping to establish whether the phenomena observed in Au+Au collisions are unique to this bigger system, or if they are also present in collisions between lighter nuclei where a Quark Gluon Plasma is very unlikely to be produced, in which case they can be disqualified as signatures of matter in the QGP phase.

The data have materialized into hundreds of papers from the four experiments that collect data at RHIC. Whether a quark gluon plasma has been produced or not is still not universally agreed upon. But a majority of the Heavy Ion Physics community seem to be satisfied that the effects observed at RHIC are sufficient evidence that a Quark Gluon Plasma has been produced.

In the first chapter of this dissertation I make a phenomenological description of the Quark Gluon Plasma and the theory behind it. In Chapter two

I establish the terminology and variables used in describing Heavy Ion Collisions and give a phenomenological overview of the collision process with some theoretical predictions regarding particle ratios in a hadron gas. In the *Experimental setup* chapter I give a brief description of the RHIC complex and a more in-depth survey of the BRAHMS detector. I then briefly describe the calibrations that are done to the TPCs before track reconstruction are done. These are described in chapter 5 together with the event characterization and particle identification (PID) process. In chapter 6 describe the general procedure I have followed in order to obtain the ratios from the available data sets. The results and analysis details for specific spectrometer settings are given in chapter 7 with an estimation of the systematic uncertainties. In the final chapter I compare the results from this analysis with rapidity dependent antiparticle to particle ratios measured by BRAHMS in p+p and Au+Au collisions, and PHOBOS ratios from d+Au collisions at midrapidity. I also make a tentative estimation of the system temperature in d+Au collisions compared with Au+Au and p+p collisions, and more generally in big systems compared with smaller systems at various energies.

Chapter 2

Heavy Ion Collisions and the QGP

2.1 Quarks and Gluons

The *Standard Model of Particle Physics* (e.g. [2]) describes the elementary particles of the universe, their properties and interaction. According to this model the building blocks of nuclear matter are quarks and gluons. Quarks are fermions characterized by their $flavor$. The Six known quark-flavors, u (up), d (down), s (strange), c (charm)t (top) and b (bottom) are listed in table 2.1 with their flavor quantum numbers, electrical charges and masses. For each quark-flavor there exists an anti-quark with the corresponding anti-flavor, denoted e.g. $\bar{u}$ (anti-up). The quantum numbers and charges of the quark anti-flavors may be found by switching the signs in table 2.1.

The quark-quark interaction

In addition to the quantum numbers listed in table 2.1 each quark carries either one of three *color-charges*: red, green or blue, while the anti-quarks are anti-red, anti-green or anti-blue. Particles carrying color interact through the strong nuclear force, which is mediated by gluons and is formally described by *Quantum Chromo Dynamics* (*QCD* e.g [4]).

Regardless of its color, a quark can interact with a quark of any color through the exchange of gluons. Gluons are massless bosons, like the photon of the electromagnetic interaction. One important difference, however, is the fact that the gluon carries a color charge of its own. More specifically it carries a non-neutral color anti-color combination. Since the gluons carry color charge, gluons can interact with gluons. This makes the distance dependence of the color-force very different from the distance dependence of the electromagnetic force.The electromagnetic potential $V_{e.m.}(r)$ from an electronic charge as function of distance r, called the *Coulomb potential* is of the form $V_{e.m.} \sim -\frac{\alpha\hbar c}{r}$, with $\alpha \sim 1/137$, which vanishes at large distances. The color potential $V_s(r) \sim -\frac{4}{3}\frac{\alpha_s\hbar c}{r} + kr$ where α_s is a distance dependent factor that is falling off for small distances,

Quark Flavor	Baryon Number	Electrical charge Q	I_z	S	C	B	T	mass (MeV) [3]
u	$\frac{1}{3}$	$\frac{2}{3}$	$\frac{1}{2}$	0	0	0	0	5.6 ± 1.1
d	$\frac{1}{3}$	$-\frac{1}{3}$	-$\frac{1}{2}$	0	0	0	0	9.9 ± 1.1
s	$\frac{1}{3}$	$-\frac{1}{3}$	0	-1	0	0	0	199 ± 33
c	$\frac{1}{3}$	$\frac{2}{3}$	0	0	1	0	0	1350 ± 50
b	$\frac{1}{3}$	$-\frac{1}{3}$	0	0	0	-1	0	$\backsimeq 5000$
t	$\frac{1}{3}$	$\frac{2}{3}$	0	0	0	0	1	> 9000

Table 2.1: The quark flavors and their flavor contents. Q is electrical charge, I_z is the z-component of the /emphIsospin, C is the charm quantum number, S is strangeness and T and B are the top and bottom quantum numbers, respectively. The listed mass of a particle is the /emphcurrent mass of the particles, which is the mass in the absence of *confinement* (defined below)

typically $\alpha_s \sim 0.1 - 0.3$, and $k \sim 0.16 GeV^2/\hbar c$. At small distances this is proportional to $1/r$ like the Coulomb potential of the electromagnetic interaction. At large distances the second term kicks in and the potential increases linearly with increasing distance. The dependence of the color potential as function of momentum transfer Q (often denoted Q^2) is shown in figure 2.1 together with lattice QCD calculations of the quark-quark potential as function of distance. Since increasing momentum transfer between probe and target is equivalent to looking at the target with increasing spatial resolution the two are closely related with $\sqrt{Q^2} \sim \frac{1}{r}$.

The linear increase of the color potential with increasing separation means that no particle with color charge can exist freely. They can only exists in color neutral combinations with other particles carrying color charge, this phenomenon is called *confinement* since particles with color charge are confined inside the color field of the particles with which it interacts. No matter how large the distance between a $q\bar{q}$-pair becomes they cannot escape each others color fields. If the energy becomes sufficiently large the pair may break up, but only through the creation of a new $q\bar{q}$-pair, forming an additional color neutral hadron, but no free quarks. This process is illustrated in figure 2.2.

Because of confinement no free quark has ever been detected. All quarks

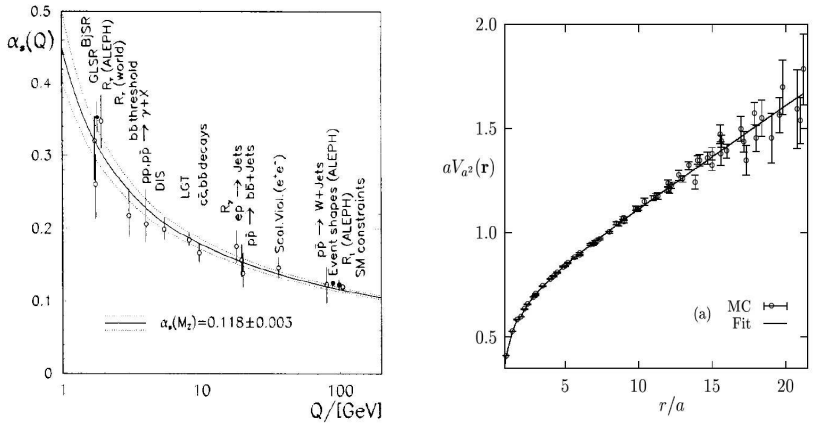

Figure 2.1: Left: Strong coupling constant $\alpha_s(Q)$ as function of momentum transfer Q (usually denoted Q^2) from [5]. Right: Shape of q-q potential as function of separation r calculated from lattice QCD calculations, from [6].

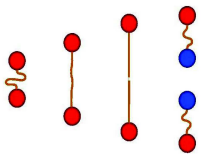

Figure 2.2: A hadron splitting into two hadrons through the creation of a $q\bar{q}$ pair. Figure from [7].

are found in color-neutral combinations with other quarks. In analogy with additive color models of light a color neutral (white) state can be created either by making color anti-color ($q\bar{q}$) combinations (mesons), or by combining three quarks (baryons), each quark of a different color to form a neutral (red+green+blue=white) qqq or $\bar{q}\bar{q}\bar{q}$ state.

Another important feature of the color-field potential is that it decreases asymptotically at very small distances, as may be seen from figure 2.1. This phenomenon is called *asymptotic freedom*, since it implies that the partons of a hadron move like free particles at very small distances. It is this property of the quark-quark potential which led to the theory that, at sufficiently high densities hadronic matter will undergo a transition from a state where the quark-quark potential confines each parton inside the parent hadron, to a deconfined state where the quarks move freely. In this situation the hadrons are squeezed so tightly together, or have such high energies, that the boundaries between them vanish, making the confining potential disappear and each quark is able to roam the entire system independent of its parent hadron. This state of matter is called the *Quark Gluon Plasma* (QGP).

Results from QCD-lattice calculations, shown in figure 2.3, show a sharp increase in the energy density as a function of temperature at a critical temperature $T_c \sim 160MeV$. Such phenomena are signatures of phase transitions where new degrees of freedom are liberated. The QCD phase-transition is caused by the liberation of the quark and gluon degrees of freedom through deconfinement.

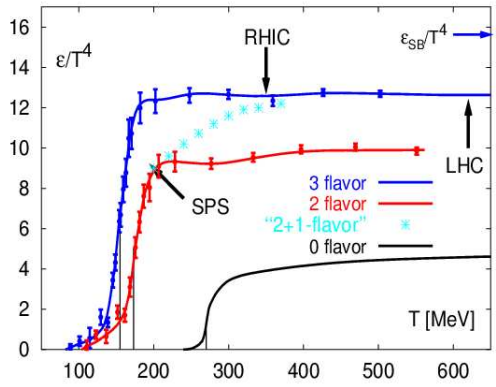

Figure 2.3: Energy density vs temperature from selected QCD lattice calculations. Figure from [7].

2.2 The Phase diagram of matter

Deconfinement can be achieved in two ways: High density or high temperature. Figure 2.4 shows the theoretical phase-diagram of strongly interacting matter in equilibrium. Along the x-axis is the baryochemical potential μ_B which is related to the net baryon density. Along the y-axis is the temperature T. The red lines are the assumed boundaries of a phase, and matter probably has to undergo some sort of phase-transition in order to move from one part to the other. Normal nuclei have a high baryochemical potential and a low temperature. The blue arrows represent the paths in the phase diagram that matter in a relativistic heavy ion collision is thought to follow. They start out as regular nuclei with a high net baryochemical potential and low temperature. The high energy-density caused by the collision leads to high temperatures, while the expansion of the system leads to a lowering of the baryochemical potential. The matter in d+Au collisions, which are not expected to lead to the formation of a quark-gluon plasma, might end up somewhere in the region indicated as a hadron gas, with relatively high energy densities, and a lowered μ_B.

The other phases that are mentioned in the right part of picture are all exotic states of matter that have been predicted to exist by theorists, but which might not be experimentally explorable.

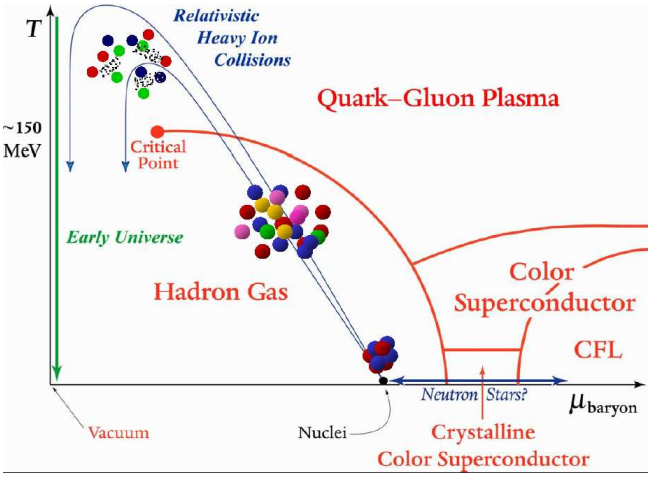

Figure 2.4: The phase-diagram of matter. Figure from [8]

2.3 Ultra-relativistic Heavy Ion Collisions

In experimental studies of Heavy Ion Collisions we cannot observe the collision process directly. What we can observe is the resulting distribution of particles and photons coming out of the collision regions. The chemical composition of the particle yields and shape of the spectra of the various particle types can give information on the processes that govern the production of, and interactions between, particles in the collision region. In this section I will establish terminology and variables that are useful in the description and analysis of Heavy Ion Collisions, before I proceed with a phenomenological description of the collision process.

2.3.1 Variables and terminology

Heavy Ion Collisions are often described in a coordinate system where the z-axis is aligned with the beam-direction. The projection of a variable on this axis is often referred to as the *longitudinal* fraction of the variable. The plane spanned by the $x-$ and $y-$ axes, is called the *transverse* plane. The *impact parameter* b of the collision is the transverse separation between the centers of the two nuclei taken at infinite distance (schematically shown in figure 2.5). It is common to define the x and y axes as the directions parallel and perpendicular to the impact parameter vector, respectively. The xz-plane is often referred to as the *reaction plane*.

Transverse and Longitudinal momentum

When the particles in the beams approach each other along the beam line their momenta are purely longitudinal. This means that any *transverse momentum* p_{T} detected after a collision stems from energy deposited by the colliding nuclei. p_{T} distributions of the various particle types are therefore especially interesting. The transverse momentum p_{T} and *longitudinal momentum* p_{L} are defined by:

$$p_{\mathrm{T}} = \sqrt{p_x^2 + p_y^2}, \qquad p_{\mathrm{L}} = p_z \tag{2.1}$$

Rapidity y

The particles in the beams have energies well into the relativistic region. In the longitudinal direction it is therefore convenient to use a velocity measure that is additive under Lorentz transformation and that doesn't approach c asymptotically. The variable most commonly used is the rapidity y defined by:

$$y = \frac{1}{2}\ln\left(\frac{E + p_{\mathrm{L}}}{E - p_{\mathrm{L}}}\right) = \tanh^{-1}\left(\frac{v_{\mathrm{L}}}{c}\right) \tag{2.2}$$

2.3.2 The Participant Spectator model

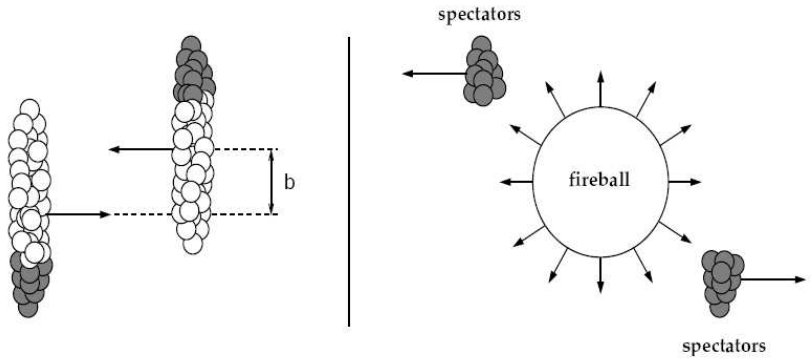

Figure 2.5: A simplistic cartoon of two nuclei immediately before and after a collision at impact parameter b. If the two colliding nuclei have radii R and r the impact parameter b must be smaller than the sum of the two radii for a collision to take place, i.e. $b_{max} = R + r$. Figure from [9].

The participant/spectator model is an attempt at making a simplified phenomenological description of the processes in a heavy ion collision. According to this model the high energies at which the nuclei collide causes their nucleons to be split into two different groups: *Participants*, which are the particles that take part in the collision process, and *Spectators* which are the particles that are situated in the region where the two nuclei do not overlap, they are therefore not involved in the collision. The spectators are expected to continue more or less straight ahead in the beam direction after the collision, while the participants interact and deposit huge quantities of energy in the *interaction region*. In this region the energy density is expected to be very high and the reaction zone is therefore often referred to as the *fireball*.

2.3.3 Centrality

A head-on collision between two heavy ions will be very different from a collision where the two nuclei only have peripheral contact. The centrality of an event is related to the impact parameter b with the most central collisions at $b = 0$. On average decreasing impact parameter will lead to a higher number of participant nucleons and this is expected to result in higher numbers of produced particles, often referred to as higher *multiplicity*. The centrality C of an event with impact parameter b_C is usually given as the percentage of events that will have a smaller impact parameter. The geometrical probability to have a collision with impact parameter b increases proportionally by $2\pi b$ and the centrality of the given event

can be described by:

$$C = \frac{\int_0^{b_C} 2\pi b db}{\sigma_{inel}} \tag{2.3}$$

where σ_{inel} is the total inelastic cross section of nucleus-nucleus collision. Since b cannot be measured directly the centrality is usually estimated through measurements of the number of produced charged particles and/or the number of participants in the collision.

2.3.4 Stopping and Transparency

The degrees of transparency and stopping in a collision reflect the loss of longitudinal momentum suffered by the participant nucleons. High degrees of stopping means that the participants lose a huge fraction of their initial longitudinal momentum through the interactions they undergo with other participants in the initial stages of the collision. In the extreme case of full stopping the participants are more or less completely stopped and all of their initial kinetic energy goes into the fireball, which will have a high net baryon density, since the baryon numbers that were initially put into the fireball must be preserved. A collision process with full stopping is depicted in figure 2.6.

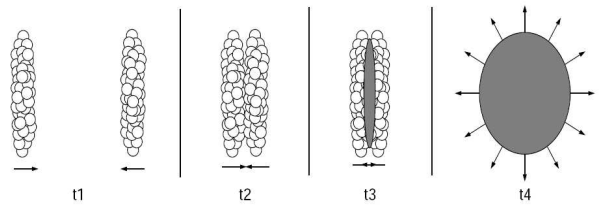

Figure 2.6: Cartoon of collision with a high degree of stopping. The participants are more or less completely stopped and all of their initial energy goes into the fireball. Produced and initial particles then flow out. Figure from [9].

In the case with low stopping the participants pass through the collision region with a large fraction of their initial longitudinal momentum intact, and the collision is said to be *transparent*. There will still be a large energy density left in the collision region in the form of color field strings between quarks in oppositely moving participants. When these strings are stretched too far they break and the energy is released in the form of $q\bar{q}$ pairs. In this scenario the central part of the fireball will be almost entirely made up of particles produced in the collision, with approximately equal amount of quarks and anti-quarks. In the midrapidity region around $y = 0$, the net baryon density will then be close or equal to zero. The baryon numbers of the participant nucleons, which must

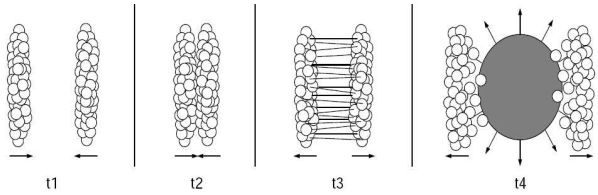

Figure 2.7: Cartoon of collision with low degree of stopping and high degree of transparency. Figure from [9].

still be conserved, may be found in the more forward and backward regions closer to $y = \pm y_{beam}$. Such a scenario is illustrated in figure 2.7.

Since all baryon numbers must be preserved in the collision processes the degree of stopping in a collision can be measured by measuring the rapidity-distribution of the net-baryon content in the fireball. The difference between proton and anti-proton yields is a good indicator of the distribution of net baryon content, since the proton, with quark content uud, consists solely of quarks that may be found in the nucleons of the colliding nuclei (protons and neutrons (udd)), while the anti-proton, with quark content $\bar{u}\bar{u}\bar{d}$, consists of quarks which must all be produced in the collision. Any excess of protons compared with anti-protons in a region of phase-space must arise from the transportation of baryon numbers from the beam rapidities to the given region. In a transparent collision the net proton distribution is therefore expected to have a rapidity dependent distribution with low net proton content at midrapidity and higher contents at $y \approx \pm y_{beam}$.

2.3.5 Measurements of stopping at RHIC and SPS

Results from Au+Au collisions at RHIC have shown that the energies there are sufficient to make the nuclei quite transparent. Figure 2.8 shows a plot of the net proton density as function of y for different center of mass energies $\sqrt{s_{NN}}$. For $\sqrt{s_{NN}} \sim 5$ GeV the proton density has its peak at zero rapidity. At higher $\sqrt{s_{NN}}$ there is a dip in the net baryon density at mid-rapidity with peaks closer to the beam-rapidities, indicating a hight content of light quarks from the original nuclei, often referred to as the *fragmentation peaks*.

At fixed $\sqrt{s_{NN}}$ the degree of stopping depends on system size and centrality. Figure 2.9 shows the projectile component of the net proton distribution as function of x_F (related to longitudinal momentum, see figure caption for details) for different systems and centrality selections. The left panel shows net protons from p+p and p+Pb collisions with the latter divided into two centrality selections based on the average number of collisions undergone by participant nucleons $\langle\nu\rangle$, with $\langle\nu\rangle$= 3.1 and $\langle\nu\rangle$= 3.6. The right panel compares N+N

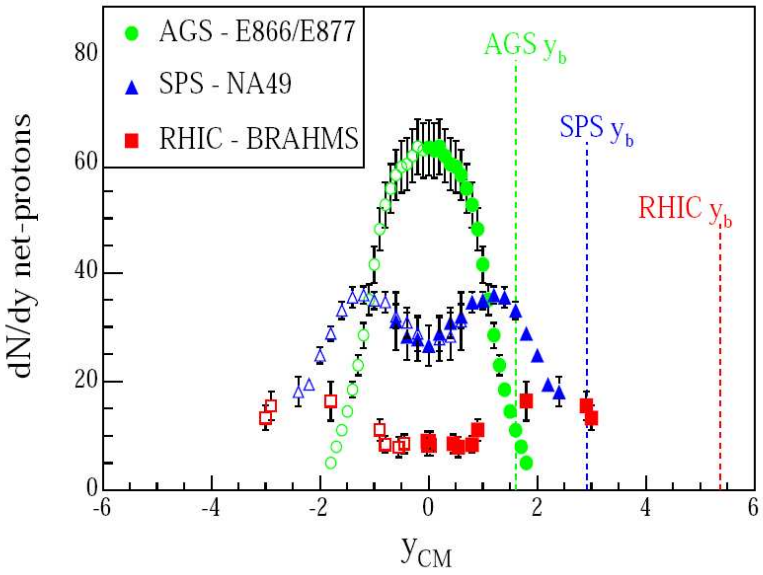

Figure 2.8: Net proton distribution as function of rapidity in Au+Au collisions at $\sqrt{s_{NN}} = 5$ GeV(AGS), Pb+Pb at $\sqrt{s_{NN}} = 17$ GeV(SPS) and Au+Au at $\sqrt{s_{NN}} = 200$ GeV(BRAHMS). Figure from [10].

collisions (isospin weighted) with Pb+Pb collisions at 3 different centralities. It is seen that the net proton component on average is shifted to significantly lower x_F in p+Pb than in Pb+Pb. This occurs because the average number of collisions suffered by the small-nuclei participants in collisions between a small and a large nucleus is larger than for participants in collisions where both nuclei are equally massive, since the small projectile has to penetrate a thick part of the massive nucleus for a range of impact parameters, while full overlap between massive nuclei is only obtained for $b = 0$, and even in this case there will be projectile participants situated in the periphery of the collision region, colliding with the dilute surface region of the target.

The p+p (N+N) net proton distribution indicates a smaller degree of stopping than is the case in p+Pb and Pb+Pb, which is expected since only one collision takes place.

At RHIC energies a comparison of the net proton distribution in p+p and Au+Au collisions at $\sqrt{s_{NN}} = 200$ GeV indicates that the rapidity loss $\Delta y = y_{beam} - \langle y \rangle_{net\ baryon}$ is ~ 1 unit smaller for the elementary collisions [11]. The trend from lower energies predict a projectile rapidity loss for d+Au even greater than in Au+Au. This is confirmed by STAR measurements of baryons at midrapidity and forward rapidity [12] shown in figure 2.10. The rapidity loss in central and semi-central d+Au collisions is significantly higher than in central Au+Au collisions as measured by BRAHMS [10].

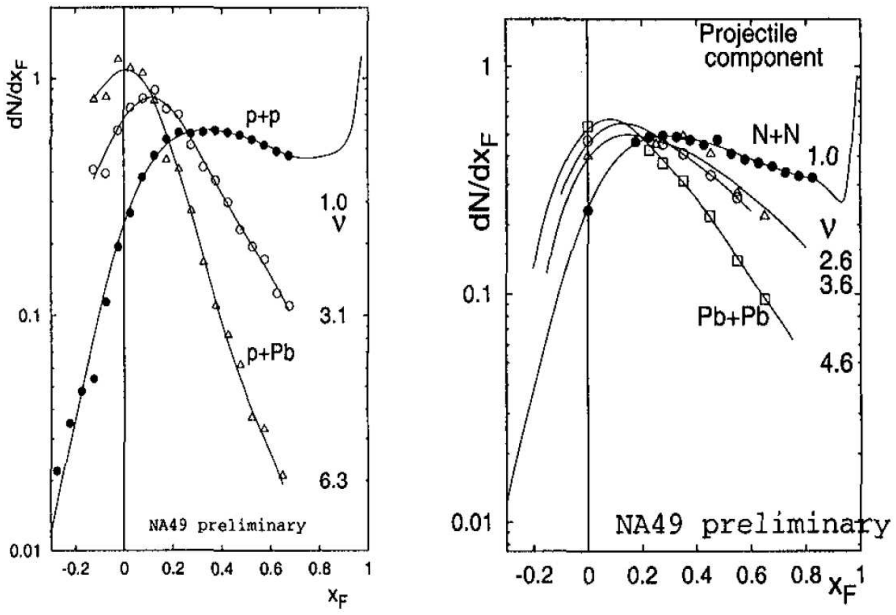

Figure 2.9: Net proton x_F distributions of projectile components in p+p and p+Pb collisions, and Pb+Pb and N+N collisions (right). x_F is defined as $\frac{p_L^*}{p_{max}^*}$ where p_{L}^* is the longitudinal momentum of a detected particle, while $p_{max}^* \approx p_{beam}$ is the maximum momentum achievable, with both momentum variables defined in the center of mass system. The variable $\langle\nu\rangle$ is the average number of binary collisions undergone by each projectile nucleon and is centrality dependent. Figures from [13].

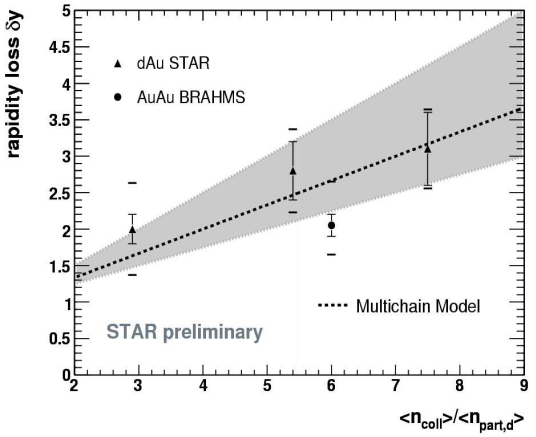

Figure 2.10: STAR measurements of the rapidity loss of deuteron-side participants in d+Au collisions as function of the average number of binary collisions by each participant, compared with BRAHMS Au+Au results from [10] and predictions from the multi-chain model. Au+Au points, predictions and figure from [12].

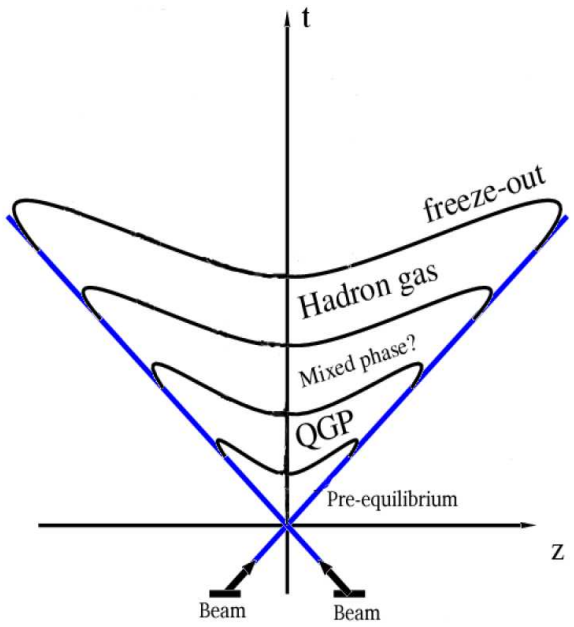

Figure 2.11: The space-time evolution of a Heavy Ion Collision. The nuclei approach each other along the dotted lines, their paths converging at $(z, t) = (0, 0)$.

2.4 Time evolution of a Heavy Ion Collision

Figure 2.11 gives a schematic overview of the space-time evolution of a Heavy Ion Collision in the Bjorken picture where we look at two nuclei approaching each other along the beam lines and colliding at $(t, z) = (0, 0)$. The collision process is thought to undergo different stages, depending on the energy density ϵ in the fireball:

Pre Equilibrium

In the pre-equilibrium stage parton-parton scatterings take place. In this stage high p_{T} jets, heavy quark-antiquark pair production and other effects of high momentum transfers on the partonic level occur. These, together with softer inelastic processes which also cause break-up of the incident nucleons help convert the initial kinetic energy into partonic degrees of freedom [14]. If the energy density is well above the critical energy density ϵ_c the partons are expected to be in the deconfined phase, but may not be in equilibrium. For $\epsilon < \epsilon_c$ the produced particles must be in the confined hadronic state and a hadron gas is produced.

Quark gluon plasma phase

If the energy density is above ϵ_c multiple partonic scatterings will bring the deconfined matter to local equilibrium at the proper time [1] τ_0 and the Quark Gluon Plasma is formed. The plasma then evolves according to the laws of thermodynamics. As the plasma expands and cools it may enter a mixed phase with droplets of QGP and Hadron Gas.

Hadronization and Freeze out

When the temperature in the plasma is down to the critical temperature T_c the matter in the fireball will undergo the phase transition to the hadron gas phase. The produced hadrons then interact through inelastic scatterings until the hadron gas reaches the temperature of *chemical freeze-out* T_{ch}. At this point the relative abundances of the various particle species (the ratios) have been settled, as there will be no more re-scatterings in which the particles exchange quarks. The hadrons still undergo elastic scatterings, exchanging energy and momentum, until the temperature is down to *kinetic freeze-out* T_{kin}. From this point the yields and the shape of the spectra of the various particle types are fixed, as the hadrons are expected to fly out from the collision region without any more interactions taking place.

2.4.1 The Hadron Gas Phase

In the hadron gas phase the particles may undergo extensive elastic and inelastic re-scatterings; most of the observable signals related to the bulk particle production are therefore settled in this phase. The hot fireball undergoes an explosive expansion. Knowing the shape of the p_{T} spectra of the various particle types the kinetic freeze-out temperature T_{kin} and the collective transverse flow velocity β_s may be extracted. In [15] it is shown that by modelling the RHIC Au+Au reaction zone as many expanding thermal sources at different rapidities, with temperature T_{kin} and radial flow velocity β_s as rapidity dependent parameters the shape of the observed *transverse mass*, $m_{\mathrm{T}} = \sqrt{m^2 + p_{\mathrm{T}}^2}$, spectra are well reproduced.

Particle ratios and baryon content

From simple observations regarding the quark content of particles and anti-particles some general qualitative predictions regarding correlations between anti-particle/particle ratios and the net baryon density in a region of phase space may be made.

As mentioned in section 2.3.4 the net proton content in a region of phase space is a good measure of the net baryon content in that region. The $\bar{p}/p$

[1] *proper time* $\tau = \frac{t}{\gamma} = t\sqrt{1 - v^2/c^2} = \sqrt{t^2 - z^2/c^2}$.

ratio may therefore be used to get an estimate of the net baryon density in a given region of phase space. With relatively high degrees of transparency in the collision processes the net proton content of the fireball will vary with rapidity, as described in section 2.3.4. The $\bar{p}/p$ ratio is therefore expected to be quite high, but below one, at midrapidity; and falling as function of increasing y as the net baryon content increases closer to the fragmentation peaks.

Since the K^+ $(u\bar{s})$ contains one quark which is a constituent of both the proton and the neutron while the K^- $(\bar{u}s)$ does not, the relative production of these particles is also expected to have a dependency on the net baryon content of any region of phase space. While the total net strangeness content of the particles produced must be zero, any over-abundance of u-quarks compared with $\bar{u}$-quarks in a region of phase space is likely to lead to an increase in the number of K^+compared with K^-. The K^-/K^+ ratio may therefore be expected to be closely related to the $\bar{p}/p$ ratio.

The π^+ $(u\bar{d})$ and π^- $(\bar{u}d)$ are symmetrical in this respect. For Isospin symmetric collisions systems where the number of protons is equal to the number of neutrons, the $\pi^+$and π^-constituent quarks are equally abundant in the nucleons of the colliding nuclei. Using the simplistic arguments from this section it is therefore natural to expect this ratio to be close or equal to one in most regions of phase space.

The Generalized Thermal Approach

A statistical thermal approach has been very successful in describing particle yields assuming a phase space saturated with particles in local equilibrium. In this grand canonical model description the emitting source is characterized by its baryochemical potential μ_B, and its temperature T, identified with the chemical freeze out temperature T_{ch}. The strangeness chemical potential μ_S is fixed by net strangeness conservation and may be non-zero in a hadron gas, although the net content of strange quarks in the source is zero. Theoretical estimates of μ_S as function of μ_B using the grand canonical hadron gas model [16] are shown in figure 2.12. Here μ_S shows a temperature dependent correlation with μ_B. In this model the particle yields are governed by their *quark flavor fugacities* $\lambda_i = e^{\mu_i/T}$, where μ_i is the chemical potential of hadron species i, (see equation 2.4 for definition of μ_i).

The time scale for strangeness saturation of phase space is larger than the collision time scale [17] and we must allow for only partial strangeness saturation. Since the processes involved in distributing strangeness among the strange particle species have much higher cross sections than the strangeness producing processes we may assume relative chemical equilibrium among strange particle species [18], while they may be suppressed by a the phase space occupancy factor γ_s in relation to non-strange particles.

In an Isospin symmetric system, such as d+Au collisions, it is possible to

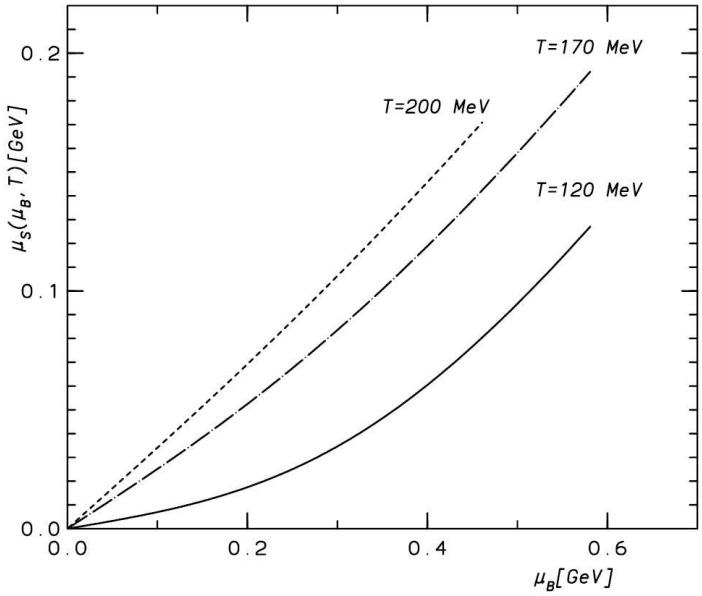

Figure 2.12: The temperature dependence of μ_S as function of μ_B from [16].

ignore the difference between u and d flavor and refer to the light quark chemical potential μ_q with $\mu_q = \frac{1}{3}\mu_B$ [18]. The chemical potential of hadron i may then be constructed as

$$\mu_i = (q_i - \bar{q_i})\mu_q + (s_i - \bar{s_i})\mu_s = B_i\mu_B - S_i\mu_S \tag{2.4}$$

where q_i, s_i $(\bar{q_i}, \bar{s_i})$ are the numbers of light and strange valence quarks (anti-quarks) in hadron i, and B_i, S_i are its Baryon and Strangeness numbers. The correlation between the two equivalent pairs of chemical potentials is given by:

$$\mu_B = 3\mu_q, \qquad \mu_S = \frac{1}{3}\mu_B - \mu_s = \mu_q - \mu_s \tag{2.5}$$

Since particles and anti-particles have identical masses the momentum phase-space factors will cancel out in ratios between yields as will saturation factors γ_i. The anti-particle to particle ratios are then given by the ratios between the particle fugacities and may be parametrized in terms of the quark or baryon chemical potential and the $\bar{p}/p$ ratio $\frac{\bar{p}}{p} \sim e^{\frac{-6\mu_q}{T}} = e^{\frac{-2\mu_B}{T}}$. Applying this to the K^-/K^+ ratio yields:

$$\frac{K^-}{K^+} = \frac{\gamma_s\lambda_s\lambda_q^{-1}}{\gamma_s\lambda_s^{-1}\lambda_q} = e^{\frac{2\mu_s}{T}} \cdot e^{\frac{-2\mu_q}{T}} = e^{-2\frac{\mu_S}{T}} = e^{-2\mu_B \cdot \frac{\mu_S}{\mu_B}} = \left(\frac{\bar{p}}{p}\right)^{\frac{\mu_S}{\mu_B}} \tag{2.6}$$

Hence the ratio $\frac{\mu_S(\mu_B,T)}{\mu_B}$ can be extracted from experimental antiparticle/particle

ratios. At small μ_B the ratio $\frac{\mu_S}{\mu_B}$ is expected to be approximately constant, as seen from figure 2.12.

Applying the same approach to π^-/π^+ ratios yields

$$\frac{\pi^-}{\pi^+} = \frac{e^0}{e^0} = 1 \tag{2.7}$$

which suggests a ratio which is independent of μ_B and equal to one. This is also what is suggested by the simple quark content observations made in the beginning of this section. Note that this prediction will only be valid in Isospin symmetric systems where $\mu_u = \mu_d$.

2.5 Bjorken's estimate of the Initial Energy Density

Making three assumptions Bjorken [19] produced a method for determining the energy density in the initial stages of the collision using the measured rapidity distribution of particles coming out of the collision region. The assumptions were that the collision processes are transparent, that the particle density dN/dy around mid-rapidity is constant (*boost invariance*) and, finally, that the source will follow a hydrodynamical evolution after it has been produced.

He focused on a thin slab of matter at mid-rapidity. Because of the boost-invariance, energy flow in the longitudinal direction will cancel out and can be disregarded. The total energy in the slab can be estimated from the mean energy $\langle E \rangle$ times the number of particles ($\langle E \rangle \approx m_T \cosh y$) in the slab-volume V. The volume of the slab is given by transversal area πR^2 of the short cylinder multiplied by its length Δz. Taking $c = 0$ the z-coordinate of a particle produced at z=0 at t=0 can be expressed by $z = t\beta = \tau\beta\gamma = \tau \sinh y$. The length of the slab element Δz at the proper time τ_0 when the plasma has formed is then given by $\Delta z = \tau_0 \cosh y \Delta y$. The mean energy density ϵ_0 at the proper time τ_0 may then be estimated as:

$$\epsilon_0 = \frac{\langle E \rangle}{V} = \frac{\langle m_T \rangle \cosh y \frac{dN}{dy} \Delta y}{\pi R^2 \tau_0 \cosh y \Delta y} = \frac{\langle m_T \rangle}{\pi R^2 \tau_0} \frac{dN}{dy} \tag{2.8}$$

The QGP formation time τ_0 is thought to be comparable to, or shorter than, the time it takes to produce particles, τ_{prod}, which is estimated to be in the range $0.4 - 1.2$ fm/c [3]. In central Au+Au collisions ($R \approx$6 fm) at $\sqrt{s_{NN}} = 200$ GeV the rapidity density of produced particles is (since most of the produced particles are pions) $\sim 3/2 \cdot$charged hadrons ~ 950 at mid-rapidity [20] and the mean transverse mass $\langle m_T \rangle \sim 0.6$ GeV. Using a conservative estimate of $\tau_0 = 1$ fm/c yields $\epsilon_0 \approx 5$ GeV/fm^3. This is 5 times higher than the critical energy density determined from QCD lattice calculations [21], indicating that the requirements for the production of matter in a deconfined phase are met.

2.6 Possible evidence of QGP formation at SPS and RHIC

2.6.1 J/Ψ suppression

In their article "J/Ψ suppression by quark-gluon plasma formation" [22] Matsui and Satz introduce the idea that one of the signatures left by matter in the QGP-state would be a suppression of the number of J/Ψ particles produced. The J/Ψ, which is a bound state consisting of a pair of c and $\bar{c}$ quarks, can be produced through the annihilation of a quark-anti-quark pair or, through gluon fusion or the decay of a single gluon. In a quark gluon plasma the color potential between two quarks will be screened by the free quarks and gluons present. This effect is called Debye-screening and in combination with the deconfinement it will lead to the dissociation of most J/Ψ-particles present in the plasma [3].

When the QGP plasma cools down and rehadronization occurs there will be plenty of lighter quarks and anti-quarks for the charm and anti-charm quarks to attach themselves to, thus making it less likely that a J/Ψ will be created. In [23] the NA50 collaboration at CERN published yields of J/Ψ in Pb+Pb collisions at $\sqrt{s_{NN}} = 158$ GeV. The most central collisions show a suppression of charmonium particles which, they state, "is stronger than what can be explained through the absorption by comoving hadrons", which is the predominant suppression factor in the case where there is no deconfinement. In [24] from 2005 they published additional results which confirm this picture.

2.6.2 Strangeness enhancement

The valence quarks in regular nuclear matter are u and d quarks. Any strangeness content of the particles detected after the collision must therefore have been produced in the collision process. In a quark-gluon plasma a $s\bar{s}$ pair may be formed through $q\bar{q}$ annihilation, gluon-fusion or the decay of a single gluon. The estimated critical temperature at which the phase transition from hadronic matter to a quark-gluon plasma is expected to occur ($T_C \approx 170 - 190$ MeV) is of the same order as the strange quark mass in the plasma ($m_s \approx 150 - 180$ MeV). This facilitates a high production rate of $s\bar{s}$ pairs.

In a hadron gas the processes involved in the production of strangeness have energy thresholds of several hundred MeV. Because of this the production of strange quarks will be higher and faster in a quark-gluon plasma than in a hadron gas. In order to produce multi-strange hyperons[2] in a hadron gas multiple hadronic collisions are necessary whereas the production of multi-strange particles in a QGP can happen through the simple coalescence between strange quarks at hadronization. The relative increase in the production of hyperons

[2] A hyperon is baryon containing one or more strange or anti-strange quarks.

in a QGP compared to that in a hadron gas is therefore expected to increase with the number of strange quarks it takes to produce the particle [25]. In [26] the WA97 and NA57[3] collaborations published their results on strangeness enhancement in Pb+Pb collisions compared to p+Be collisions as a function of the number of wounded nucleons N_{wound}. Their results show a clear enhancement of hyperons, and the enhancement grows with the strangeness of the produced hadron.

2.6.3 Elliptic flow v_2

Flow is the collective movements of the particles in the fireball due to the pressure gradients inside it. The particles on the surface will be accelerated outward by the pressure created by the density of matter in the fireball. As the surface particles move outwards, the pressure gradient move inwards, accelerating the more central particles outward as well.

When two particles with impact parameter $b > 0$ collide the created fireball will have an asymmetry in the transverse plane. The overlapping area has the form of an almond. This asymmetry make the pressure more effective in accelerating particles in the directions where the distance to the surface is shorter, since the inward-moving gradient has the shape of a collapsing almond. Because of this the flow will be greater in the transverse direction where the fireball is narrower. This effect reduces the spatial asymmetry, making the shape of the fireball more and more spherical. The spatial asymmetry of the fireball is thus converted into an asymmetry in the transverse momentum distribution of the particle in the fireball. By measuring the elliptical flow one can get an estimate of this asymmetry. Elliptic flow is mathematically defined by:

$$v_2 \equiv \langle \frac{p_x^2 - p_y^2}{p_{\mathrm{T}}^2} \rangle \tag{2.9}$$

This is in the case where the impact parameter b is aligned with the x-axis, making the initial fireball elongated in the y-direction.

Since the elliptic flow is relatively insensitive to the re-scatterings and expansion that happens in the hadronic phase [7] the measured elliptic flow can carry important information about the earlier stage of the collision. This is also thought to make the elliptic flow much larger in a collision where a quark gluon plasma is produced.

In figure 2.13 the measured v_2 of different particle species as a function of p_{T} is compared with predictions from hydrodynamical model using a parametrization of the quark gluon plasma as a perfect non-viscous fluid. The hadron-mass dependence of the predictions are very well reproduced in the data below p_{T}

[3]The WA97 and NA57 are consecutive collaborations using essentially identical experimental setups.

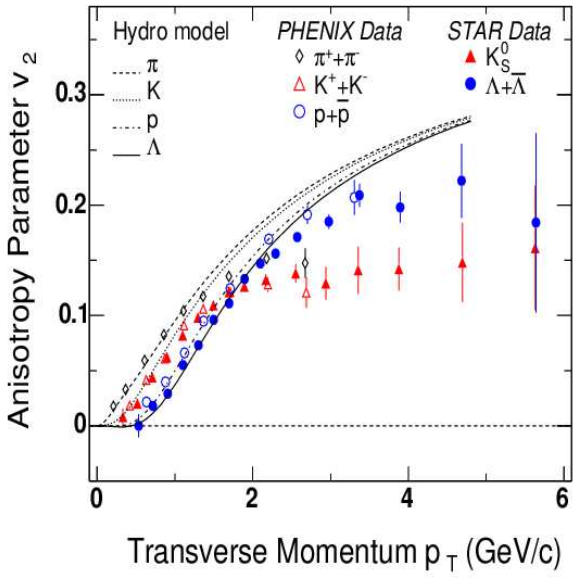

Figure 2.13: Elliptic flow as function of p_{T} measured by Phenix and Star compared with predictions from perfect fluid hydrodynamic predictions. Figure from [7].

~ 1 GeV/c. According to theorists [7] this perfect agreement between data and hydrodynamic model predictions can be seen as the "QGP fingerprint, showing there is a common bulk collective azimuthally asymmetric flow velocity field", whose magnitude can only be explained if the system behaves like a strongly interacting fluid such as the quark gluon plasma.

2.6.4 Jet quenching

In a QGP with free color charges, partons with high momenta will lose energy very rapidly due to gluon bremsstrahlung. This effect is often referred to as *Jet Quenching*, since jets of particles with very high momenta are produced in the hard inelastic scattering between partons in the initial stages of a collision. Such medium effects are not present in p+p collisions, where the jets escape without energy loss. The results from Au+Au collisions at RHIC show two effects which may be attributed to jet quenching:

High p_{T} suppression

The *Nuclear Modification factor* R_{AA} is a variable which is often used when comparing yields from collisions between massive nuclei with elementary pp

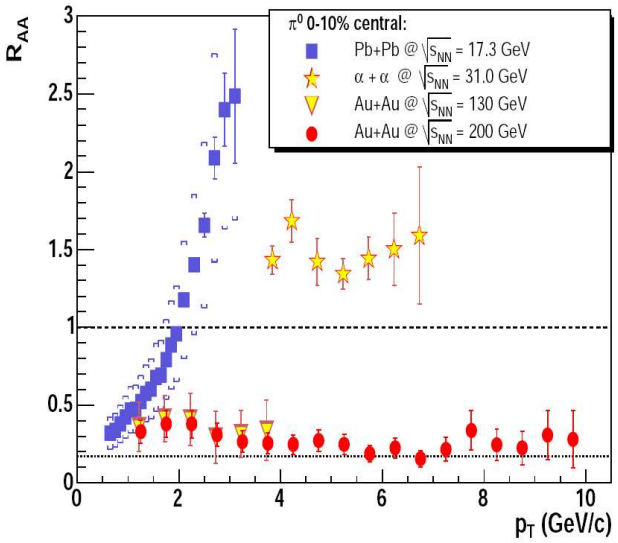

Figure 2.14: The nuclear modification factor R_{AA} in Au+Au collisions at different $\sqrt{s_{NN}}$. At lower beam energies the high-p_T tails are strongly enhanced, whereas the $\sqrt{s_{NN}} = 200$ GeV data show a clear suppression of the high p_T tails compared with p+p collisions. Figure from [7]

collisions, it is defined by:

$$R_{AA} = \frac{\frac{d^2N_{AA}}{dydp_T} \cdot \frac{1}{N_{coll}}}{\frac{d^2N_{pp}}{dydp_T}} \tag{2.10}$$

where N_{pp} and N_{AA} are the yields from p+p and Au+Au collisions, respectively. N_{coll} is the number of binary collisions in the Au+Au collision system. If there are no nuclear effects the yield from Au+Au collisions should scale like the yield from p+p collisions scaled with N_{coll}, in which case we should have $R_{AA} \sim 1$.

Results from massive nuclear collisions and p+Au collisions at low energies have shown a systematic enhancement of the high-p_T tail in these ratios, called Cronin-enhancement [27]. This is usually attributed to the broadening of parton p_T distributions due to the scattering of partons in the initial stage of the collision. Figure [28] shows the Phenix measurements of the R_{AA} for pions at midrapidity in Au+Au collisions at $\sqrt{s_{NN}} = 200$ GeV together with measurements from Au+Au at $\sqrt{s_{NN}} = 130$ GeV, $\alpha + \alpha$ at $\sqrt{s_{NN}} = 31$ GeV and Pb+Pb at $\sqrt{s_{NN}} = 17.3$ GeV. The lower energy results show strong Cronin enhancement at high p_T while the two gold measurements show a suppression by a factor of 4 to 5 in the entire p_T range measured.

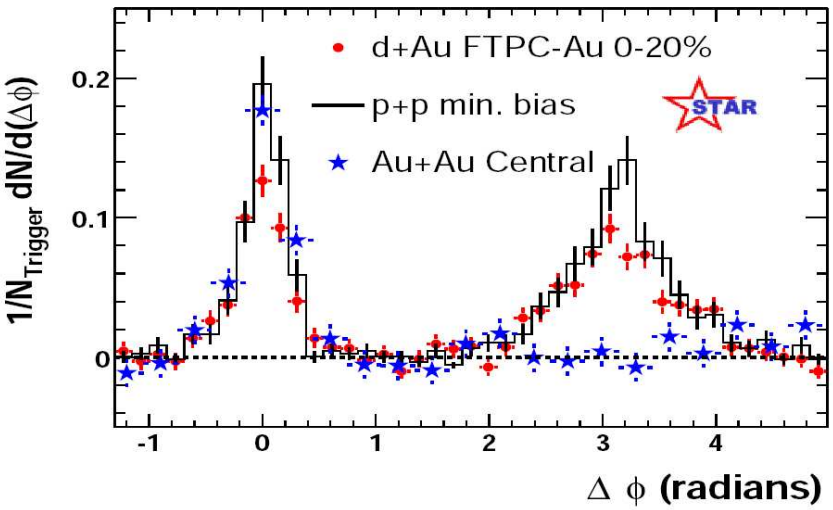

Figure 2.15: Back to back jet correlations measured by STAR. The p+p and d+Au data show a clear correlation, whereas the away side jet is missing in the Au+Au data. Figure from [7].

Missing Back to back correlations

Another interesting result from the Au+Au collisions is the missing back-to-back correlations of high p_{T} particles in central collisions. Particles with very high p_{T} are thought to be produced in hard parton-parton scatterings. These are usually accompanied by a shower of particles in more or less the same direction, as well as a corresponding shower in the opposite direction so that the vector sum of the transverse momenta of the two jets cancel each other out. In results from p+p collisions and nucleon nucleon collisions at low energies these correlations have been present, but in the central Au+Au collisions at $\sqrt{s_{NN}} = 200$ GeV the away-side jet appears to have been quenched. The back to back correlation measured by STAR for 3 different systems at $\sqrt{s_{NN}} = 200$ GeV are shown in figure 2.15. In d+Au collisions the jet correlations are similar to those in the p+p system.

2.6.5 The Initial State

Jet quenching in a deconfined medium is not the only possible explanation for the suppression phenomena demonstrated by the nuclear modification factors. The initial distribution of partons inside the colliding nuclei is expected to influence the way in which the collision unfolds.

An accelerated hadron consists not only of its valence quarks, but also of

gluons and $q\bar{q}$-pairs that have been produced from the gluons. Increasing numbers of partons means that the fraction of the total longitudinal momentum carried by each parton must necessarily decrease. At high energies the longitudinal momentum fraction of a hadron's total longitudinal momentum carried by one of its partons can be identified with the *Bjorken* x of the parton and it is expressed by:

$$x = \frac{p_{\mathrm{L},parton}}{p_{\mathrm{L},hadron}} \tag{2.11}$$

As the momentum of a hadron increases regions of lower x-partons become kinematically accessible. The gluon showers can instigate new gluon showers themselves. This causes cascades of gluon showers at low x to be created, the result of which is illustrated by the data from deep inelastic scatterings measured by HERA [29] shown in figure 2.16. As may be seen from this figure the Gluon Distribution function $xG(x, Q^2)$ show a rapid increase with decreasing x. There is also a strong rise in the gluon density with increasing momentum transfer Q^2 between the probe and the target, which, in accordance with the Heisenberg uncertainty principle, corresponds to looking at the target with increasing resolution and which depends on the relative momentum between probe and target.

The increase in the number of partons means that the transverse distance between each parton must necessarily decrease. In addition the low x partons will have long wavelengths, (also in accordance with the Heisenberg uncertainty principle), making heavy nuclei densely packed with low x partons at high energies (illustrated in figure 2.16). The valence quarks have momenta that are significantly higher than the low-x partons and their time-scales are therefore time-dilated relative to the slower partons. Since the low x gluons are set up by the color fields arising from the valence quarks, they evolve slowly compared with their natural time scales.

The cascades of low x gluons are thought to have a destructive interference reducing the likelihood of an interaction between the probe and a parton situated in the back of the nuclei with which it collides. This effect is often referred to as *Gluon Shadowing* or *Nuclear Shadowing*. It can also be viewed as a gluon recombination process and leads to a depletion in the number of gluons with $x \lesssim 0.1$, and enhancing the gluon density for $0.1 < x < 0.3$ relative to the gluon distribution in a proton.

Another effect, called *Parton saturation*, will occur when the gluon density is so high that phase space becomes saturated preventing the formation of more gluons due to instant recombination. This is expected to happen at very low $x \lesssim 0.001$. Phase space will then be saturated up to a certain momentum transfer Q^2 which grows with nuclear size as $\sim A^{1/3}$.

Both Nuclear Shadowing and Parton Saturation effects are able to qualitatively explain the suppression of hadron yields in Au+Au collisions, described in the above section.

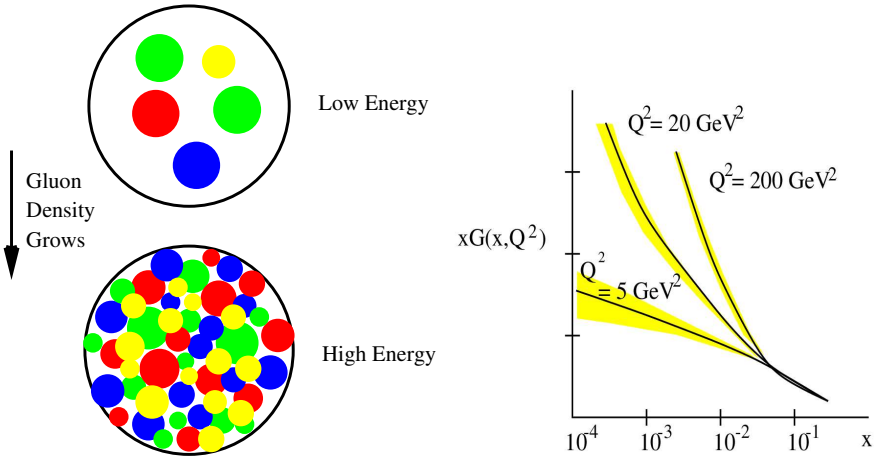

Figure 2.16: Left: Simplistic representation of the increase in the partons of a hadron with increased energy. Right: Schematic depiction of HERA measurements of the gluon distribution as a function of x for various values of Q^2. Figures from [7].

2.6.6 The d+Au control experiment

d+Au collisions were expected to settle the dispute on whether the jet-quenching phenomena were initial or final state effects. If the suppression phenomena seen at midrapidity in Au+Au collisions are caused by initial state effects related to the initial nuclear parton distributions they should be present in d+Au collisions as well, whereas a QGP-related final state effect would not be reproduced in this system where no hot deconfined medium is expected to be produced.

In the summer of 2004 the four RHIC experiments all published results from d+Au collisions. These showed back to back correlations and Cronin-like enhancement at mid-rapidity in d+Au collisions, giving a strong indication that the suppression of these phenomena in Au+Au collisions must be due to final-state medium effects. Figure 2.17 compares the measured centrality dependence of the R_{AA} with corresponding measurements of R_{dA}. In the most peripheral centrality bin the nuclear modification factors of the two systems are more or less in agreement, just below one. With increasing centrality the R_{AA} decreases whereas the R_{dA} shows a Cronin peak that grows with increasing centrality, illustrating the different behaviour of the two systems.

At the more forward rapidities on the deuteron side, however, BRAHMS results show that high-p_{T} suppression is present in d+Au collisions as well, with higher suppression for the most central events. The *pseudorapidity* $\eta(= -ln(tan(\theta/2)))$ dependence of these measurements are shown in figure 2.18. In addition to the R_{dA} another variant of the nuclear modificaction factor called the R_{cp} is shown. In the R_{cp} the yields from central collisions N_c are normalized

to the yields from peripheral d+Au collisions N_p instead of the yield from p+p collisions which is used in the R_{AA}, see equation 2.10. This yields:

$$R_{cp} = \frac{\frac{d^2N_c}{dydp_T} \cdot \langle N_{coll} \rangle_p}{\frac{d^2N_p}{dydp_T} \cdot \langle N_{coll} \rangle_c} \tag{2.12}$$

This is done to avoid systematic effects from the p+p reference spectra, which are taken under different run conditions. The underlying assumption is that peripheral d+Au collisions are equivalent with p+p collisions. This is not an entirely valid assumption, but the R_{cp} show the centrality dependence of yields in d+Au collisions. As may be seen from the figure the two sets of nuclear modification factors are qualitatively in good agreement, showing high-p_T enhancement at midrapidity, with suppression at forward η.

Hadrons with transverse mass m_T and rapidity y in the deuteron direction probe the Au parton-distributions at $x_{Au} \sim \frac{m_T}{\sqrt{s_{NN}}} e^{-y}$. Their transverse momenta p_T can be related to the momentum transfer Q^2 in a binary collision by $p_T^2 \lesssim Q^2$. The suppression of high-p_T particles at forward rapidities is therefore consistent with the effects expected from a depletion in the number of low x gluons in the gold nucleus, which, when colliding with medium-to-high-x partons in the deuteron, would give rise to hadrons at high longitudinal momentum on the deuteron side. Suppression at forward rapidities in d+Au collisions, probably due to the initial state of the gold nucleus, indicates that the suppression phenomena seen in Au+Au collisions at forward rapidities may also, in part, be due to initial state effects [7].

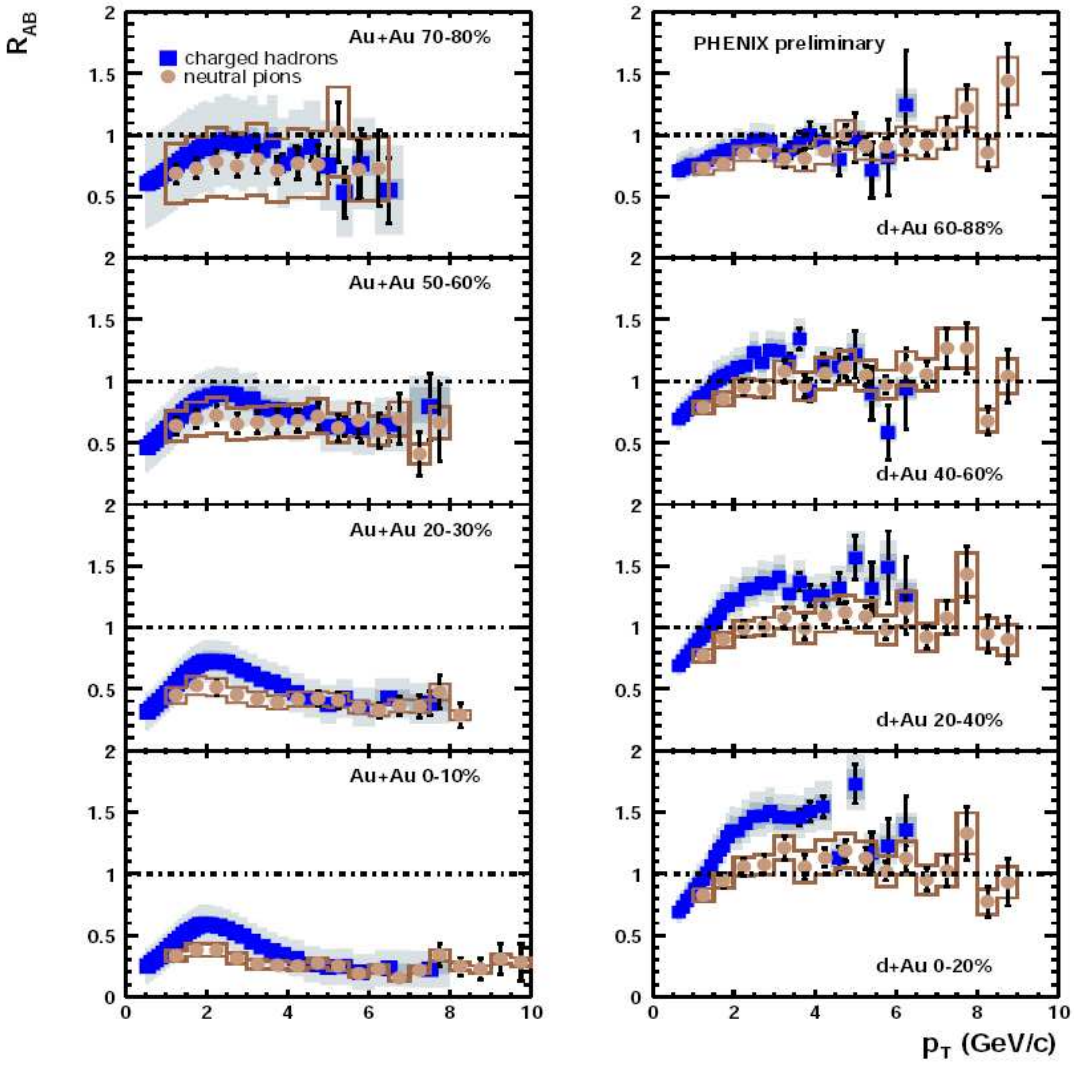

Figure 2.17: R_{AA} and R_{dA} for charged hadrons and neutral pions as function of p_{T} measured by PHENIX, published in [30].

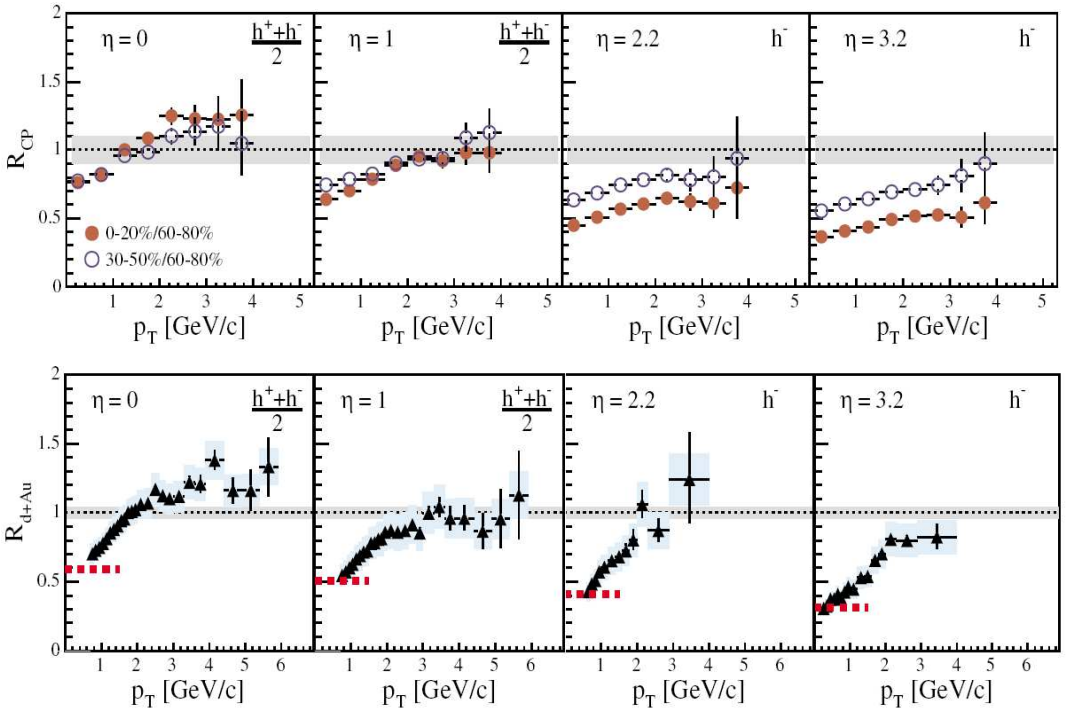

Figure 2.18: The Nuclear Modification factors R_{cp} (top) and R_{dA} (bottom) for charged hadrons as function of p_{T} and η in d+Au collisions at $\sqrt{s_{NN}} = 200$ GeV, measured by Brahms. Published in [28].

Chapter 3

Experimental setup

In this chapter I will give an overview of the BRAHMS detector, some of its technical features and capabilities. A more detailed description of the detector may be found in [31].

3.1 The Relativistic Heavy Ion Collider (RHIC)

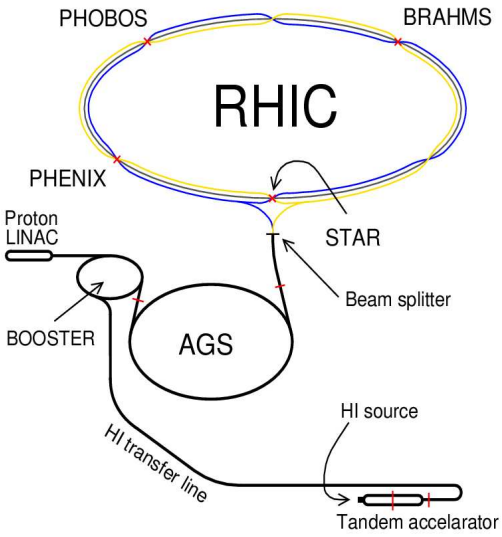

Figure 3.1: Schematic overview of the RHIC accelerator complex. Figure from [32]

The Relativistic Heavy Ion Collider (RHIC) [33] is situated at the Brookhaven National Laboratory (BNL) on Long Island, New York. It is part of the BNL accelerator complex and utilizes most of its facilities in order to reach the highest energies possible. A schematic overview of the entire accelerator complex is

shown in figure 3.1.

For gold and other heavy nuclei the acceleration process starts in the Tandem Van der Graaf which they typically leave after having been stripped of 12 electrons and accelerated to energies of 1 A MeV. Additional stripping followed by further acceleration in the Booster synchrotron new round of stripping prepare the ionized nuclei to enter the AGS ring with charges of +77e and energies of 95 A MeV. Here they are accelerated up to the maximum AGS energies of 10.8 A GeV. A final stripper removes the last two electrons and the fully ionized nuclei are ready to enter one of the two RHIC rings in which they are finally accelerated up to the energies of 100 A GeV. The two rings are actually hexagons with a common center, but slightly rotated with respect to each other, so that the beams cross between each of the corners. This gives 6 interaction points where the beams are essentially parallel, four of which have detectors installed. In addition to the BRAHMS detector the PHENIX [34], PHOBOS [35] and STAR [36] experiments are located at RHIC.

3.2 The BRAHMS experiment

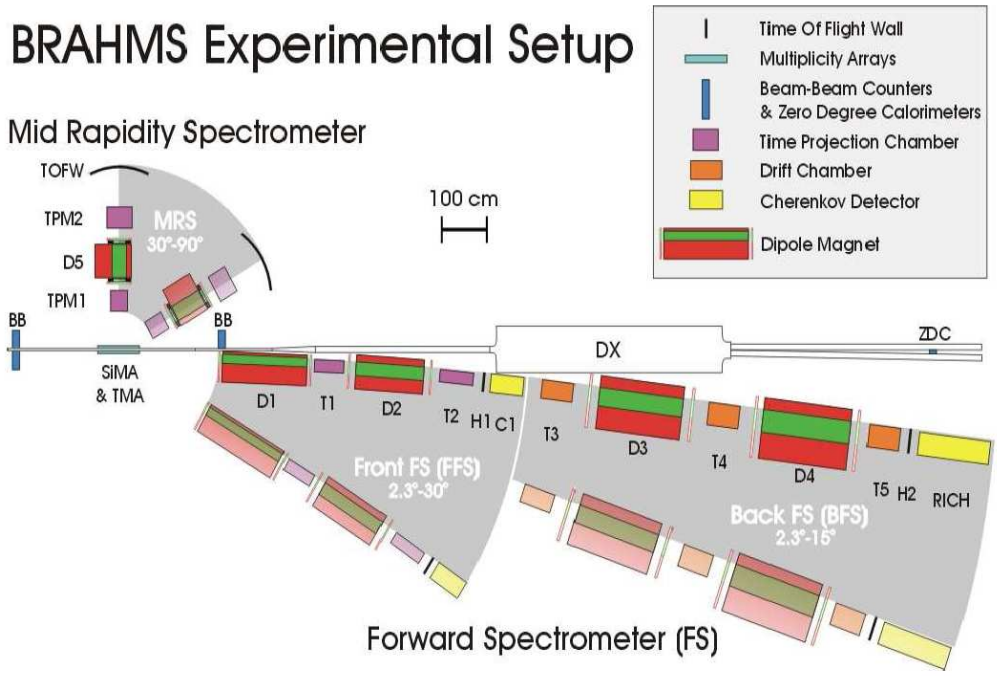

Figure 3.2: An overview of the BRAHMS detector. Figure from [14]

The BRAHMS detector, which is schematically shown in figure 3.2, consists of two separate detector-arms, the Mid Rapidity Spectrometer (MRS) arm and

the Forward Spectrometer (FS) arm. Both arms consist of tracking and time-of-flight detectors with magnets in between. In the FS arm there is also two Cherenkov detectors. In addition to the two spectrometer arms there is a set of global detectors dedicated to measuring event-characteristics, like the collision interaction point (the vertex) and the centrality of the collision.

3.2.1 Coordinate system

When describing the setup of the BRAHMS detector I will use the coordinate system shown in figure 3.3. The z-axis is aligned with the beam-direction, with origo at the *Nominal Interaction Point* which is the center of the region where the two beams cross. The x- and y- directions are the horizontal and vertical directions perpendicular to the z-axis, respectively, forming a right-handed coordinate system.

When referring to sub-detectors I will use a system where the z-axis is aligned with the center axis of the detector in the direction that the particles from the interaction point move. The x- and y- axes are the according perpendicular horizontal and vertical directions.

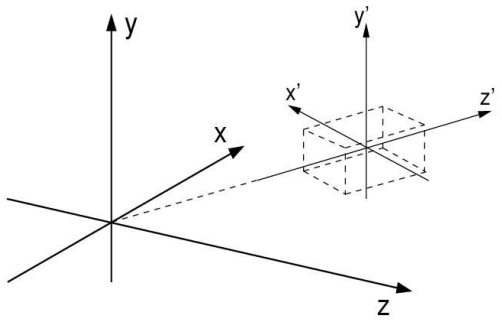

Figure 3.3: The coordinate system used in this thesis, with a sub-detector coordinate system.

3.2.2 The MRS arm

The Mid Rapidity Spectrometer consists of two tracking detectors, TPM1 and TPM2, on either side of a dipole magnet D5 and a Time-of-flight-wall (TOFW) at the very end. The center axis (internal z-axis) of the two tracking chambers and the magnet are aligned so that both negative and positive particles can make a track through the entire arm. The MRS covers what is called the mid-rapidity region at angles from $\theta = 30°$ to $\theta = 90°$ relative to the beam-direction.

3.2.3 The FS arm

The Forward Spectrometer arm is curved to conform to the path of a charged particle that traverses the magnetic fields of the consecutive magnets. Because of this the detector can only measure global tracks of one particle charge at a time. The preferred charge is switched by switching magnet polarities.

It is divided into two parts, the Front Forward Spectrometer (FFS) and the Back Forward Spectrometer (BFS). The FFS can cover angles from 2.3° to 30° in respect to the beam direction, whereas the BFS only covers the most forward region from $\theta = 2.3°$ to $\theta = 15°$ degrees.

The foremost component of the FFS arm is a dipole magnet (D1). This sweeps away low momentum particles and particles of the unwanted charge. The rest of the FFS arm is similar to the MRS system with two tracking chamber separated by a dipole magnet (D2) and a time of flight detector (H1). In addition the is a Cherenkov detector (C1) at its very end.

The BFS, which is an extension of the FFS arm, can only cover the very forward angles and is designed to identify particles with very high momenta. It consists of two dipole magnets (D3 and D4) sandwiched between three tracking chambers (T3, T4 and T5) ending in a time of flight wall (H2) and, finally, the Ring Imaging Cherenkov detector (RICH).

3.2.4 Global detectors and triggers

In addition to the two spectrometer arms the BRAHMS detector is outfitted with various global detectors. These are designed to detect the occurrence of events with the required characteristics, as well as determining the vertex position, the centrality, and the time when the event occurred. They also trigger the readout of events to the data acquisition system (DAQ).

Beam Beam counters (BB)

The beam beam counters consists of two arrays of Cherenkov detectors connected to photo-multiplier tubes, placed at $z = \pm 2.2$m on either side of the nominal interaction point. Their main purpose is to measure the vertex position using the left-right time difference, provide a start time for the time-of-flight walls and serve as triggers in Au+Au collisions. They cannot be used for these purposes in d+Au collisions, as the low multiplicities on the deuteron side requires higher sensitivities.

Multiplicity Array (MA)

The Multiplicity Array, which is placed around the beam pipe with its center at the nominal interaction point, measures the energy deposited by charged particles traversing it. It consists of two layers, the inner an array of silicon

strip detectors called the Silicon Multiplicity Array (SMA). On the outside we have the Tile Multiplicity Array (TMA) which is made up of plastic scintillator tiles. The amount of deposited energy can be related to the total number of produced charged particles and thus, to the centrality of the event.

Zero Degree Calorimeter (ZDC)

The Zero Degree Calorimeters are two lead-tungsten calorimeters placed at $z = \pm 18$m on either side of the nominal interaction point behind the beam-focusing DX magnets. All the RHIC interaction regions are outfitted with identical ZDCs, providing an opportunity to compare the beam luminosities at the interaction points. Since charged particles are swept away by the magnetic fields in the DX-magnets only spectator neutrons reach the ZDCs.

The energy signal may be used as an indication of the centrality of the event [37]. The difference between the time signals from the ZDCs can be used to determine the event vertex and they can function as triggers by requiring hits in both within some time limit. For collisions between two large nuclei they have been used as minimum bias triggers. For the d+Au collisions, with the deuteron containing only one neutron, a set of INEL-counters set up for the p+p run were used for this purpose.

In-Elasticity (INEL) counters

Three pairs of INEL counters were used as minimum bias triggers for the d+Au and p+p runs in 2003. They detect charged particles in the pseudorapidity range of $3.2<|\eta|<5.3$. The basic INEL counter consists of a plastic scintillator ring that is segmented into four pieces and arranged around the beam pipe. The three pairs utilized were located at $\pm 155cm, \pm 416cm$ and $\pm 660cm$. They can determine the Interaction vertex with a resolution of $\sim 5cm$ [14] using the relative time of flight measurements of particles hitting the left and right slat in coincidence. The INEL trigger is estimated to select $91 \pm 3\%$ of the d+Au inelastic cross section through GEANT simulations [14].

Spectrometer trigger slats

The number of tracks in p+p and d+Au collisions are low compared to Au+Au collisions. To facilitate the selection of events with tracks in the spectrometer arms trigger slats were placed in front of the two arms. For the MRS-trigger a 4 slat counter (TMrsT0) was installed across the front of TPM1. The FS-trigger was a 3 slat counter (TD1) placed in front of the D1 magnet. For the d+Au and p+p runs the time signals from the detector slats were used to provide the start time for time of flight measurements and for the Tracking Chambers.

Triggers

A trigger is a set of circumstances that indicates an event has happened and helps decide whether the Data Acquisition System should store the signals from the detector or ignore them. Since the storing of data takes both space and time, we have different triggers to indicate whether the information registered in the different detector arms are worthwhile storing or not. In table 3.1 is a list of the different triggers used in the d+Au 2003 runs: The events that I have used in this analysis are the trigger 3 and trigger 2 events for the MRS and the FS arm respectively with the minimum-bias trigger 5 as normalization to the number of events. But not only events with tracks in the detector arms are stored. Mainly for normalization purposes we need a statistically significant sample of minimum bias events. To minimize the statistical errors in normalized particle yields the different triggers are outfitted with a scaledown factor which may be adjusted to give the right composition of events. The value of this factor decides what fraction of a given event-type should be stored. If the scaledown value of trigger 5 is 10, then only one in ten registered trigger 5 events are actually sent to the DAQ and stored. This has to be taken into account when normalizations are done. (The normalization procedure is described in section 6.1.1.)

Trigger nr	Conditions
1	BBC time-coincidence with $N_L \geq 1$ and $N_R \geq 1$
2	BFS (INEL and TD1 and H1 and H2)
3	MRS (INEL and TMrsT0 and TOFW)
4	ZDC (peripheral)
5	INEL (minimum bias trigger)
6	FFS (INEL and TD1 and H1)
7	Pulser trigger for pedestal runs
8	1 Hz synchronization trigger

Table 3.1: List of triggers used for the d+Au runs with required conditions.

3.2.5 Tracking detectors

There are two types of tracking detectors. Time Projection Chambers (TPCs: TPM1, TPM2, T1 and T2) and Drift Chambers (DCs: T3, T4, T5).

Both types are chambers filled with a special mixture of gas that is ionized by passing charged particles. The electrons that are knocked loose create a shower of secondary electrons. The difference between the two types of tracking chambers lies in the way that the liberated charges are registered and reconstructed into particle tracks.

In the TPCs a homogeneous vertical electrical field makes the electrons drift up-wards. At the very top they are accelerated towards anode wires at +1200 volts creating showers of secondary electrons. The electrons are absorbed by the anode wires and the positive gas ions form a space charge which induces a mirror charge in the readout pads signaling the shower. Each chamber has several rows of these pads, with several pads per row. The x- and z-coordinate where the initial electron was knocked out may be decided by the position of the read-out pad(s) that were hit. For each triggered event a series of electronic snapshots of the readout pads are taken, giving the time dependence of the signal in each pad. The interval between each snapshot is 100ns and corresponds to a *timebin*. In combination with the drift velocity of electrons in the gas this enables the reconstruction of the y-coordinate of the initial ionization.

The drift velocity is sensitive to small changes in gas pressure. To make sure that we use the correct drift velocity there are Drift Velocity Monitors installed. These are not very efficient and calibrations with the help of horizontal silicon fibers placed outside some of the TPCs are therefore necessary. These calibrations, with others that are done for the TPCs, are discussed in chapter 4.

The DCs are gas detectors like the TPCs but these have a set of anode and field wires that attract the electrons and ions inside the gas volume, rather than a homogeneous field. Each DC has 3 modules with 8-10 wire-planes. Each plane has a set of parallel wires that are configured in one out of four orientations x, y, u or v. The x and y orientations are the x and y directions of the detectors internal coordinate systems (horizontal and vertical). The u and v orientation are lines in the x-y plane +/- 18 degrees off the y-axis.

3.2.6 PID detectors

The BRAHMS experiment have two different PID detector types: Time Of Flight detectors, and Cherenkov detectors.

Time of flight (TOF) detectors

There is a total of three time of flight detectors in the two spectrometer arms, the Time Of Flight Wall (TOFW) in the MRS-arm and H1 and H2 in the FS-arm. All three TOF detectors are built of plastic scintillator slats that are read out by two photo multiplier tubes, one at either end of the slat. The difference in the time signals from the two tubes is used to calculate the y-coordinate of the hit, while the average is used as the arrival time of the particle. The time resolution of the TOF detectors is 75 ps.

The Cherenkov detectors C1 and RICH

In the FS-arm there are two Cherenkov detectors. Cherenkov light is the light emitted when a charged particle traverses a medium with a velocity v greater than the velocity of light in the medium (given by c/n, where n is the refractive index of the medium). The Cherenkov-angle θ_{ch} at which the light is emitted is given by $cos\theta_{ch} = \frac{1}{\beta * n}$.

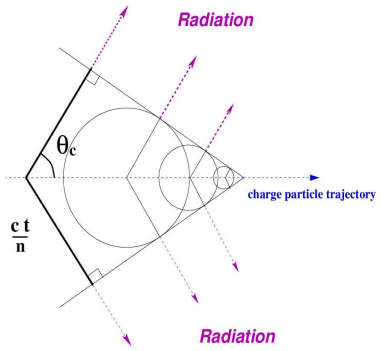

Figure 3.4: Light shock-waves created by a particle traversing a medium at $v > c/n$. Figure from [9].

The C1 detector consists of 32 tubes, and works as a threshold Cherenkov detector, i.e. it establishes whether the traversing particles has a velocity higher than c/n. It may be used to discriminate pions from kaons and protons when the momentum is above pion-, but below kaon- and proton-threshold.

At the very back of the FS the Ring Imaging Cherenkov (RICH) detector is situated. In the RICH a spherical mirror is used to reflect the Cherenkov light onto a finely segmented readout plane. All the Cherenkov light emitted from the trajectory of one particle will form a circle on the readout plane with a radius which depends on the Cherenkov angle and, hence, on the velocity of the particle.

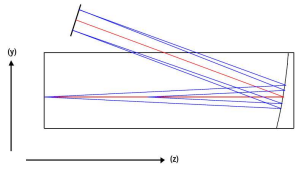

Figure 3.5: The light-focusing mechanism in the RICH detector. The Cherenkov light hits a spherical mirror and is reflected onto a finely segmented read-out plane.

Chapter 4

TPC Calibrations

Before the signals from the TPCs can be decoded into coordinates in space and time they need to undergo several calibrations. Firstly each read out pad is controlled to see if it behaves reasonably. Secondly the calculation of the y-coordinate of hits at the edges of the TPCs are checked for consistency with hits in the central part of the detector, to remove errors arising from the non-uniformities in the field toward the edges of the detector. Finally, the drift-velocity of the electrons through the gas is calibrated by using signals from horizontal fibers outside the gas volume, with known y-coordinates.

4.1 Pad Status

The module *calibratePadStatus.C* which takes care of the pad status calibrations loops through the signals received from all the pads in a TPC during a given run and establishes whether it was instrumented during the run in question and, if so, did it behave in a reasonable manner? Reasonable behaviour for a pad is defined as behaving like the other pads. Pads with deviant behaviour, i.e. that seem to be over-sensitive or insensitive are branded as hot or cold, respectively and disregarded. This is implemented by looping through all instrumented pads recording each pad's total accumulated ADC value over all hits (the sum) and the maximum ADC value from one hit during a run. These values are then divided by the average value for all instrumented pads for the given run.

To remove the influence of pads with extreme values a "mean average" is calculated, which is the average value of the scaled ADC values between zero and two, thus including pads whose values are reasonably close to the average only. All pads' values are then divided by this mean average and pads whose values are now lower than 0.2 are considered to be cold pads, whereas pads whose values are now higher than 3.0 are branded as hot.

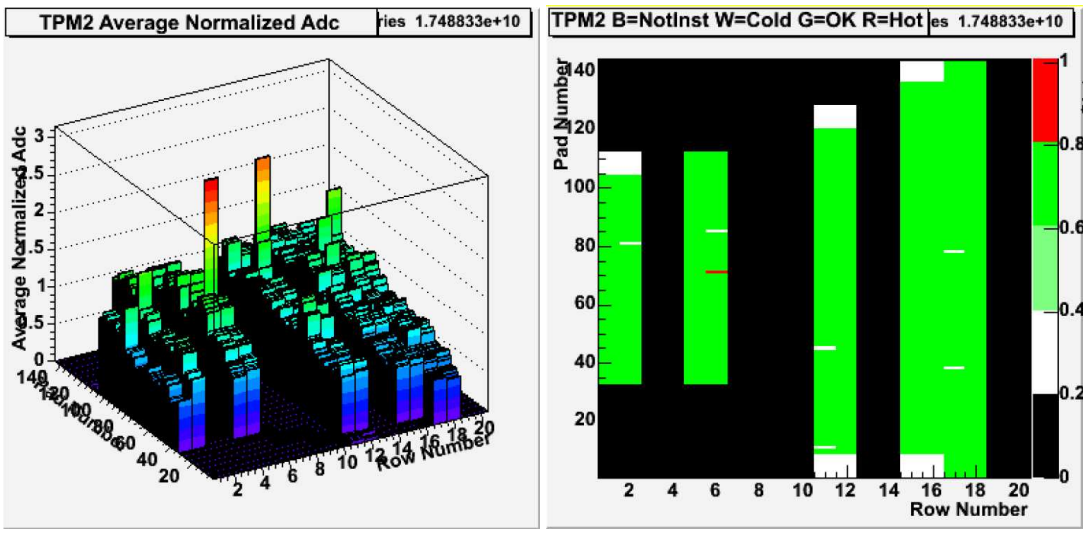

Figure 4.1: Sample histogram from the pad status calibrations of TPM2.

4.2 Time Offset

The Time Offset calibrations are designed to amend the row-time offsets experienced in the TPCs due to electronic imperfections, or non-uniformities in the field, and thus in the drift velocity of electrons through the gas, towards the edges of the detectors.

The algorithm behind the module *calibrateTime.C* which takes care of these calibrations is based on the assumption that these offsets are minimal in the most central part of the detector. Tracks are chosen that have a sufficient amount of hits in these select few central rows (5 hits minimum for T1 and T2, 3 hits for TPM2) to allow the track to be refitted on the basis of only these hits. Since the Drift Velocity calibrations have not been updated the y-positions of hits are computed using the drift velocity values from the latest calibration.

Subsequently the algorithm loops over all the hits that were included in the original track over again, comparing the calculated y-coordinate of each single hit with the y-coordinate of the refitted track at the same position. The deviation between the refitted track's y-coordinate and the single hit's y-coordinate is filled into a 2D-histogram as function of the y-coordinate of the hit. A sample histogram where the coordinates have been converted to time coordinates is shown in figure 4.2. Gaussian fits to all the entries in each separate bin are made, and finally a profile of the errors in the y-coordinate as function of y for the given row is made by fitting a 1st degree polynomial to the centroids of these gaussian fits as function of y. Finally, this function is converted into time coordinates (time error as function of timebin) and submitted into the calibration database.

4.3 Drift Velocity from fiber

The y-coordinate of tracks in the TPCs are calculated on the basis of the velocity of ions through the gas in the chambers. These velocities are sensitive to small variations in pressure and gas mixture. To allow recalibration of the drift velocities in the drift-chambers, two sets of horizontal drift-velocity fibers have been installed in each of the detector arms. There is one set of fibers on the front and back of TPM2, one set is placed in front of T1 and the last set is placed in the back of T2. The module *calibrateFibDrift.C* which takes care of these calibrations goes through all tracks and picks tracks that have hit a fiber. If the projection of the locally fitted track misses the fiber that was hit, this indicates that the drift velocity used to calculate the y-coordinate of the track is incorrect. The recalibration is done by comparing the calculated y-coordinate of the track at the fiber's z-coordinate with the physical y-coordinate of the fiber. This is done by storing all the calculated y-coordinates (track y-projection at fiber's z-coordinate) in a separate histogram for each fiber. When all tracks have been looped over, a gaussian is fitted to each of these fiber-histograms and the mean value is taken to be the "measured y-coordinate" of the fiber. In a new histogram we plot the measured coordinate of the fiber as a function of its actual y-coordinate (Both histograms shown in figure 4.3). By fitting a straight line to these points we get a function which reflects measured y-coordinates as function of actual y-coordinates. If the drift velocity used in calculating the tracks' y-coordinates is correct, the slope of this fit should be equal to one. A too high drift velocity will result in the calculation of too high drift distances and the slope of the fit will then be larger than one, and vice versa for too small values of the drift velocity. The correct drift velocity is calculated by dividing

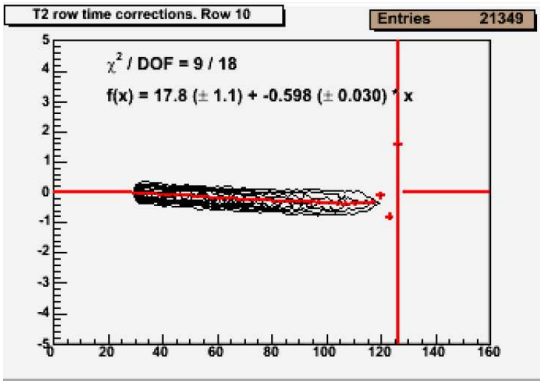

Figure 4.2: Sample of a histogram of deviations for row nr 10 in the T2 tracking chamber. Timebins along the x-axis. Deviation in fractions of timebin (100 ns) along the y-axis. The red points are the gaussian fits made to the distribution of time-deviations in each timebin.

the value used initially used by the slope of the fit.

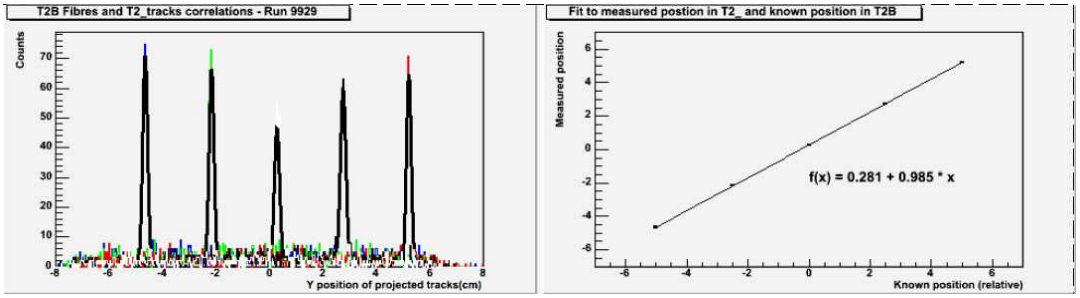

Figure 4.3: A sample histogram from drift velocity calibrations of T2 from run 9929. On the left are the gaussian fits to the y-position of the track-projections at the z-position of the fiber. On the right are the points given by plotting the measured y-coordinate as function of the actual y-coordinate of the slat that had been hit, with the 1st degree polynomial fitted.

Chapter 5

From raw data to PID

The raw data written to magnetic tapes during a run comprises all the information extracted from all the channels in each of the detectors. Once calibrations have been done the data can be decoded to obtain the physical quantities of interest. The most important tool used in this reconstruction are the ROOT C++ library package [38] together with a specifically designed BRAHMS reconstruction package built on top of the ROOT framework, called BRAT [39]. With the help of the standard BRAT modules the data are reconstructed and reduced into Data Summary Trees which contain all the relevant data from each event. When assigning PID I have used the Final Looping And PID (FLAP) software written by Bjorn Samset, to which I have made some very small modifications of the PID algorithm. The programs used in the final extraction of the various variables I have written myself.

5.1 Global Event Characterization

5.1.1 Event vertex determination

The event vertex, the z-coordinate where an event took place, is calculated using the time signals from the INEL-counters. The particles hitting the INEL slats have velocities equal to the beam velocities. The difference in the time coordinate of hits in a left and right slat is used to estimate the vertex position of the event by: $z = \frac{c}{2}(t_L - t_R)$, where $t_{L,R}$ are the time signals from the left and the right counter respectively. If the pair used is not symmetrically placed around Nominal Interaction Point the difference in distance is corrected for.

5.1.2 Centrality determination

The event centrality is determined through the charged particle multiplicity obtained from the Multiplicity Arrays. Details are given in [40].

5.2 Event selection

Event selections was done using the relevant spectrometer triggers (trigger 2 for Forward Spectrometer events and trigger 3 for MRS events). The normalization to the number of minimum bias events were done using trigger number 5, the INEL-trigger. For both arms I have chosen events with INEL-vertex in the region -40$<z<$40, but narrower cuts have been made in the MRS data in accordance with the vertex-dependence of the geometrical acceptance. No centrality cuts have been made.

5.3 Local Tracking

The signals in the various sub-detectors form points on a particle's trajectory through the detector. In the BRAHMS detector local tracking is defined as the reconstruction of these signals into three-dimensional space-coordinates in a sub-detector. Fitting a straight line to these points yields the particle's path through the sub-detector volume.

5.3.1 Local tracking in the TPCs

As described in section 3.2.5 the TPCs detect showers of electrons created when a charged particle ionizes the gas molecules in the gas chamber. The showers are created when the vertical electrical field makes the electron drift upward toward the readout pads situated on the ceiling of the chamber. When the DAQ receives a trigger from a spectrometer arm consecutive snapshots of the ADC values of each pad are stored. The period between each snapshot is called a *timebin*. The signals from a shower as function of timebin and pad number show up as a cluster of ADC values different from the background. Such a cluster is shown in figure 5.1. Given the vertical direction of the electrical field the x- and z-coordinates of the original ionized electron is given by the x- and z- coordinates of the cluster centroid. The time coordinate in combination with the drift velocity of an electron though the gas is used to calculate the y-coordinate of the point where the passing particle ionized the gas-molecules. The details of how this is done are discussed in [41] and in [42].

5.3.2 Local tracking in the DCs

Local tracking in the Drift Chambers is far more complicated. Hits in wires from consecutive planes with the various orientations give 2D information on the particle trajectory. As mentioned in section 3.2.5 the combination of track information from several wire-planes with different orientations can resolve the

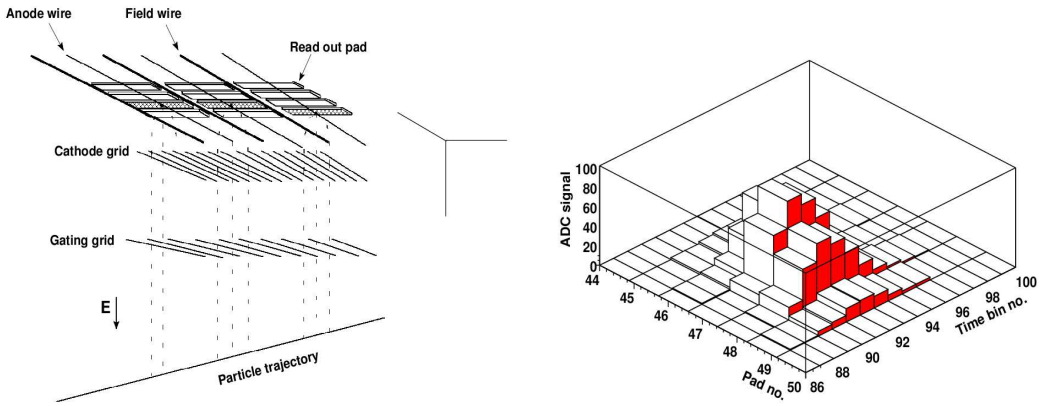

Figure 5.1: Left: Internal view of a TPC chamber. Right: The ADC-value cluster created by an electron shower.Figures from [9].

ambiguities with respect to combinations of (x, z) and (y, z) coordinates. Ambiguities as to which side (left or right) of a wire a particle passed are resolved by consecutive planes with identical orientation, but shifted slightly with respect to each other, making it possible to determine the particle trajectory in three dimensions.

5.4 Track matching and momentum determination

Track matching is the procedures done to determine whether various local tracks have been left by the same particle, i.e. matching local tracks left by one particle into one global track of the particle's trajectory through the entire spectrometer arm it has traversed. As mentioned in section 3.2 two tracking chambers are typically placed on either side of a magnet whose magnetic field is aligned with the y-axis. Both track-matching and momentum determination are based on the following relation governing the force $\vec{F}$ working on a particle with charge q traversing a magnetic field $\vec{B}$ at the velocity $\vec{v}$:

$$\vec{F} = q\vec{v} \times \vec{B} = q[v_z B_y, 0, v_x B_y] \tag{5.1}$$

Assuming a uniform magnetic field this makes the particle trajectory though the magnetic volume a helical curve with a constant slope α_y in the y-direction and a circular projection on the (x, z) plane. Since the force is perpendicular to the motion of the particle, and energy loss in air is small enough that it can safely be ignored, the particle's velocity is constant as it passes through the magnet volume. The curvature of the trajectory projection on the (x, z) plane will therefore be constant.

Matching parameters

Before the tracks can be matched a matching plane must be established. Firstly the points $F(x, y, z)$ and $B(x, y, z)$ are defined as the points in space where a projection of the front track enters the magnetic field and the point where a backward projection of the back track would have left the magnet field respectively. (Since the magnetic field does not go to zero immediately at the magnet edges these point are defined through an effective edge approach, where the z_{eff} where the magnetic field is said to end is defined by taking an integral over the magnetic field measured as function of z (and x for second order corrections) (see [9] for details)). A matching plane is then defined as the plane perpendicular to the line segment $[F, B]$ at the center of this. Using the notation from figure 5.2 the angles Ψ_f and Ψ_b are defined as the angles in the (x, z) plane between the line segment $[F, B]$ and the front and back tracks respectively. As observed from equation 5.1 the curvature of the trajectory through the magnet volume should be constant, which yields the first matching criterion:$\Delta\Psi = \Psi_f - \Psi_b = 0$. The last two matching criteria follow from the fact that the magnetic force $q\vec{v} \times \vec{B}$ has no component in the y-direction: The slopes $\alpha_{y,f}$ and $\alpha_{y,b}$ in the y-direction of the front and back tracks must be identical, yielding: $\Delta\alpha_y = \alpha_{y,f} - \alpha_{y,b} = 0$. Secondly, the y-coordinate of the intersection points P_f and P_b of the front and back tracks with the matching plane must be the same yielding $\Delta y = P_{y,f} - P_{y,b} = 0$. In summary:

$$\Delta\Psi = 0 \tag{5.2}$$

$$\Delta\alpha_y = 0 \tag{5.3}$$

$$\Delta y = 0 \tag{5.4}$$

In reality measured differences $\Delta\Psi$, $\Delta\alpha_y$ and Δy have Gaussian distributions around zero and the matching conditions are elliptical cuts made from Gaussian fits to these distributions. This sometimes leads to situations where there is more than one front track that meets the matching criteria for a particular back track (or vice versa, but this is rare since the front tracks generally are much more numerous). In this case the track with the best match is selected to be the real track, where the quality of the match is given by the quadratic sum over the fraction between each matching parameter and the width of their Gaussian distributions, i.e $Match^2 = \left(\frac{\Delta\Psi}{\sigma_\Psi}\right)^2 + \left(\frac{\Delta y}{\sigma_y}\right)^2 + \left(\frac{\Delta\alpha_y}{\sigma_{\alpha_y}}\right)^2$

Momentum determination

Once tracks from either side of a magnet have been matched, the momentum of the detected particle through the magnet volume may be calculated. The projection of the momentum on the (x, z) plane, p_{xz}, is given by :

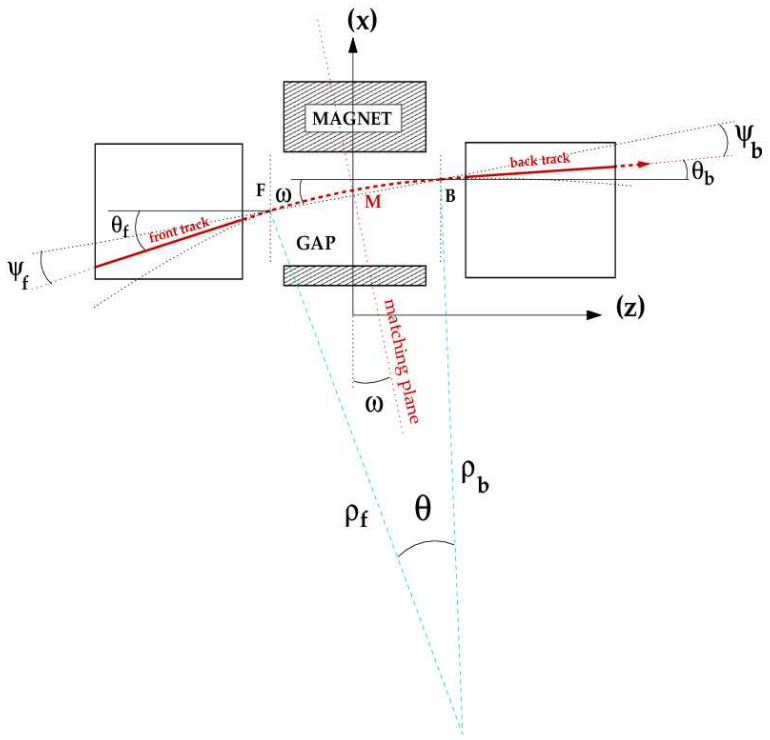

Figure 5.2: Top view of trajectory of a charged particle through a magnet gap. Figure from [9].

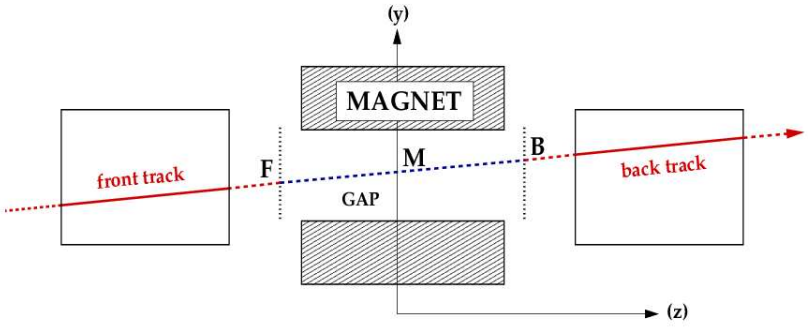

Figure 5.3: Side view of a particle trajectory through a magnet gap.Figure from [9].

$$p_{xz} = \frac{qB\Delta L}{(sin\theta_b - sin\theta_f)} \tag{5.5}$$

where θ_b and θ_f are defined in figure 5.2 and ΔL is the length of the magnetic field in the local z-direction (estimated through the effective edge approach).

The relations $p_y = \alpha_y p$ and $p^2 = p_{xz}^2 + p_y^2$ in combination with equation 5.5 finally yields the momentum as:

$$p = \frac{p_{xz}}{\sqrt{1 - \alpha_y^2}} \tag{5.6}$$

For the full FS track the momenta are obtained from 3 matchings, through D2, D3 and D4. Track refits are finally done using all available information to yield best possible FS trajectory and combined momentum.

5.5 Track Selection

The selection of tracks is designed to remove secondary tracks, which do not originate from the interaction point. The most basic track requirement is a full track, i.e. the particles trajectory may be reconstructed with local tracks in all the tracking detectors it has traversed as well as fulfilling the matching criteria through the various magnets. In addition, *fiducial* and *pointing cuts* were made to ensure good track quality in magnets and track origin close to the primary vertex.

Fiducial cuts

Fiducial cuts are done because of uncertainties in track directions near the spectrometer edges, i.e close to tracking chamber or magnet walls. Tracks in these regions may arise from secondary particles from interactions with the detector wall or primary particles that have been deflected. They may also have traversed inhomogeneities in the magnetic or electric fields close to the edges. Cuts in the tracking chambers and magnet volumes are imposed to remove any such effects.

The magnet fiducial cuts remove particles whose track at any point is closer than 0.5 cm to the magnet edges.

To avoid edge effects from the tracking chambers cuts are set in the track position in the back plane of TPM2 in the MRS and T2 in the FS. These positions are used because they are the narrowest parts of the acceptance for the MRS and FS arms, respectively. The cuts used are

TPM2: -15cm$<x<$20cm, -7cm$<y<$3cm

T2: -12cm$<x<$17cm, -8cm$<y<$6cm

These cuts correspond are approximately equivalent with removing tracks 1 cm away from the experimental edges of the detectors, i.e. the region where tracks are reconstructed.

Pointing cut

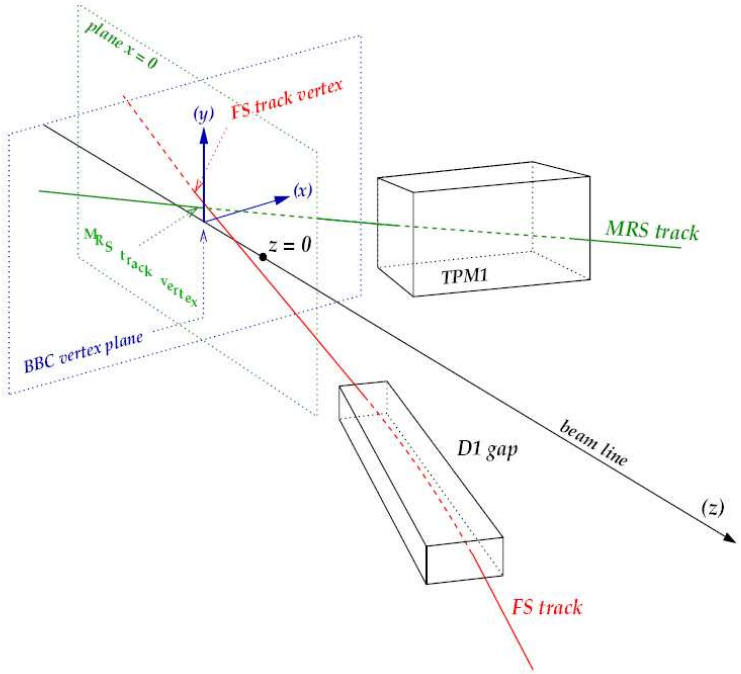

Figure 5.4: The definitions of track-vertexes in the two arms. In the MRS arm the primary intersection plane is the beam plane $x = 0$ The variable V_z is defined as the distance from the INEL-vertex (BBC vertex in figure) and the track's z-coordinate in the intersection plane. V_y is simply the track's y-coordinate in the intersection plane. For tracks from the FS the plane defined by z =INEL-vertex is used as primary intersection plane. V_x and V_y are track's x and y coordinates in this plane accordingly. Figure from [9].

The pointing cut is designed to remove tracks that do not point back to the primary interaction region. This is done by defining an intersection plane to which the particle tracks are projected. In the MRS arm the intersection plane is defined as the xz plane at $x = 0$, often referred to as the *beam plane*. In this plane we use a coordinate system where origo is placed in the point ($y = 0, z$ =INEL-vertex). The variables used to make the cut are the y- and z-coordinates V_y and V_z of the point where the track intersects the beam plane. By making Gaussian fits to the track vertex distributions and extracting the

centroids and widths of these fits the accepted region is defined as the elliptical region in the intersection plane within some set number of sigma N_σ centered around the point $(y_{centroid}, z_{centroid})$ defined by the centroids of the two Gaussian distributions. In mathematical terms:

$$(\frac{z - z_{centroid}}{\sigma_z})^2 + (\frac{y - y_{centroid}}{\sigma_y})^2 < N_\sigma^2 \tag{5.7}$$

In the FS arm the extrapolation of the track to the event vertex requires swimming the track back through the D1 magnet using the fitted momentum. The pointing cut is done in the plane perpendicular to the beam line defined by the z =INEL-vertex. The variables used are V_y and V_x defined in the same manner as V_y in the MRS arm only in the FS intersection plane.

$$(\frac{x - x_{mean}}{\sigma_x})^2 + (\frac{y - y_{mean}}{\sigma_y})^2 < N_\sigma^2 \tag{5.8}$$

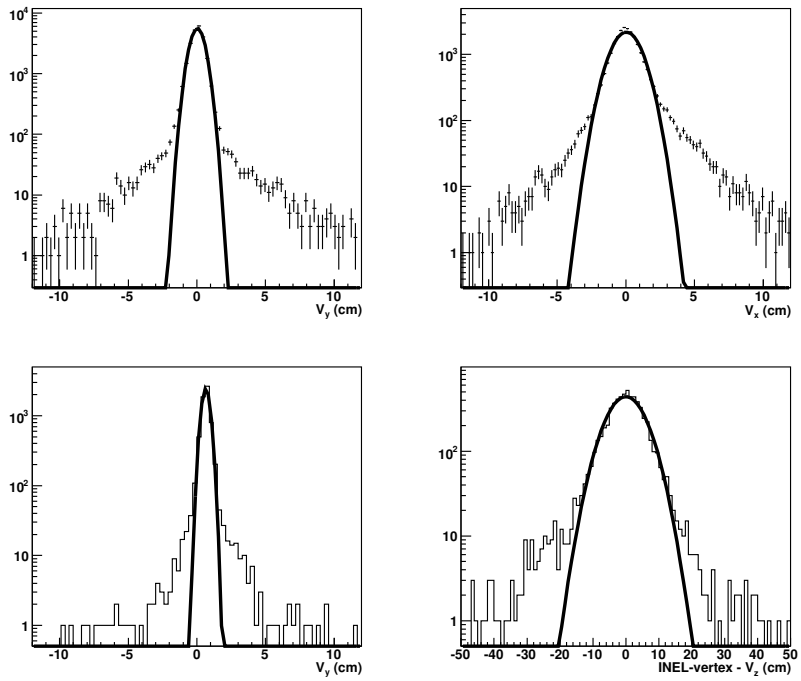

Figure 5.5: Top: The V_x and V_y for all charged particles from run nr 8514 (8 degree 843 magnet current, negative polarity). Bottom: V_y and (INEL-vertex - V_z) distributions for all charged particles from run 8368 from the 90 degree setting. The curves are gaussian fits to the distributions.

For both arms the region is redefined by new fits from every run, thus taking into account how the primary intersection region may move significantly depending on the tuning of the beams.

In this analysis I have used cut widths of 2.5σ.

5.6 Particle Identification, PID

The relationship between a particle's momentum p, velocity v and mass m is given by:

$$p = \gamma m v = \frac{mv}{\sqrt{1-\beta^2}} = \frac{m\beta c}{\sqrt{1-\beta^2}} \tag{5.9}$$

where $\beta = \frac{v}{c}$. Using $c = 1$ this may be reordered into:

$$\frac{1}{\beta} = \sqrt{\frac{m^2}{p^2} + 1} \tag{5.10}$$

This relation is the basis of most of the identification of particle species in the BRAHMS detector.

5.6.1 Time Of Flight PID

Time of flight PID is based on very precise time measurements from the Time-Of-Flight Walls placed in the detector arms. The time of flight t is defined as the time it takes a particle to traverse the distance from the trigger slat to the TOF-slat where it is detected. The start time is given by the relevant spectrometer trigger. Using the flight length L, which is the length of the track from its intersection with the trigger slat to the TOF slat where it is detected, one may find a particles velocity v by $v = L/t$. By inserting the mass of a particle species into equation 5.10 a curve in $(p, 1/\beta)$ space is defined, on which any particle of the given species should lie. Taking into account the uncertainties in time of flight, $dtof$ (given in units $\frac{dt}{L/c}$), and our momentum measurements, dp, equation 5.10 turns into:

$$\frac{1}{\beta} = \sqrt{\frac{m^2}{(p \pm dp)^2} + 1} \mp dtof \tag{5.11}$$

The two curves defined by adding and subtracting the uncertainty variables creates the limits of our PID region. An example of TOFW PID is shown in figure 5.6. The used uncertainty values are the default values from FLAP $dp = 0.1$Gev/c and $dtof = 0.0025$, which is a dimensionless parameter like β. The values have been selected to give a good fit to the experimental $(p, 1/\beta)$ band, using visual inspection.

In reality dp is momentum dependent [11]. It is acceptable to use the simple expression with constant dp for computation of ratios, since the momentum dependence will be identical for positive and negative particles and any error will cancel out as described in section 6.1.6.

5.6.2 RICH PID

The relation between a particle's velocity through a medium and the angle of the Cherenkov light emitted is given by::

$$cos\theta_{ch} = \frac{1}{\beta * n} \tag{5.12}$$

The radius of a ring on the read-out plane is given by:

$$r = F \tan \theta_{ch} \tag{5.13}$$

where F is the focal length of the mirror used to focus the Cherenkov light onto the plane. Combination of equations 5.10, 5.12 and 5.13 yields

$$r = F \tan \left(\cos^{-1} \left(\frac{1}{n} * \sqrt{1 + \frac{m^2}{(p \pm dp)^2}} \right) \right) \pm dr \tag{5.14}$$

The variables dr and dp are the uncertainties in our measurements of the particle's ring-radius and momentum respectively. The values used were $dR =$ 0.35cm , $dp_\pi = 0.6$GeV/c, $dp_K = 0.5$GeV/c and $dp_p = 0.2$GeV/c. As in the MRS the PID is done by selecting particles that lie between the two lines defined by the adding and subtracting of the uncertainty variables. (see figure 5.7). For particles that are above both pion and kaon threshold the RICH-detector may also be used to identify protons as any particle between kaon and proton threshold that doesn't emit Cherenkov light. In the 8 degree setting I have used this method of proton identification, while I have restricted the proton identification to particles between the proton PID curves in the 4 degree setting. This is to avoid contamination from pions and kaons whose rings have not been detected in the RICH. In the 8 degree setting there are no particles above proton threshold. My estimation of the contamination to the protons in this setting due to the RICH inefficiency are described in section 6.1.4.

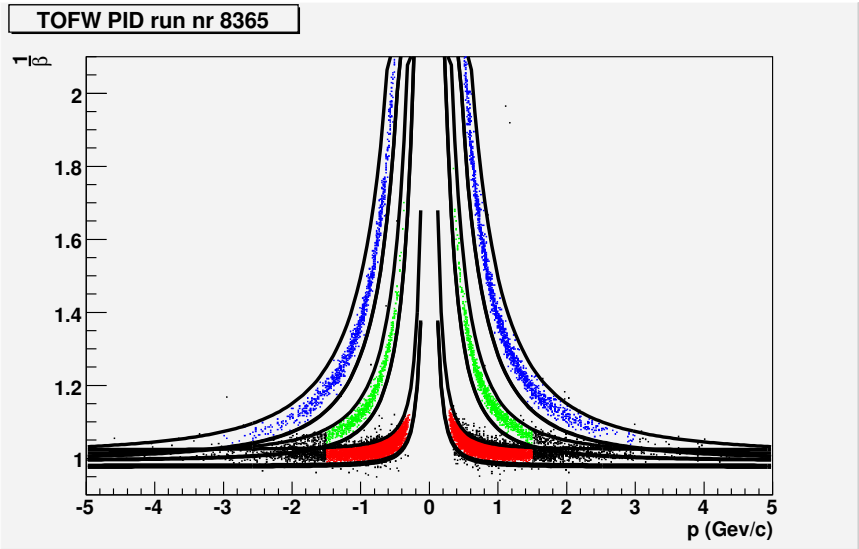

Figure 5.6: Sample of TOFW PID-histogram from the 90° 1050 setting. Curves are the PID-curves given by subtracting and adding the uncertainty variables in equation 5.14. The red points are particles identified as pions. Green points are kaons and blue points are protons. Black points are particles that haven't been assigned a PID as they lie outside any PID area or within two making the PID ambiguous.

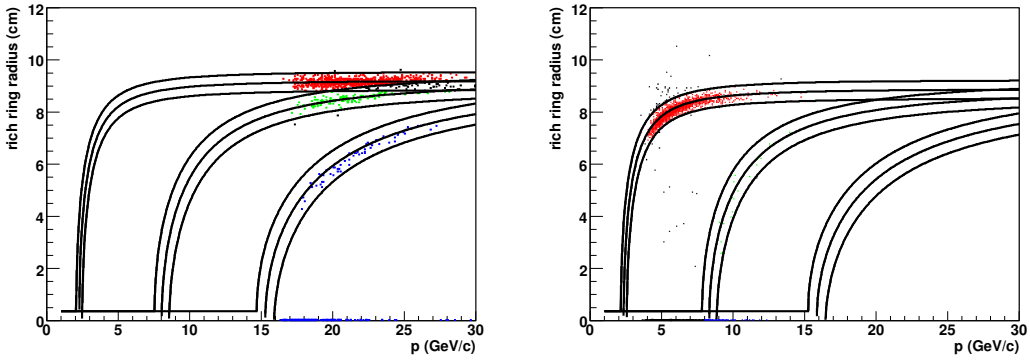

Figure 5.7: Sample of RICH-PID histogram from the 4 and 8 degree settings. Curves are the PID-curves given by subtracting and adding the uncertainty variables in equation 5.14. The red points are particles identified as pions. Green points are kaons and blue points are protons. Black points are particles that haven't been assigned a PID as they lie outside the PID areas, or in a region where two PID region overlap, making the PID ambiguous.

Chapter 6

Extraction of ratios

For each particle type there are only four small regions of (y, p_{T})-space where there is data from both particle charges available. In order to obtain the ratios at a given point of phase space I need to estimate the true yields $\frac{d^2N}{dydp_{\mathrm{T}}}$ of each particle species and charge at that point. The ratio $R(y, p_{\mathrm{T}})$ is defined by

$$R(y, p_{\mathrm{T}}) = \frac{\frac{d^2N^-}{dydp_{\mathrm{T}}}}{\frac{d^2N^+}{dydp_{\mathrm{T}}}} \tag{6.1}$$

where N is the true particle density per event as function of y and p_{T} . Before the particle density can be extracted the data need to be normalized to the number of minimum bias events and corrected for effects which may have an impact on the reconstructed yields.

6.1 Normalization and Corrections

For normalization and correction purposes the spectrometer track data for each particle species are initially stored in separate (y, p_{T}) histograms, depending on the location of the event vertex. In the MRS arm this is taken to be the coordinate of the track intersection with the beam plane. In the FS the z-coordinate of the INEL-vertex is used. The true particle density in the vertex bin i is given by:

$$\frac{d^2N^{\pm}}{dydp_{\mathrm{T}}}|_i = \frac{d^2n^{\pm}}{dydp_{\mathrm{T}}}|_i \cdot \mathrm{CORR}^{\pm}(y, p_{\mathrm{T}})|_i \tag{6.2}$$

where $dn/dydp_{\mathrm{T}}$ is the raw yield of particles as function of rapidity and transverse momentum and

$$\mathrm{CORR}(y, p_{\mathrm{T}})|_i = \frac{Norm|_i}{Corr(y, p_{\mathrm{T}}) \cdot Acc(y, p_{\mathrm{T}})|_i} \tag{6.3}$$

$\mathrm{Corr}(y, p_\mathrm{T})$ is the Correction factor which contains various physics and detector efficiency corrections, $\mathrm{Norm}|_i$ is the normalization to the number of minimum bias events in the given vertex bin and $\mathrm{Acc}(y, p_\mathrm{T})|_i$ covers corrections for the geometrical acceptance. All of these are discussed in sections 6.1.1, 6.1.2, 6.1.3 and 6.1.6.

From equations 6.1 and 6.2 it is clear that any correction factor which is independent of the particle charge will cancel out when the ratios are calculated, making the estimation and application of these correction factors unnecessary. This is based on the assumption that all the acceptance and the various physics corrections can be factorized independently. This might not be strictly correct, but I assume that possible correlation effects will cancel out in the ratios, at least for simple loss factors. With this assumption almost all the corrections cancel out for the data from the FS arm where there is data from both polarities. Only the correction for absorptions in the spectrometer material, which has a larger effect for $\bar{p}$ than for p and the RICH inefficiency correction which must be included in the 8 degree data to subtract contaminations when the RICH is used in veto mode are necessary. (See sections 6.1.2-6.1.6).

From the MRS arm there is only data from one polarity available so the geometrical acceptances of negative particles differ from the ones for the positive particles. I therefore had to include acceptance corrections as well as the absorption corrections which differ for the protons and anti protons in the MRS arm also.

6.1.1 Event normalization

As mentioned in section 3.2.4 the data are taken in short time periods called runs where the various triggers are given a scaledown value that is fixed for the duration of the run. For a given vertex bin i and run the normalization factor $Norm(i, run)$ is given by

$$Norm(i, run) = \frac{Scd(run)}{Events(i, run) Inelscd(run)} \tag{6.4}$$

Where $Scd(run)$ is the scaledown value of the relevant spectrometer trigger as listed in table 3.1, $Events(i, run)$ is the number of INEL-triggers in the given vertex-bin and $Inelscd(run)$ is the scaledown of the INEL-trigger for the given run.

6.1.2 Acceptance corrections

The geometrical acceptance of each spectrometer arm depends on angular setting, magnetic field and the event vertex position from where particles originate. (y, p_T) maps of the geometrical acceptances of the various particle species were

generated by making a *Geant*[1] simulation of particles traversing the detector. Each particle's energy loss due to interactions with the material in various parts of the detector that it traverses are simulated according to the well known Bethe-Bloch formula. To get a full coverage of the actual geometrical acceptance of the detector particles are thrown over the momentum and angular ranges slightly larger than the ones where the actual geometric acceptance allows a track to pass trough the spectrometer.

For a particle to be defined as accepted it has to pass through the spectrometer arm with a sufficient number of hits in the PID and Tracking detectors and fulfill the fiducial cuts (see section 5.5) that are required for the actual tracks. The acceptance is simply defined as:

$$Acc(y, p_{\mathrm{T}})|_i = \frac{\text{accepted particles}(y, p_{\mathrm{T}})|_i}{\text{thrown particles}(y, p_{\mathrm{T}})|_i} \cdot \frac{\Delta\Phi}{2\pi} \tag{6.5}$$

where $\Delta\Phi$ is the azimuthal range over which particles have been thrown in the simulation. The scale $1/2\pi$ normalizes the acceptance to full azimuthal coverage.

In the settings where there is data from both polarities (which is the case in the Forward Spectrometer arm) the acceptance map $Acc^{-}(y, p_{\mathrm{T}})|_i$ of negative particles of a given species in vertex bin i is identical to the acceptance maps of the positive particles in the positive data set in the same setting and vertex bin.

The acceptances of the various particle charges approach zero at the edges of the acceptance maps. Before the data were extracted the acceptance edges were removed by throwing away all bins where the acceptances were below some limit at about 30 per cent of the plateau found in the center of the maps.

6.1.3 Absorption corrections

The particles have to pass through the beam pipe wall and the trigger-slats before they enter either one of the spectrometer arms. As they traverse the arm they interact with air and other gases and material along the length of the spectrometer arm. This causes particle dependent losses in our spectra, as some particles are scattered or absorbed in the material. The absorption corrections as function of momentum p have been estimated through simulations particles traversing the spectrometer arm. One set of corrections amend the errors arising from interactions with the beam pipe and the material in the spectrometer arms. A second set of corrections take the effects of the spectrometer trigger slats into account. In both simulations the correction function is defined by:

$$Abs^{\pm} = \frac{(\text{surviving particles})^{\pm}}{(\text{thrown particles})^{\pm}} \tag{6.6}$$

[1] *Geant* is part of the *CERNLIB* package freely available from CERN [43]. It simulates the interaction of elementary and composite particles with matter.

The total absorption correction has been taken as the product of the two survival probabilities. For pions and kaons both of these effects are identical for the two particle charges and the factor will again cancel out when the ratios are computed. For the protons, however, the effect for the anti-proton is slightly different than for the protons. For these I used the functions plotted in figure 6.1 obtained from [11].

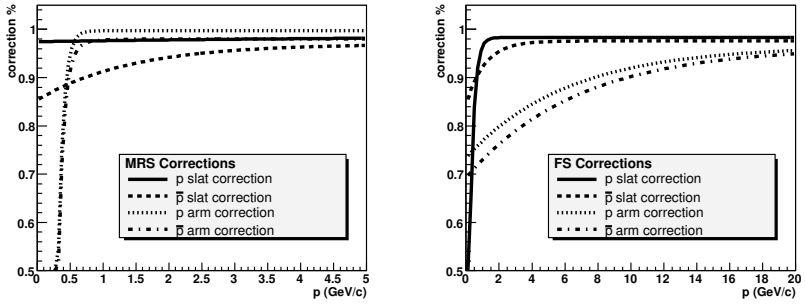

Figure 6.1: The p and $\bar{p}$ correction functions for absorptions and scatterings in the trigger slats (slat corrections) and in the spectrometer arm (arm correction) from the 90° setting in the MRS arm and the 4° and 8° settings (identical) in the FS arm.

6.1.4 RICH Veto Contamination Correction

The RICH may be used to identify protons below proton threshold by selecting particles above kaon (and by extension pion) threshold that did not emit Cerenkov light. These proton samples may, however be contaminated by pions and kaons whose rings are not detected by the RICH. By using estimates of the RICH efficiencies for pions and kaons the contamination of the protons spectra from these particles may be estimated. This correction depends on the composition of particle yields and cannot be factorized out, but must be treated separately. The only setting where this is relevant is the 8 degree setting. These corrections have been included in the 8 degree proton sample and are described in more detail in section 7.2.2.

6.1.5 Feed-down corrections

Feed-down Corrections are the corrections from the effects of the decay of heavier, unstable particles into the particles which are detected. Some of these will cancel each other out, but decay of Λ and $\bar{\Lambda}$ to p and $\bar{p}$ might influence the measured $\bar{p}/p$ ratio. Feed-down corrections have not been included in this analysis, since they have not been included in other publications, with which it is

natural to compare the results obtained here. I have estimated the systematic uncertainty contribution from Λ to p feed-down in section 7.3

6.1.6 Other Corrections

There are several other effects which may have an impact on the spectra, but which will cancel out in the ratios:

Pid and Tracking efficiencies might vary from run to run depending on malfunctions of various detector parts and the quality of the calibrations. (Some calibrations are not done on a run-by-run basis, but only periodically.) The negative and positive data from the MRS arm are both from the same runs, making most of the variations equal for both particle charges. In the FS arms the effects of these variations will only affect the data from one particle charge. I have therefore omitted runs which show a discrepancy in the yields compared with most of the other runs in the same setting. (Details in sections 7.2.2 and 7.2.3)

In Flight decay corrections would take care of errors which may occur because a particle is decaying before it has traversed the entire spectrometer, this is only relevant for pions and kaon. These effects are identical for both charges of pions and kaons and will cancel out in the ratios.

Knock-out protons The contribution from knock-out protons due to interactions with the beam-pipe has been found to be less than 2 per cent for p_{T} $\sim$0.5 GeV in the MRS and falling rapidly with increasing momentum. In the FS this contribution has been found to be negligible [44]. The effect of knock-out protons have not been considered further in this work.

Dependence of absorption on FS angle The same absorption function has been used for both 8° and 4° FS angles. At the forward angles more protons and anti-protons are absorbed in the beam-pipe due to longer path lengths through the pipe wall; this effect is slightly stronger for the anti-protons. The impact of this angular dependence on the $\bar{p}/p$ ratio has been found to amount to less than one per cent [45] for the p_{T} region of interest.

6.2 Normalization and Correction Implementation

I have used two slightly different methods for the implementation of normalization and corrections, depending on whether acceptance correction were necessary or not.

6.2.1 With acceptance maps:

The procedure for extracting the particle densities $\frac{d^2N}{dydp_T}$ I have used is the same as the one described in [45]. The main idea behind this algorithm is to give the data from each cell a weighting factor which is the inverse of its correction factor; this is done to ensure that data with a high correction is given a low weight. I implemented this by storing the raw data $\frac{d^2n}{dydp_T}$ and the correction factors $\mathrm{CORR}(y,p_T)|_i$ in two independent histograms for each vertex bin. The true particle density averaged over all vertex bins is then given by:

$$\frac{d^2N}{dydp_T}^{\pm} = \frac{\sum_i \frac{d^2n^{\pm}}{dydp_T}|_i \cdot \mathrm{CORR}^{\pm}(y,p_T)|_i \frac{1}{\mathrm{CORR}^{\pm}(y,p_T)|_i}}{\sum_i \frac{1}{\mathrm{CORR}^{\pm}(y,p_T)|_i}} \tag{6.7}$$

which factorizes into two independent sums, one over the data cells and one over the correction factors.

$$\frac{d^2N}{dydp_T} = \Big(\sum_i \frac{d^2n^{\pm}}{dydp_T}|_i\Big) \times \Big(\sum_i \frac{1}{\mathrm{CORR}^{\pm}(y,p_T)|_i}\Big)^{-1} \tag{6.8}$$

The transverse momentum distribution $\frac{dN}{dp_T}|_y$ may the be projected out for a narrow rapidity region Δy

$$\frac{dN}{dp_T}|_y = \Big(\sum_y \sum_i \frac{d^2n^{\pm}}{dydp_T}|_i\Big) \times \Big(\sum_y \sum_i \frac{1}{\mathrm{CORR}^{\pm}(y,p_T)|_i}\Big)^{-1} \tag{6.9}$$

The sum is taken over all cells where the data sets of the charges overlap, i.e where the acceptances are non-vanishing and within the PID limits of both charges.

6.2.2 Without acceptance maps:

When there is data from both polarities and the acceptance corrections cancel out the ratio in one vertex bin is given by

$$R(y,p_T)|_i = \frac{\frac{d^2n^-}{dydp_T}|_i \cdot \frac{Norm^-|_i}{Abs^-(p(y,p_T))}}{\frac{d^2n^+}{dydp_T}|_i \cdot \frac{Norm^+|_i}{Abs^+(p(y,p_T))}} \tag{6.10}$$

where $Abs^{\pm}(y,p_T)$ is the correction for absorption in the beam-pipe, spectrometer arm and trigger slat, which show significant charge dependence for the proton and anti-proton samples only. To obtain the ratio averaged over all vertex-bins I have compensated for the vertex dependence of the acceptances by scaling the negative polarity data with a factor $Norm^-|_i/Norm^+|_i$. This is done to compensate for the effects arising from differences in the vertex-distributions, which vary from run to run. In this way the particle data of opposite charge

from same vertex bins, and hence with the same geometrical acceptance, will have the same total weight in the average estimate for both particle charges. The ratio summed over all vertex bins and a narrow rapidity region is then given by:

$$R(p_{\mathrm{T}})|_y = \frac{\sum_y \sum_i \frac{d^2n^-}{dydp_{\mathrm{T}}}|_i \cdot Abs^-(p(y,p_{\mathrm{T}})) \cdot \frac{Norm^-|_i}{Norm^+|_i}}{\sum_y \sum_i \frac{d^2n^+}{dydp_{\mathrm{T}}}|_i \cdot Abs^+(p(y,p_{\mathrm{T}}))} \tag{6.11}$$

where I have used $Abs(y,p_{\mathrm{T}}) = 1$ for $\pi^{\pm}$ and $K^{\pm}$.

Chapter 7

Ratios and systematic uncertainties

In this chapter I will present the analysis details for each setting and the results that this analysis have yielded. In the last section I discuss contributions to the systematical errors arising from the various cuts that I have done to the data set. The data set available from the MRS spectrometer are from 90 and 40 degrees. From the forward arm there is data from two polarities at 8 and 4 degrees.

7.1 MRS Data

The Mid-rapidity Arm is shorter and simpler than the long FS-arm. It has only one magnet and the two tracking chambers on either side of it are placed with center axes along the center-axis of the D5 magnet, as opposed to the FS arm which has tracking detectors that are placed so as to conform to the curved path of a charged particle traversing the magnets. We therefore have data from both particle charges at either magnet-polarity, making it possible to extract ratios from data from one singular setting. Ideally we would have had data from both polarities to make the data perfectly overlapping in (y, p_{T})-space, but this is not the case and I have been able to extract reasonable results from the positive polarity data available from the 90 and 40 degree settings.

7.1.1 Run selection in the MRS arm

The detector efficiency varies from run to run. Low efficiencies can be caused by malfunctioning detector parts or poor calibrations. Since the data of both charges from the MRS arm are from the same runs most variations in the detector-efficiencies will affect both particle charges.

One variable, which is hard to calibrate very well, and which may have a

huge impact on the data in the MRS arm is the INEL vertex calibrations. As mentioned in section 6.1.1 the normalization is based on the number of INEL events in a vertex bin (5cm), while the particles in the MRS arm are assigned a vertex bin according to their track vertex V_z. Poor INEL calibrations can cause a systematic deviation between the INEL vertex and the track vertex positions. This will lead to errors when the data are normalized.

In figure 7.1 I have plotted the gaussian fits to the (INEL vertex - V_z) difference for all the runs in the 90-degree setting (these are used in the pointing cuts, section 5.5). The error bars are the widths of the fits (1 sigma). The distributions should be, and are, typically centered around zero. All the runs except 2 have centers within $\pm 2cm$ and I have included all but those two, in my analysis. (Analysis redone with narrower cut for estimation of systematic uncertainty contributions, section 7.3).

A similar run selection was done for the runs in the 40 degree setting.

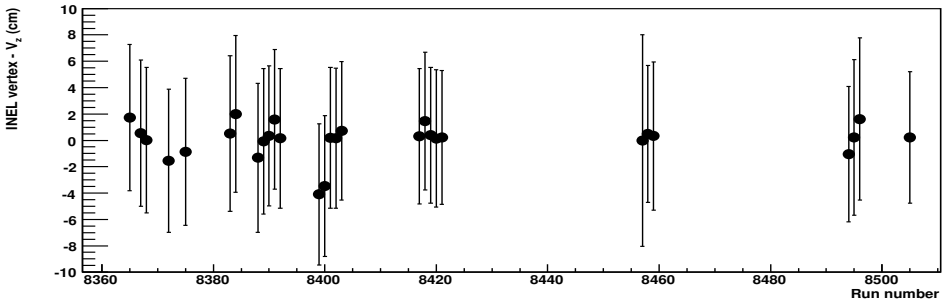

Figure 7.1: Centroids of Gaussian fits to the INEL vertex - V_z difference for the runs in the 90 degree setting. Error bars are the widths (one σ) of the fits.

7.1.2 90 degrees, 1050 A magnet current setting

The 90 degree setting is special because of its geometric symmetry around z=0. This enabled me to extract ratios in two different ways. In the first case I use the symmetry to overlay data from 'opposite' phase-space areas. In the second case I use acceptance maps to correct the differences in the overlapping region.

The symmetric case:

In the 90 degree setting the MRS-TPCs and magnets are placed symmetrically around the global x-axis at $z = 0$. This makes the acceptance as function of rapidity, transverse momentum and the vertex position symmetric around the axes $z = 0$ and (rapidity) $y = 0$ for the two particle charges. In mathematical terms:

$$Acc^{-}(-y, p_{\mathrm{T}}, -z) = Acc^{+}(y, p_{\mathrm{T}}, z) \tag{7.1}$$

This symmetry is illustrated in figure 7.2. Unfortunately this symmetry is not perfect. The TOFW in itself is not quite symmetric around $z = 0$, in addition the region of instrumented TOFW slats is extended good way further in the positive z-direction than is the case in the negative direction. There were also several slats that malfunctioned during various runs. By selecting only the tracks that hit a slat with a properly working 'mirror-slat', i.e. an instrumented and properly functioning slat at the opposite z-coordinate, I was able to symmetrize the wall to some extent. However, the z-axis is situated one-quarter of a slat into slat number 74 (centered at z=0.51cm with slat number 73 centered at z=-0.74cm). In my symmetrization algorithm I have considered slat nr 74 to be the mirror-slat of slat nr 73, nr 75 is the mirror of 72 and so on, as this is the symmetrization where the offset between the z and $-z$ coordinates of mirror-slats will be the lowest. Making slat nr 74 the center slat and slat nr 75 the mirror slat of slat nr 73 is the second-best solution. Slat nr 75, however is placed at 1.7cm, which is not as good a match with 73's coordinate.)

The symmetry may be additionally distorted by asymmetries in the TPC efficiencies due to non-uniform pad behaviour. These are often asymmetric around $z = 0$, which means that the negative and positive particles from opposite vertex bins will be influenced differently.

An implicit assumption in the symmetry method is that the physics, in particular chemical composition and yields, remains constant over the narrow rapidity interval probed.

Results

The results from this extraction method are shown in figure 7.3. The figures show (y, p_{T}) distributions with lines indicating the borders of the rapidity regions used in extracting the ratios as function of p_{T} .

The pion ratios descend from well above 1 at the low p_{T} , flattening out at $\pi^-/\pi^+ \sim 1$. This effect is probably due the the extra quarter slat at the left end of the TOFW (which is the end to which the negative particles are bent by the magnetic field), or a combination of this effect with asymmetries in the TPC efficiencies. I have redone the analysis using the alternative, less symmetric symmetrization (see figure 7.4) and in this case the pion ratios show no such descent at low p_{T} . In this case the offset in the z-coordinates of mirror slats is larger but in the opposite direction. The π^-/π^+ is very stable in the entire p_{T} range which may suggest that the two asymmetrical effects cancel each other out for the pions in this case.

Before the average sum over all vertex-bins were made the ratios were calculated bin by bin (from opposite vertex regions) to check for a dependence of the ratios on vertex-bin. The results for the pions are shown in figure 7.2. They show no significant vertex dependence, which may be taken as a sign that the extra fraction of a slat on the negative side of the TOFW has little effect and

that the opposite rapidity regions are more or less equivalent.

When summing over vertex bins I used the method described by equation 6.11. Since I am using data from opposite vertex bins the scaling $Norm^{+}(i)/Norm^{-}(i)$ with which the negative data were scaled in equation 6.11 was modified. Because there is data from only one polarity, it is not possible to use that scaling method. The normalization scaling was modified into $Norm(i)/Norm(\bar{i})$, where $\bar{i}$ is the vertex bin symmetrically opposite to bin i mirrored around $z = 0$. In this way the negative sample from vertex bin i is scaled with the normalization factor for events in the bin where the corresponding positive particle's acceptance is the same, according to the symmetry considerations. Equation 6.11 then turns into:

$$R(p_{\mathrm{T}})|_y = \frac{\sum_i \sum_y \frac{d^2n^-}{dydp_{\mathrm{T}}}|_i \cdot \mathrm{Abs}^-(y, p_{\mathrm{T}}) \cdot \frac{Norm(i)}{Norm(\bar{i})}}{\sum_i \sum_y \frac{d^2n^+}{dydp_{\mathrm{T}}}|_i \cdot \mathrm{Abs}^+(y, p_{\mathrm{T}})} \tag{7.2}$$

the independence of the ratios on p_{T} have enabled me to fit straight lines to the distribution, thus getting an estimate of the average ratio at that rapidity. The results of these fits are listed in table 7.1.

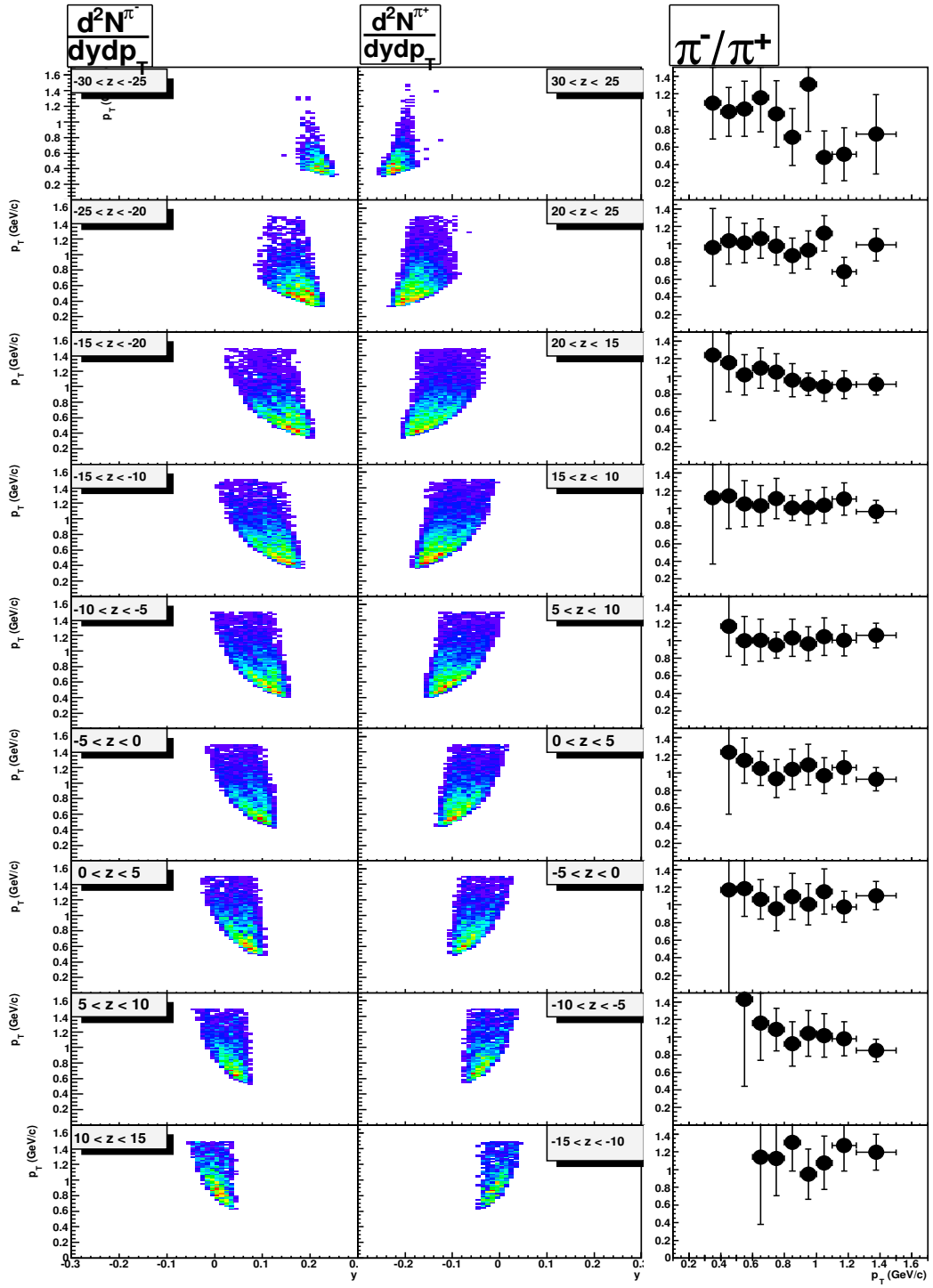

Figure 7.2: π^- (left) and π^+ (center) (y, p_{T}) distributions from the indicated vertex ranges. To the right are the π^-/π^+ ratios from the opposite but equivalent vertex regions. The negative polarity data have been scaled according to equation 7.2.

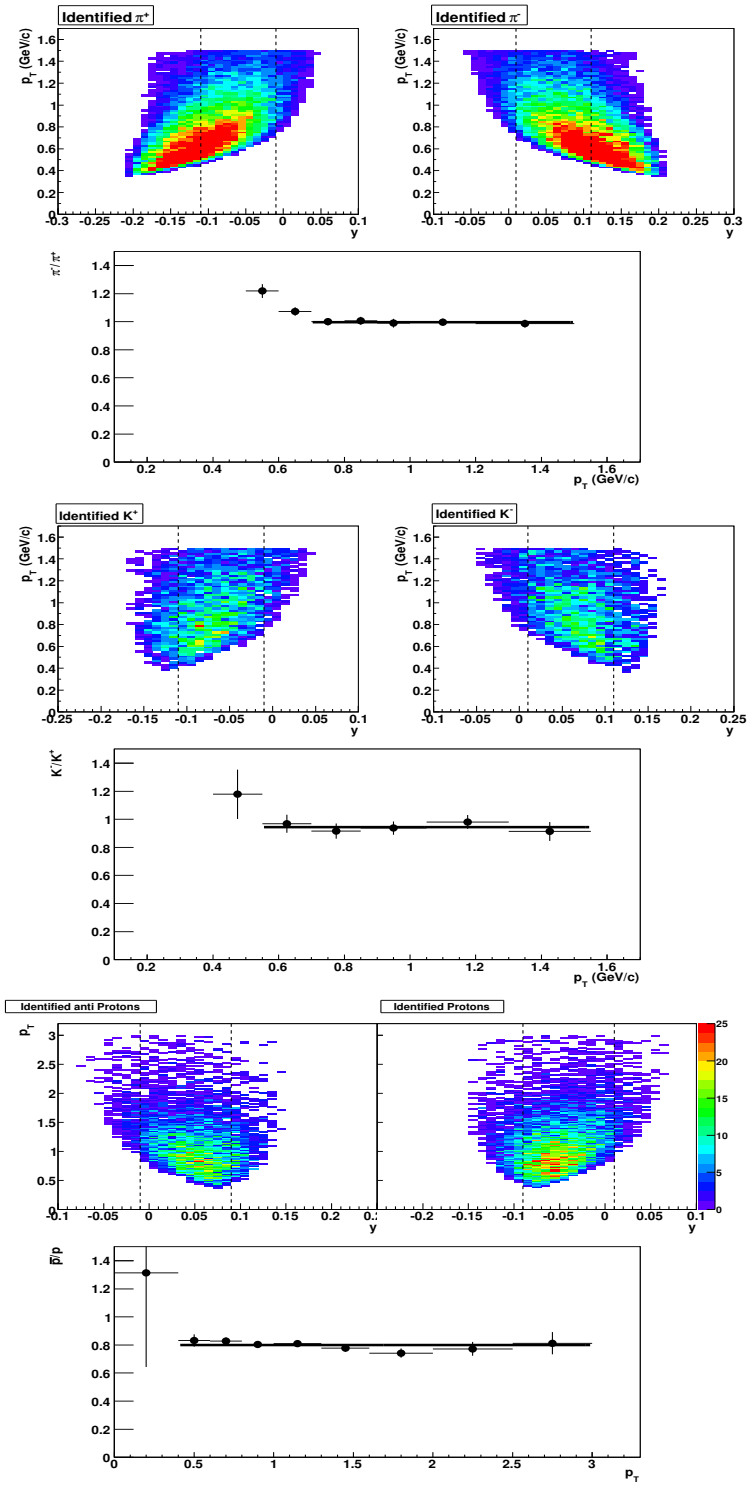

Figure 7.3: Pion, kaon and proton data averaged over vertex bins according to equation 7.2, i.e positive data are raw sums while negative data in each bin have been scaled. The dotted lines indicate the rapidity regions included when extracting the ratios. Fit results are listed in table 7.1.

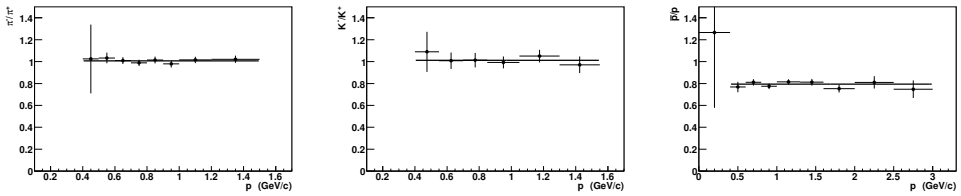

Figure 7.4: Ratios extracted using alternative TOFW symmetry as described in the beginning of this section. Pion and proton ratios unaltered (fit difference is in the order of 1 per cent) kaons at 1.0 which is $\sim$ 5 per cent higher than the result with original symmetry method at 0.94, result using acceptance corrections is at $\sim$ 0.92

Acceptance corrected

With acceptance files the procedure is more straightforward and ratios are extracted according to equation 6.9. The impact that the asymmetric TOFW has on the spectra is corrected for by the acceptance correction factor. The problem with this procedure is that the actual overlap in phase-space of the two particle charges is very small, leading to poor statistics. this is especially the case for the mesons. The 90 degree results with acceptance corrections are shown in figure 7.5

As may be seen from table 7.1 correspondence between the ratios extracted with the symmetry algorithm and using acceptance corrections is excellent.

7.1.3 40 degrees, 2000 A magnet current setting

The data from the 40 degree setting have been extracted in the same way as the 90 degree setting. In this setting there is no symmetry in the acceptances of the negative and positive particles, but with acceptance corrections the spectra in the overlapping areas may be used to extract ratios. The biggest problem is the very small area of overlap.

The results from the 40 degree setting are shown in figure 7.6.

Extrapolations

As may be seen in figure 7.6 the fraction of the data that actually overlaps is very small. In an attempt to extract something from the other parts of the data I made p_{T} -distributions from narrow rapidity-slices (0.05 units of y). The idea is to try to make fits to the p_{T} -distribution in the rapidity-area where the particle-distributions cover a wide area in the p_{T} direction. By computing the ratios of the distributions from different rapidity-regions separated by δy,

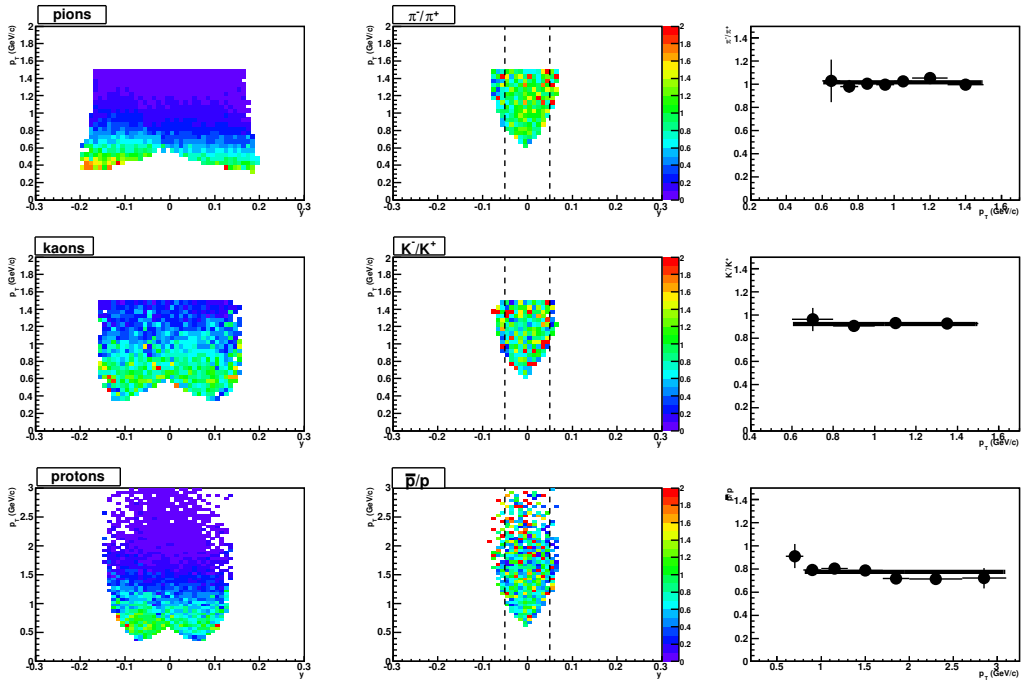

Figure 7.5: The results from 90 degrees with acceptance corrections. In the leftmost panels are (y, p_{T}) plots summed over all vertexbins and acceptance-corrected. In the center are the ratios of the acceptance corrected y, p_{T}-distributions. Finally in the rightmost panels are the ratios of the negative to the positive p_{T} distribution extracted over the rapidity region indicated by dotted lines. Fit results are listed in table 7.1.

and let δy approach zero might then give an indication of what the ratio of the overlapping area should be. The spectra are, however, not wide enough nor of sufficient statistical quality to make trustworthy extrapolations.

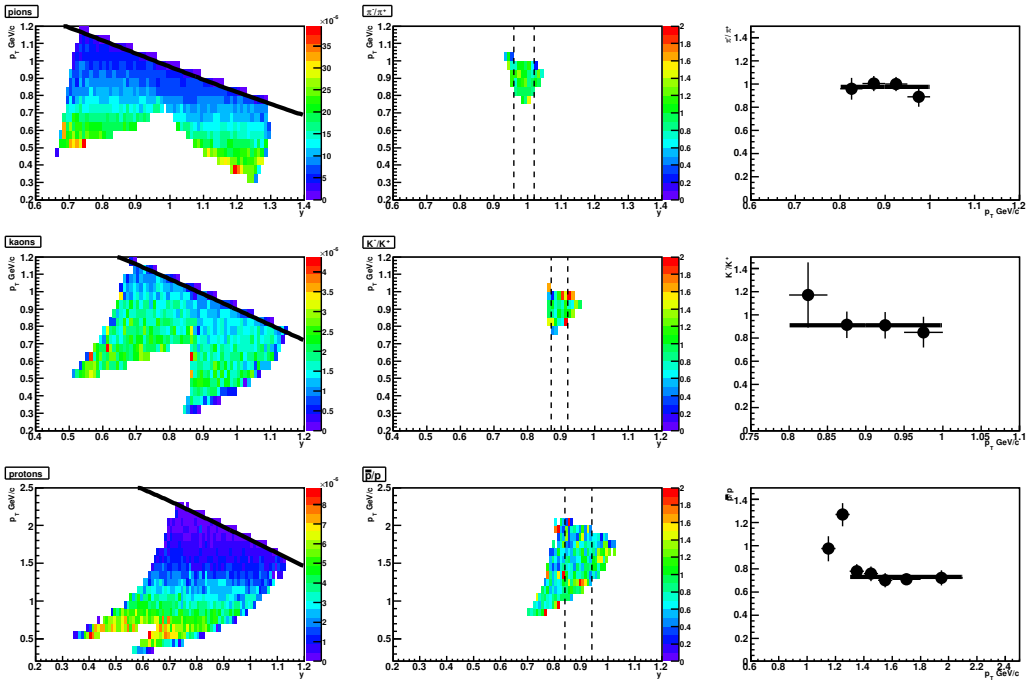

Figure 7.6: The 40 degree data with pions on top, kaons and finally protons in the lower row. Fit results are listed in table 7.1

Results from MRS				
	Midrapidity			40 degree
	Acceptance corrected $y \sim 0$	**Symmetric case** $y \sim (\pm)0.5$	$\frac{\sum_i R_i \cdot \frac{1}{\Delta R_i}}{\sum_i \frac{1}{\Delta R_i}}$	$y \sim 1.0$
π^-/π^+	1.01 ± 0.02	1.00 ± 0.01	1.00 ± 0.01	0.98 ± 0.04
K^-/K^+	0.92 ± 0.02	0.95 ± 0.02	0.94 ± 0.01	0.91 ± 0.07
$\bar{p}/p$	0.77 ± 0.02	0.79 ± 0.01	0.80 ± 0.01	0.73 ± 0.03

Table 7.1: Result from the straight lines fitted to the ratios as function of p_{T} in figure 7.3. The errors are statistical only.

7.2 FS Data

The available data sets from the forward arm are from the 8° and 4° settings. With the small angle between the beam direction and the spectrometer arm the uncertainty of the z-coordinate of the track projection back through the D1 magnet to the interaction region is quite large, while the z-dependence of the geometrical acceptance is weaker than for the MRS. In the FS arm I have therefore used the INEL vertex when assigning the particles to a vertex bin. To verify the quality of the INEL-vertex calibrations I have checked the distribution of (INEL vertex - V_z) differences using V_z from MRS tracks for the runs used in the FS settings. Because of the scarcity of available runs I have included the runs where the centroids of this distribution is not centered close to zero. For this purpose I have added a factor z_{off} which is the z position of the (INEL vertex-V_z) centroid. For all the events in a run the INEL-vertex is recomputed to:

$$\text{INELvertex}_{\text{new}} = \text{INELvertex}_{\text{old}} - z_{off} \tag{7.3}$$

In this way the INEL vertex is corrected for the systematic discrepancy with the MRS track vertex.

The vertex bin widths used in the FS arm are 5cm.

7.2.1 FS run selection

Since the FS negative and positive charge data come from different runs, temporary malfunctions and poor calibrations will only affect one particle charge. To get an estimate of how well the FS detector arm was working during the various runs I have compared the number of particles detected in various parts of the detector per INEL event. Runs that stand out as having significantly fewer particles per event, or fewer particles in the BFS relative to the FFS compared to the majority of runs have been excluded from the sample. The details are discussed in the separate setting sections.

7.2.2 8° Quarter field

Run selection

In figure 7.7 I have plotted the number of identified pions, kaons and protons together with the number of matched tracks through D2 (FFS tracks), all normalized to the number of INEL-events. The first four runs are the positive polarity runs, whereas run number 8514 is negative polarity. As may be seen from the plot the number of FFS tracks, pions and protons increase systematically from run number 8494 to run number 8505. This effect is probably due to the variation in the z-distributions of INEL vertex events, which are centered at $z \sim 22cm$, $z \sim 16cm$, $z \sim 8cm$ for runs 8494, 8495 and 8496 respectively,

whereas the center of the vertex distribution in run number 8505 is centered at $z \sim 1cm$ which is almost identical with the center from the negative polarity run at $z \sim -3cm$. The geometrical acceptance varies as function of z making the total number of particles per event vary with the distribution along the z-axis. By dividing the spectra into vertex-bins this should be taken care of. However, the ratios vary significantly with the inclusion of the first three runs as opposed to using only run number 8505 from the positive polarity setting. The inclusion of data from the other runs introduces a strong p_{T} dependence in the ratios, see e.g figure 7.12. I am uncertain about the origin of this effect, but have used only run number 8505 from the positive polarity data in the analysis. The effect of this cut has been included in the estimation of the systematic uncertainties.

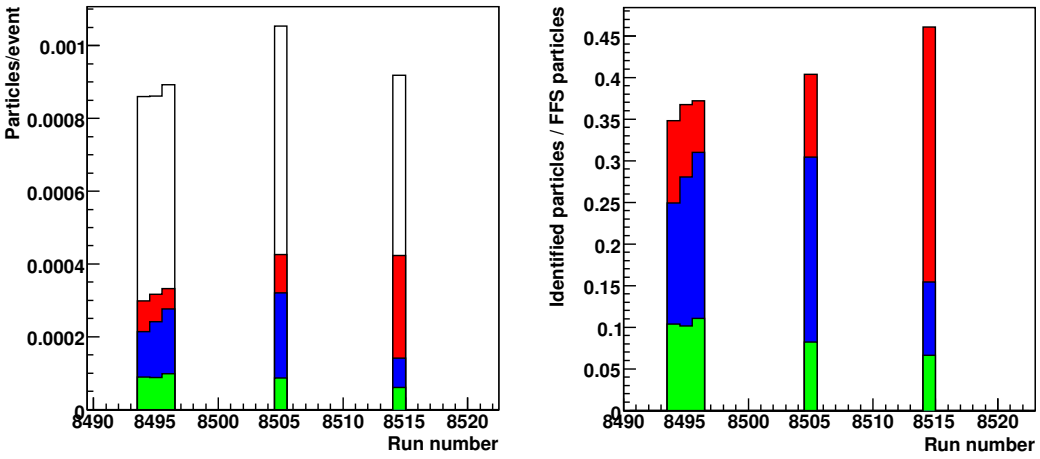

Figure 7.7: Left: The number of FFS tracks (white), pions (red), kaons (green) and protons(blue) per INEL-event for the runs in the 8 degree setting. Right: The number of identified particles per FFS track. The kaon and proton yields have been scaled by a factor 20 to make them visible on the plots.

Proton Contamination Correction

The protons identified by having momenta between kaon and proton threshold and no ring in the RICH readout plane may be contaminated by pions and kaons whose rings are not detected. In figure 7.8 I have plotted the RICH detection efficiency as function of pion momentum.

This function may be converted into efficiency as function of β which will be valid for all particle species by inserting the pion mass into the following

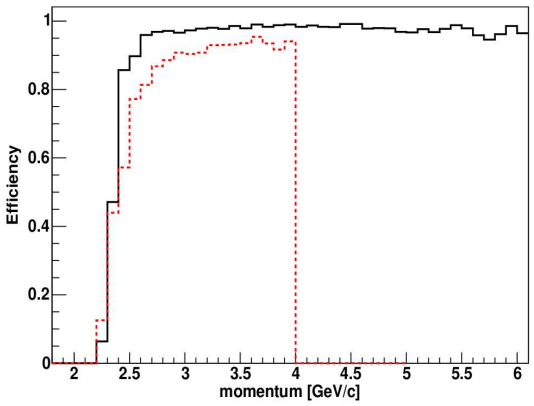

Figure 7.8: RICH pion efficiency as function of momentum (black line) estimated from simulations and pions in H2 (red dotted line). Figure from [14].

equation:

$$\beta = \sqrt{\frac{p^2}{m^2 + p^2}} \tag{7.4}$$

The detection efficiency for a species i with mass m_i may then be expressed as $\varepsilon(\beta(p, m_i))$, converting the particles momentum p_i into β according to equation 7.4.

The p_{T} distributions of the contamination contributions from pions and kaons with no RICH ring is found for each bin in the (y, p_{T}) plane by scaling the cell count of identified pions and kaons $n_{raw}(y, p_{\mathrm{T}})$ with the factor $\frac{1-\varepsilon(\beta(p,m_i))}{\varepsilon(\beta(p,m_i))}$ yielding the contamination contribution from the cell $n_{cont}(y, p_{\mathrm{T}})$ of particle species i as

$$n^i_{cont}(y, p_{\mathrm{T}}) = n^i_{raw}(y, p_{\mathrm{T}}) \cdot \frac{1 - \varepsilon(\beta(p, m_i))}{\varepsilon(\beta_i(p, m_i))} \tag{7.5}$$

Since the rapidity of a proton with momentum p and transverse momentum p_{T} is different to the rapidity of a pion or kaon with the same p and p_{T} the rapidity-region over which the contamination spectra were extracted were defined by converting the rapidity of a cell to the rapidity the particle would have had if it were a proton. By picking particles whose converted rapidity y_p were within the rapidity range used to extract the $\bar{p}/p$ ratio, the p_{T} distributions of the calculated contaminations could be projected out. The contamination p_{T} spectra from pions and kaons were then subtracted from the anti-proton and proton p_{T} distributions before the $\bar{p}/p$ ratio was computed. The projected yields of protons and anti-protons before subtraction are shown in figure 7.11 together with the respective contaminations from pions and kaons.

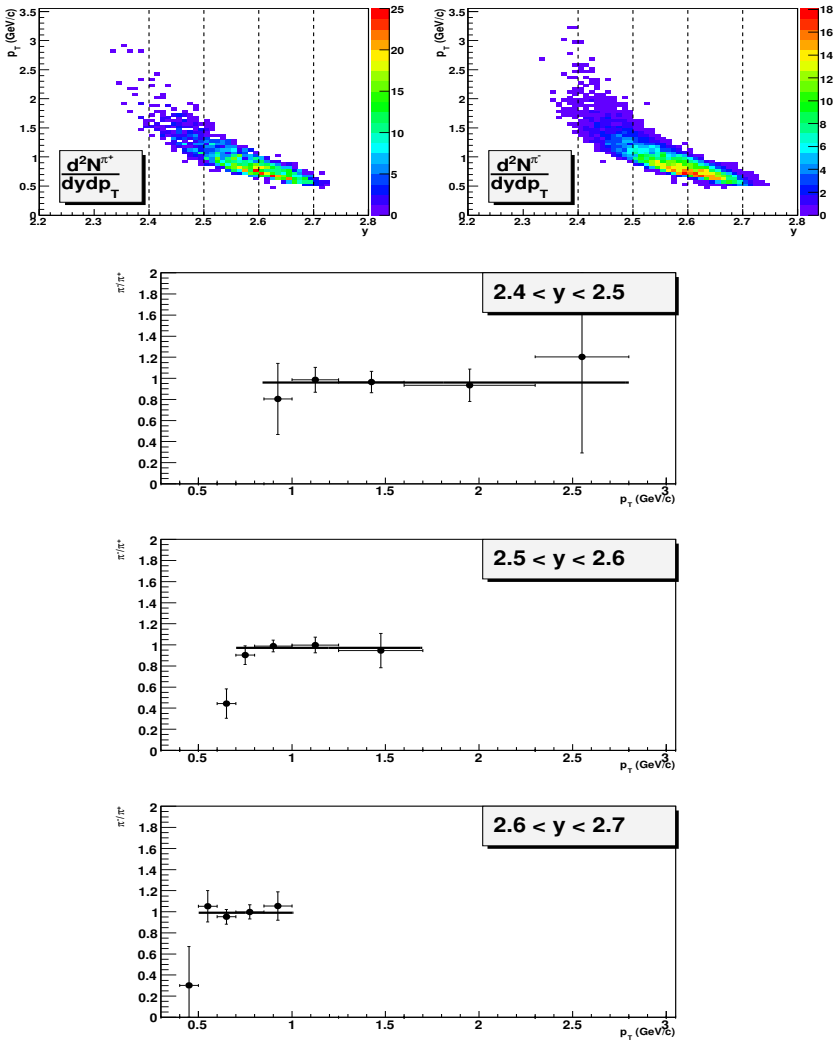

Figure 7.9: Top: (y, p_{T}) distributions for Pions summed over all vertex bins where the negative data have been weighted according to equation 6.11. The lines indicate the rapidity regions over which ratios have been extracted. Below are the π^-/π^+ ratios in the indicated rapidity regions.

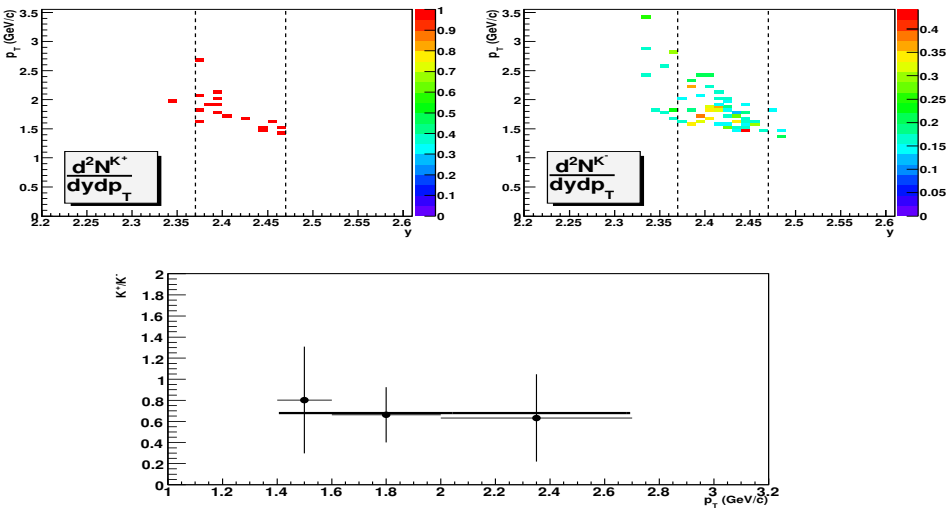

Figure 7.10: Kaon results at 8 degrees summed over all vertex bins according to equation 6.11. Ratio extracted in region indicated by dotted lines. Fit result is listed in table 7.2

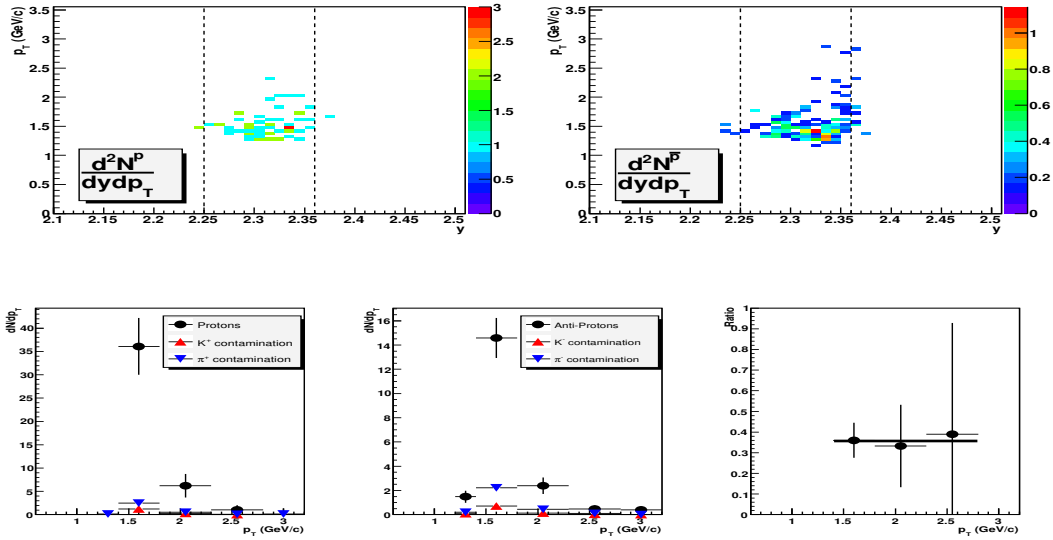

Figure 7.11: Proton results at 8 degrees summed over all vertex bins according to 6.11. (y, p_T) distributions in upper row. The p_T distribution of positive and negative kaons with the respective contaminations from pions and kaons in the lower left and center panels. In the lower right panel is the $\bar{p}/p$ ratio computed after the subtraction of the contamination functions from the p_T distributions. Fit result is listed in table 7.2.

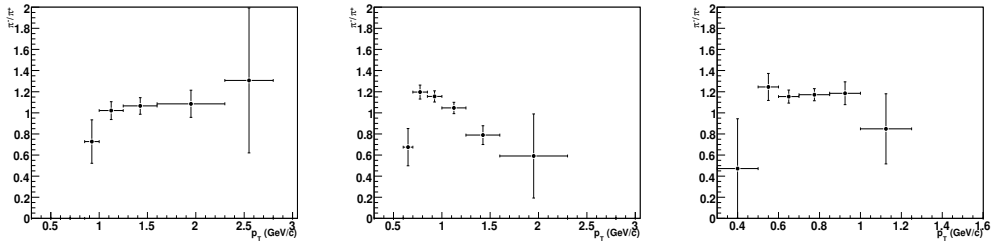

Figure 7.12: Pion results in the 8° setting with the inclusion of run number 8496 in the positive polarity data. The rapidity and p_{T} independence observed using only run number 8505 from positive polarity is no longer present. The lower rapidity bin is least influenced, but have systematically higher values than with the results in 7.9. The middle rapidity bin shows a strong p_{T} dependence and the higher rapidity bin, which is most severely changed, show more or less flat π^-/π^+ ratio at 1.16. This behaviour is different from what is observed in all other settings, and I therefore assume that these are not physical effects.

7.2.3 4° full field

Run selection

In the period when the FS spectrometer was placed in the 4 degree setting at negative polarity magnet current setting the T3 tracking chamber was malfunctioning. Because of this track-matching through the D3-magnet had to be done using track-extrapolations from T2. In figure 7.13 I have plotted the number of FFS-track per INEL event together with identified particles of each species per INEL event. The number of FFS particles per event is very stable throughout the entire range of runs, while the number of identified particles per event varies significantly. This discrepancy must arise from poor efficiencies in the rear parts of the FS arm. The positive polarity runs I have used are runs 8418-8422, 8524-8529 and run 8539. For the first four of these runs one of the RICH calibrations had a strange effect on the pions (see figure 7.14) which made it necessary to exclude these runs from the pion data. The effect only sets in at low momentum and high ring-radius, therefore leaving the kaons and protons more or less unaffected as seen from the figure. I have redone the analysis excluding these runs from the kaon and proton data as well and discovered no discernible systematic effect on the proton or kaon ratio, only a weakening of already poor statistics.

Of the negative polarity data I have used the runs where the BFS stand out as being significantly better than for the other runs. I have used the five best runs, i.e. run 8310, 8311, 8318, 8336 and 8367.

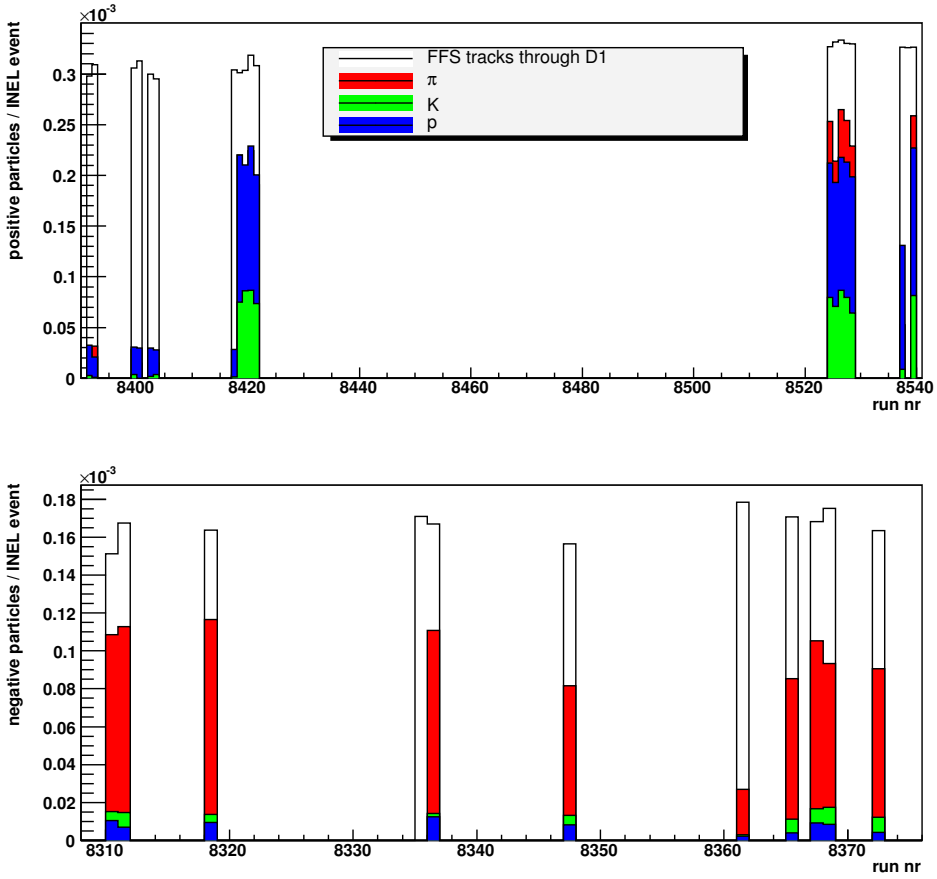

Figure 7.13: The number of identified FFS particles, pions (red), kaons (green) and protons (blue) per INEL event.

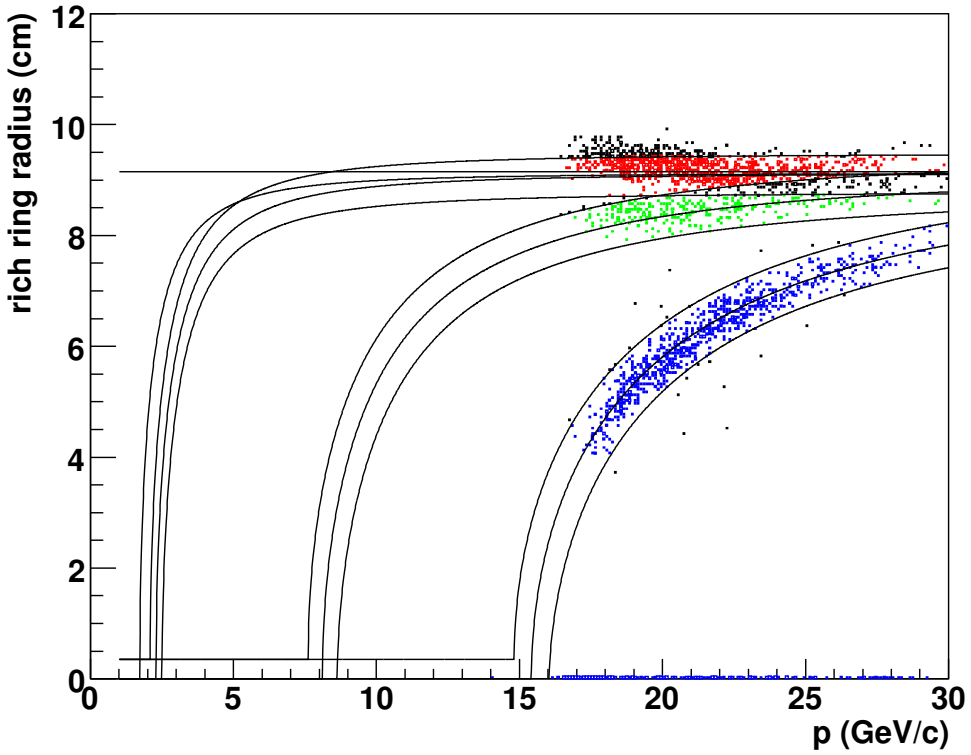

Figure 7.14: RICH PID from run nr 8418. At low momentum p the ring radius goes up and does not follow the expected behaviour as function of p. The kaon points also seem to start curving up slightly, but not to the same extent, thus leaving most of the kaons inside the PID curves.

Results

The pion and kaon data sets are distributed over a wide area in the rapidity-direction, but have narrow distributions in the the p_T direction. I have therefore extracted the ratios in several rapidity bins for these two particle species, whereas the proton set is only wide enough for one bin. The results are shown in figures 7.15, 7.16 and 7.17.

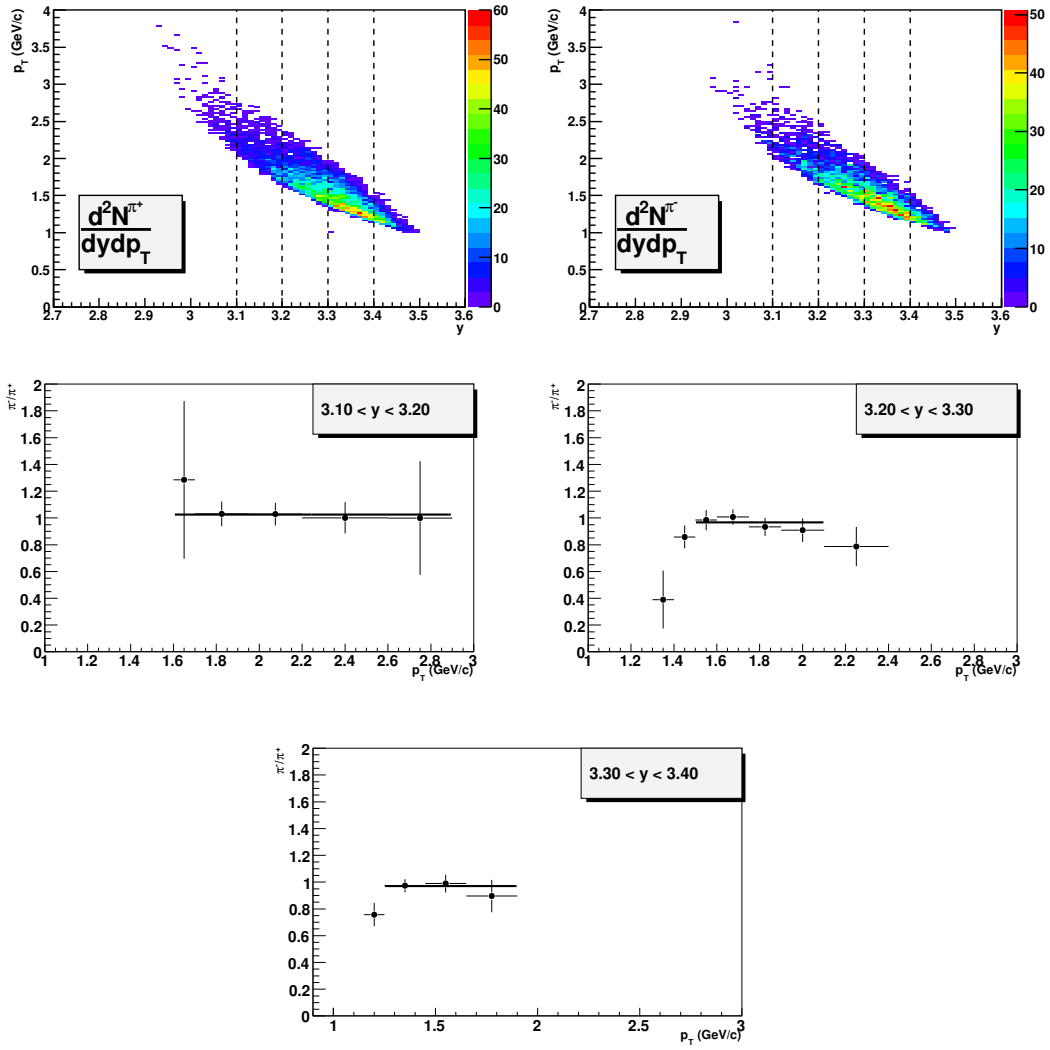

Figure 7.15: Top: (y, p_T) distributions of pions summed over all vertex bins according to equation 6.11. Dotted lines indicating y-regions over which ratios have been extracted. Fit values listed in table 7.2.

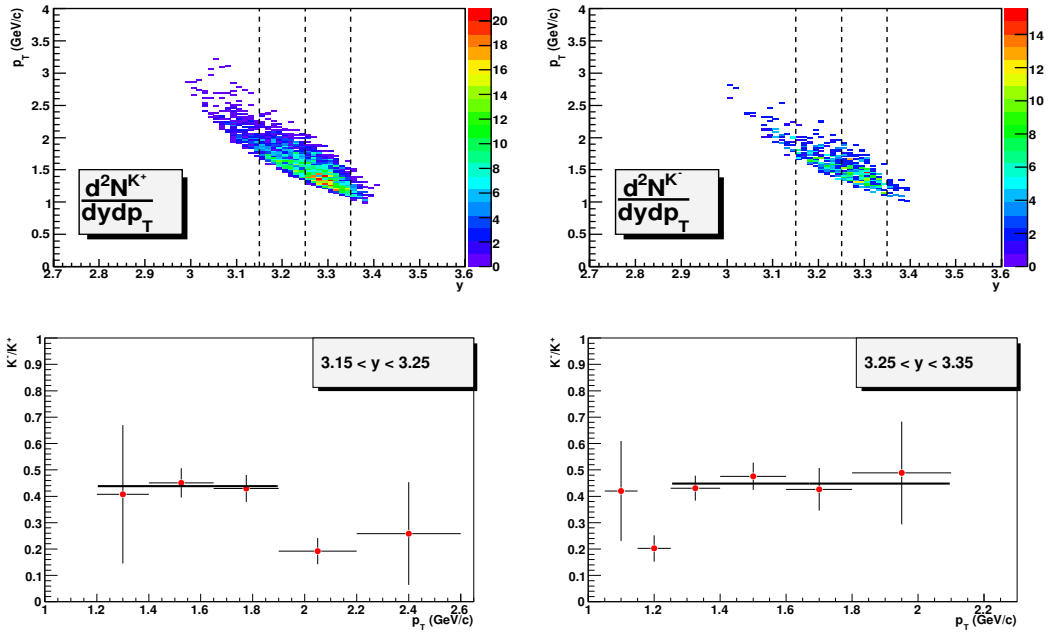

Figure 7.16: Kaon results from the 4 degree setting summed over all vertex bins according to equation 6.11. Fit values listed in table 7.2.

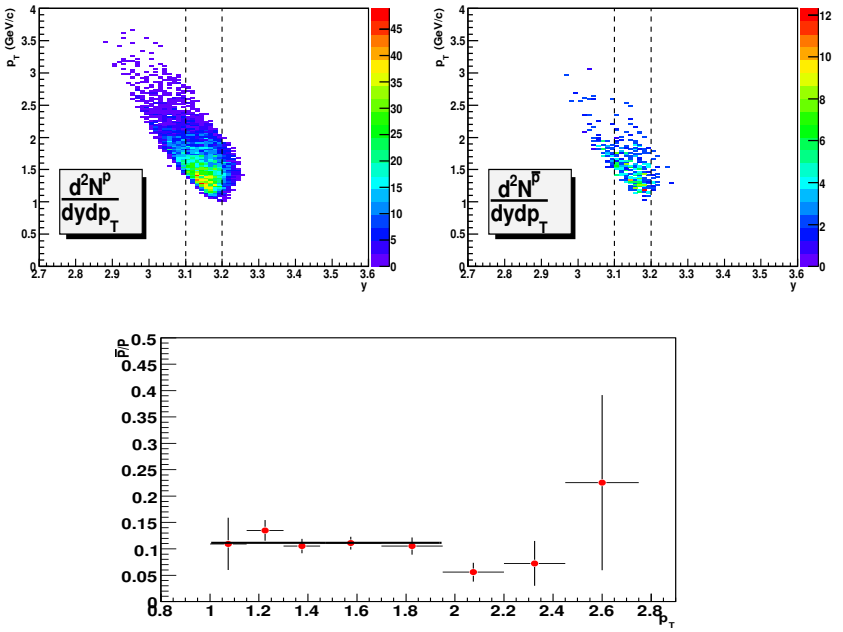

Figure 7.17: The 4 degree proton results summed over all vertex bins according to equation 6.11. Fit value listed in table 7.2.

8° Results

Pions		Kaons		Protons	
$y \sim$	fit	$y \sim$	fit	$y \sim$	fit
2.4<y<2.5	0.96±0.07				
2.5<y<2.6	0.97±0.05	2.42	0.68±0.19	2.30	0.36±0.08
2.6<y<2.7	0.99±0.04				
$\frac{\sum_i R_i \cdot (1/\Delta R_i)^2}{\sum_i (1/\Delta R_i)^2}$	**0.98±0.03**		**0.68±0.19**		**0.36±0.08**

4° Results

Pions		Kaons		Protons	
y range	fit	y range	fit	y range	fit
3.10<y<3.20	1.0±0.06	3.15<y<3.25	0.45±0.04	3.075<y<3.175	0.11±0.01
3.20<y<3.30	0.98±0.04	3.25<y<3.35	0.46±0.03		
3.30<y<3.4	0.97±0.04				
$\frac{\sum_i R_i \cdot (1/\Delta R_i)^2}{\sum_i (1/\Delta R_i)^2}$	**0.98±0.03**		**0.46±0.02**		**0.11±0.01**

Table 7.2: Fit results in the FS arm. Errors are statistical only

7.3 Systematic uncertainties

All the various cuts that have been made in the data set will have an impact on the outcome of the analysis. The systematic uncertainty from each cut can be estimated by the impact a change in the cut has on the final result. Below I have listed the various cuts I have made with a brief description of how the systematic uncertainty arising from the cut was estimated. The contribution on the systematic error from each on the various data sets are listed in table 7.4

Pointing Cuts I estimated the systematic uncertainty from the pointing cuts by increasing the widths of the elliptic pointing cuts with 1 σ (from 2.5σ to 3.5σ).

Rapidity Region The error contribution from the choice of rapidity region was estimated by moving the selected rapidity regions 0.02 units of rapidity in either direction.

p_T Fitting Range When making fits to the p_T distributions I have generally tried to extend the fit range over the entire range where the data are in agreement within the statistical error. I have estimated the contribution to the systematical error of the choice of p_T-range by shortening and lengthening the range by one bin on either side. The contribution will obviously be larger for data sets where the range is short, such as the points at $y \sim 1$.

Vertex Range of the Data used The range I have used varies within the data sets, in the MRS arm where the geometrical acceptance has the bigger dependence on the z-projection of a particle's trajectory I have chosen the vertex regions where the acceptance is non-vanishing over an extended area of (y, p_T) space and has a discernible plateau. In the FS-arm I have used the region from -40cm $< z <$ 40cm. Contribution to the systematic uncertainty was estimated by removing one vertex bin (5cm) on either side.

Vertex Binning I redid the FS analysis using narrower vertex binning (3cm) and wider (10cm). The effects were found to be negligible in both settings.

Slat symmetrization in the MRS (90 degree): When extracting ratios using the symmetry of the MRS-arm in the 90 degree setting I symmetrized the TOFW by making cuts in the data according to which slat in the wall had been hit. As mentioned in section 7.1.2 this symmetry was not perfect. In figure 7.4 I have plotted the ratios extracted with the alternative symmetry. The difference in fit result between the two choices of symmetry axis is taken to be the contribution to the systematic error from the symmetry method.

INEL-calibrations As mentioned in section 5.5 one of the variables included in the elliptic pointing cut in the MRS arm is the difference between the track-vertex and the INEL-vertex. As may be seen from figure 7.1 this distribution is generally centered at (INEL vertex - V_z) $\sim 0 \pm 2$ cm, but the distribution varies from run to run. In my analysis I have included all the runs that have the center of the distribution in the range from ± 2 cm (see fig 7.1). I have estimated the systematic uncertainty of this selection by reducing the accepted range to ± 1 cm.

FS run selection I have made cuts on runs in the FS-arm based on the number of detected particles per event, which is related to the detector efficiency. The various settings show meta-stable plateau, with some runs that stand out as less efficient than the rest. In the 8 degree setting I ended up with only one out of four runs (see section 7.2.2). In the 4 degree setting I estimated the systematic uncertainty of the run selection by excluding the runs with the lowest yields of the originally accepted i.e. run nr 8367 from negative polarity and runs 8525 and 8528 from the positive polarity setting. In the 8 degree setting the systematic error contribution was estimated by including run nr 8496 from the positive polarity setting, (see figure 7.12).

PID cut Error contribution estimated by increasing and narrowing the widths of the PID cuts by 20 per cent (increasing the uncertainty variables which define the PID-curves, see sections 5.6.1 and 5.6.2).

Acceptance cut As described in section 7.1.2 I cut away the edges of the acceptance maps by requiring acceptances above some limit. By varying this limit with about 25 per cent in either direction I estimated the effect of this cut on the data set.

Feed down

As mentioned in section 6.1.5 Λ and $\bar{\Lambda}$ particles may decay into p and $\bar{p}$, respectively. The fraction C of Λ and $\bar{\Lambda}$ decays giving rise to p and $\bar{p}$ that are detected as primary p and $\bar{p}$, respectively, has been estimated to be about 50% [45]. The influence on the measured $\bar{p}/p$ ratios, $\frac{\bar{p}_{obs}}{p}_{obs}$, can be expressed by:

$$\frac{\bar{p}_{obs}}{p_{obs}} \sim \frac{\bar{p}(1+C\frac{\bar{\Lambda}}{\bar{p}})}{p(1+C\frac{\Lambda}{p})} = \frac{\bar{p}\Big(1+C\frac{\Lambda}{p}(\frac{\bar{\Lambda}}{\Lambda})(\frac{\bar{p}}{p})^{-1}\Big)}{p(1+C\frac{\Lambda}{p})} \sim \frac{\bar{p}(1+C\frac{\Lambda}{p})(\frac{K^+}{K^-})}{p(1+C\frac{\Lambda}{p})} \tag{7.6}$$

where p and $\bar{p}$ are primary protons and anti-protons, and using the statistical model ansatz $\frac{\bar{\Lambda}}{\Lambda} \sim \frac{\bar{p}}{p} \cdot \frac{K^+}{K^-}$ (see section 2.4.1).

The contribution of feed-down protons in the measured proton spectrum $\varepsilon_{fd}(p_{\mathrm{T}}) = \frac{C\frac{\Lambda}{p}}{1+C\frac{\Lambda}{p}}$ has been determined through simulations for p+p data (figure

4.17 in [11]). Taking the probability $(C\frac{\Lambda}{p}) = \frac{\varepsilon_{fs}(p_T)}{1-\varepsilon_{fd}(p_T)}$ to be the same as for the p+p data system for the purpose of a very rough estimate, and using the K^-/K^+ ratio found this work interpolated to the rapidity where the $\bar{p}/p$ ratio was taken, the error may be estimated as listed in table 7.3.

The measured ratio $p_{obs}/\bar{p}_obs$ is higher than the true ratio, with the factor given in the last row as estimated by equation 7.6

No attempt has been made in this work to subtract the feed-down contributions from the p and $\bar{p}$ yields. Feed-down contributions to $\pi^{\pm}i$, mainly from the decay of K^0 and Λ, $\bar{\Lambda}$ have been found to be much smaller [46] and are not considered here. The data that I compare my results with in the concluding section also include feed-down contributions and suffer from similar systematic errors.

	90°		60°		8°		4°	
p_T (GeV)	~ 1	~ 2	~ 1	~ 2	~ 1	~ 2	~ 1	~ 2
$C\frac{\Lambda}{p}$	0.3	0.2	0.3	0.2	0.27	0.19	0.27	0.19
K^+/K^-	1.05		1.1		1.4		2.0	
$\frac{1+C\frac{\Lambda}{p}\cdot(\frac{K^+}{K^-})}{1+C\frac{\Lambda}{p}}$	1.01	1.01	1.02	1.02	1.08	1.06	1.2	1.16

Table 7.3: The estimated error in the $\bar{p}/p$ ratios from Λ feed-down for all the settings.

Data set →	90° sym			90° acc			40°			8°			4°		
Effect ↓	$\frac{\pi^-}{\pi^+}$	$\frac{K^-}{K^+}$	$\frac{\bar{p}}{p}$	$\frac{\pi^-}{\pi^+}$	$\frac{K^-}{K^+}$	$\frac{\bar{p}}{p}$	$\frac{\pi^-}{\pi^+}$	$\frac{K^-}{K^+}$	$\frac{\bar{p}}{p}$	$\frac{\pi^-}{\pi^+}$	$\frac{K^-}{K^+}$	$\frac{\bar{p}}{p}$	$\frac{\pi^-}{\pi^+}$	$\frac{K^-}{K^+}$	$\frac{\bar{p}}{p}$
Pointing Cut	0	1	0	0	1	0	3	3	3	4	4	4	3	1	1
Rapidity Region	2	3	3	3	5	3	3	8	5	6	6	6	4	4	5
p_{T} Fit Region	1	1	1	1	1	1	2	3	3	1	4	4	1	3	3
MRS Slat Symmetry	1	6	1	–	–	–	–	–	–	–	–	–	–	–	–
MRS INEL-V_z Cut	1	4	2	1	3	2	1	5	1	–	–	–	–	–	–
Vertex Range	1	1	1	1	3	2	2	3	2	1	4	3	1	1	1
FS Run Selection	–	–	–	–	–	–	–	–	–	8	7	7	5	7	6
PID Cut	1	1	1	1	1	1	1	1	1	1	7	–	5	2	2
Acceptance Cut	–	–	–	1	1	1	1	4	2	–	–	–	–	–	–
Λ Feed-down	–	–	1	–	–	1	–	–	2	–	–	7	–	–	18
$\sqrt{\sum_i e^2}$	**3**	**7**	**4**	**4**	**7**	**4**	**5**	**11**	**7**	**10**	**13**	**11**	**8**	**9**	**20**

Table 7.4: The contributions to the systematic uncertainties in per cent

Chapter 8

Conclusion

8.1 Rapidity dependence of ratios

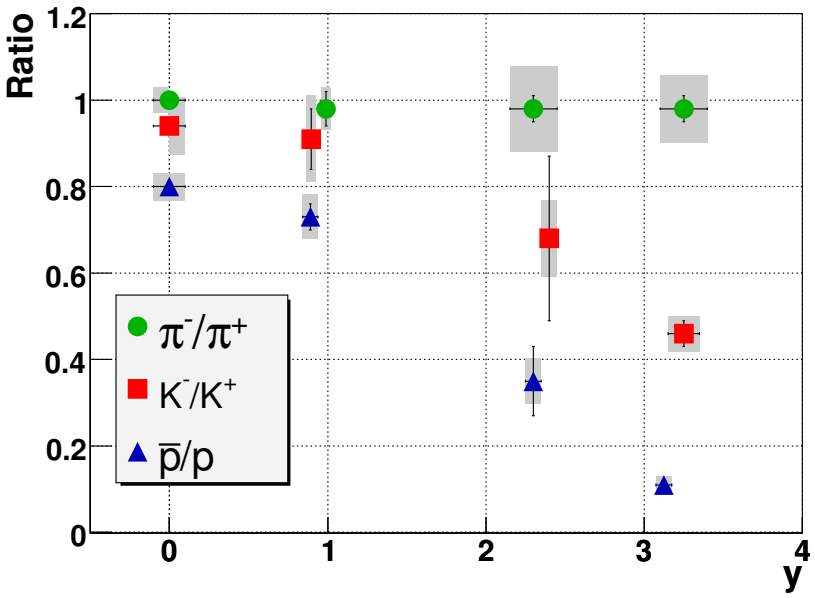

Figure 8.1: The results of the straight line fits as function of rapidity y for pions, kaons and protons. The shaded boxes signify the systematic error in each point. Vertical bars are statistical error, horizontal bars are the widths of the rapidity bins.

In figure 8.1 I have plotted the extracted pion, kaon and proton anti-particle to particle ratios as function of rapidity. In figure 8.2 I have plotted the results together with the corresponding ratios from p+p and Au+Au collisions which have been published by the BRAHMS collaboration in [47] and [44] respectively.

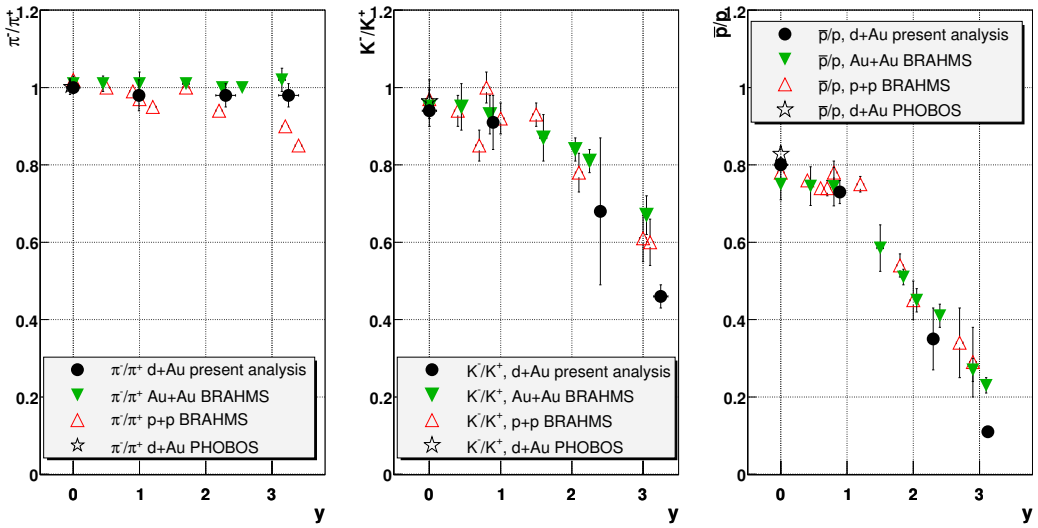

Figure 8.2: Comparison of the results from this dissertation with ratios in p+p and central Au+Au collisions published by BRAHMS in [47] and [44]. The PHOBOS points are from d+Au collisions at RHIC, published in [48] and summed over all centralities.

The π^-/π^+ ratio shows no rapidity-dependence, and is consistent with unity over the entire rapidity range from y=0 to y=3.2 as expected for an isospin symmetric projectile. This is consistent with the results from Au+Au collisions which are also flat at one over the entire rapidity range. The pion ratios from p+p collisions have a similar behaviour for rapidities below $y \sim 1.5$, but in the range where $y > 1.5$ the π^-/π^+ ratio drops below unity and decline steadily down to 0.85 at $y = 3.4$. This can be attributed to Isospin and charge conservation in the fragmentation region [44], an effect which is not present in d+Au collisions due to the isospin neutrality of the deuteron.

The $\bar{p}/p$ and K^-/K^+ ratios are both consistent with the results from p+p and Au+Au collisions in the rapidity range up to $y \sim 2$. The p+p and Au+Au results exhibit plateau-like behaviour from $y = 0$ up to $y \sim 1$, with independence of y in this range. The d+Au K^-/K^+ point at $y \sim 1$ is consistent with the point at $y \sim 0$ within the statistical uncertainty. There is a possibility of a slight decline in the $\bar{p}/p$ ratio from $y \sim 0$ to $y \sim 1$. It is therefor unclear wether a plateau is present in the d+Au data.

The K^-/K^+ and $\bar{p}/p$ points at $y \sim 3$ are significantly lower than the points from p+p and Au+Au collisions. This can be attributed to a higher degree of nuclear stopping on the deuteron side of d+Au collisions compared with Au+Au and p+p collisions, in agreement with the SPS results from p+Pb collisions and the preliminary STAR data on stopping in d+Au discussed in section 2.3.4.

The p+p, d+Au and Au+Au $\bar{p}/p$ points at midrapidity are all consistent with each other. PHOBOS measurements of the centrality dependence of the $\bar{p}/p$ ratios in [35] show an indecency of centrality in d+Au collisions. This is an indication that the $\bar{p}/p$ ratio at midrapidity is not influenced very strongly by the exact degree of projectile stopping; this in contrast with NA49 measurements of Pb+Pb, p+Pb and p+p collisions at $\sqrt{s_{NN}} = 17.2$ GeV published in [49]. These results show a clear increase in the $\bar{p}/p$ -ratio with decreasing system size. It is hard to draw firm conclusions from this, but at RHIC energies the transparency is large, and most p and $\bar{p}$ around $y \sim 0$ are pair produced giving $\bar{p}/p$ near 1, while at SPS energies the midrapidity baryon content is dominated by baryon transport from both target and projectile.

8.2 Comparison to statistical model predictions

In the upper panel of figure 8.3 I have plotted the measured K^-/K^+ ratio as function of $\bar{p}/p$ from this work together with results from p+p collisions at $\sqrt{s_{NN}} = 200$ GeV [47] and $\sqrt{s_{NN}} = 23-63$ GeV [50] and S+A and p+A [51] (A signifying various target nuclei) collisions at $\sqrt{s_{NN}} = 19.4$ GeV and $\sqrt{s_{NN}} = 29.1$ GeV, respectively. The d+Au K^-/K^+ results have been interpolated to the rapidity bin of the $\bar{p}/p$ results. In the lower panel results from Au+Au and Pb+Pb collisions at energies from $\sqrt{s_{NN}} = 5$ GeV to $\sqrt{s_{NN}} = 200$ GeV are plotted in the same way for comparison.

All the $\sqrt{s_{NN}} = 200$ GeV data points are very well described by power-law functions of the form $\left(\frac{\bar{p}}{p}\right)^{\left(\frac{\mu_S}{\mu_B}\right)} = \left(\frac{\bar{p}}{p}\right)^{\alpha}$, with $\alpha = \frac{\mu_S}{\mu_B}$, as predicted in section 2.4.1. This is consistent with the behaviour expected from systems exhibiting local thermalization with μ_q (μ_B) varying strongly with rapidity and the chemical freeze-out temperature, T_{ch}, remaining approximately constant throughout the reaction zone. The fits to the $\sqrt{s_{NN}} = 200$ GeV data points yields $\alpha = 0.24 \pm 0.02$, $\alpha = 0.32 \pm 0.04$ and $\alpha = 0.34 \pm 0.05$ for the Au+Au, p+p and d+Au points respectively.

As described in section 2.4.1 the correlation between μ_S and μ_B is temperature dependent. The Statistical model predictions in [16] shown in figure 2.12 exhibit a linear dependence at low μ_B with a steeper slope indicating higher system temperature. A higher α value may therefore in this model description tentatively be interpreted as a sign of higher system temperature. A statistical model fit to the Au+Au data indicates $T_{ch} \sim 170$ MeV [52]. A curve in figure 2.12 with linear dependence $\alpha \sim 0.33$ is consistent with a temperature $T_{ch} \sim 200$ MeV . As may be seen from figure 8.3 all the Au+Au and Pb+Pb points follow the $\sqrt{s_{NN}} = 200$ GeV fit reasonably well, while the points from p+p collisions at $\sqrt{s_{NN}} = 200$ GeV and $\sqrt{s_{NN}} = 23 - 63$ GeV follow the curve corresponding to a fit to the d+Au data reasonably well. This is consistent with a systematically higher chemical freeze-out temperature in small systems

compared with the massive Au+Au and Pb+Pb collisions at high energies. A similar increase in the chemical decoupling temperature for smaller systems is also concluded in [53].

A separate fit to the Au+Au SPS data points in [44] yields $\alpha \sim 0.20 \pm 0.02$. The p+A points in the upper panel at $\sqrt{s_{NN}} = 29.1$ GeV are also situated above the curve indicating the fit to the $\sqrt{s_{NN}} = 200$ GeV d+Au data, while the ISR p+p data at $\sqrt{s_{NN}} = 23 - 63$ GeV follow the $\alpha \sim 0.34$ d+Au curve well. Although the material presented here does not allow for firm conclusions to be drawn, these are hints that the chemical freeze-out temperature increases with $\sqrt{s_{NN}}$, in particular from the SPS energy regime to the RHIC top energy. Statistical model fits to relative yields from a large selection of particle species show such a dependence of T_{ch} on $\sqrt{s_{NN}}$ [16].

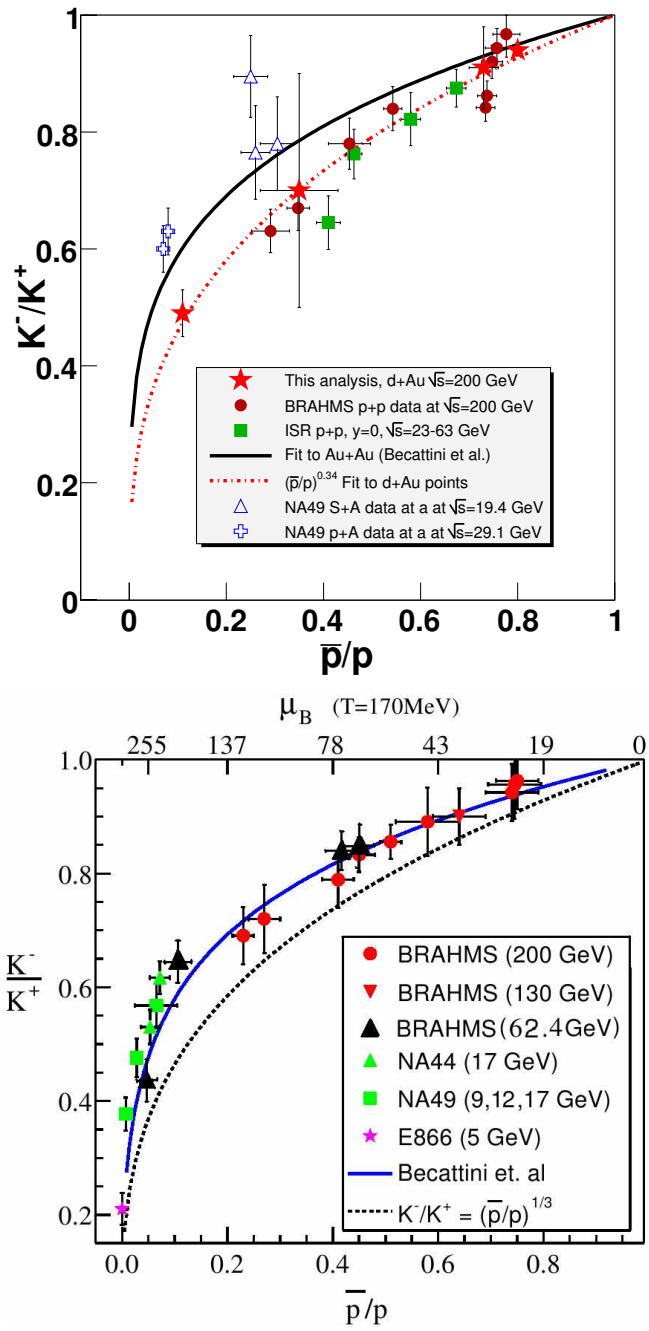

Figure 8.3: Top: The kaon ratio as function of the proton ratio results from this work with results from p+p [47] (BRAHMS) and [50] (ISR) as well as S+A and p+A collisions [51] (NA49), where A signifies various target nuclei. Bottom: Same results for Au+Au and Pb+Pb collisions. NA49 Pb+Pb points from [54, 55], NA44 data from [56], E866 data from [57], The 62.4 Au+Au points and lower panel plot from [58].

Bibliography

[1] J.C.Collins and M. J. Perry. Superdense matter: Neutrons or asymptotically free quarks? *Phys. Rev. Lett.*, 34:1353–1356, 1975.

[2] A.D.Martin F.Halzen. *Quarks & Leptons.* Wiley, 1984.

[3] Cheuk-Yin Wong. *Introduction to High-Energy Heavy-Ion Collisions.* World Scientific Publishing Co. Pte. Ltd, 1994.

[4] F. Wilczek. *Ann. Rev. Nucl and Part. Sci.*, volume 32. Annual Reviews, 1982.

[5] R. Barate et al. Studies of quantum chromo dynamics with aleph detector. *Phys. Rept.*, 294:1–165, 1998.

[6] T. R. Klassen. The (lattice) QCD potential and coupling: How to accurately interpolate between multiloop QCD and the string picture. *Phys. Rev. D*, 51:5130–5152, 1995.

[7] M. Gyulassy and L. McLerran. New forms of QCD matter discovered at RHIC. *Nucl. Phys. A*, 750, 2005.

[8] J. L. Nagle. Powerpoint presentation.

[9] D. Ouerdane. *Charged Pion and Kaon Production in Central Au+Au Collisions at* $\sqrt{s_{NN}} = 200$ *GeV.* PhD thesis, Niels Bohr Institute, 2003.

[10] I.G.Bearden et al. Nuclear stopping in Au+Au collisions at $\sqrt{s_{\rm NN}} = 200$ GeV. *Phys.Rev.Lett*, 93(102301), 2004.

[11] B. H. Samset. *Charged particle production in p+p collisions at* $\sqrt{s} = 200$ *GeV.* PhD thesis, University Of Oslo, 2006.

[12] QM2005. *F. Simon for the STAR Collaboration: Forward Lambda Production and Nuclear Stopping Power in d+Au Collisions at RHIC*, 2005. nucl-ex/0512031.

[13] S.V.Afanasiev et al. New results from na49. *Nucl.Phys. A*, 698:104–111, 2002.

[14] Zhongbao Yin. *High p_{T} Physics in Heavy Ion Collisions at $\sqrt{s_{NN}} = 200$ GeV*. PhD thesis, University Of Bergen, 2004.

[15] I.Arsene et al. Centrality dependent particle producttion a $y = 0$ and $y \sim 1$ in Au+Au collisions at $\sqrt{s_{NN}} = 200$ GeV. *Phys.Rev. C*, 72(014908), 2005. nucl-ex/0503010.

[16] P. Braun-Munzinger et al. Hadron production in Au-Au collisions at RHIC. *Phys.Lett.B*, 518:41, 2001.

[17] J.Rafalski P.Koch, B. Muller. Strangeness in relativistic heavy ion collisions. *Phys. Rep.*, 142:167–262, 1986.

[18] J. Sollfrank et al. Chemical freeze-out conditions in central s-s collisions at 200 a GeV. *Z.Phys.C*, 61:659–665, 1994.

[19] J.D.Bjorken. Highly relativistic nucleus-nucleus collisions: The central rapidity region. *Phys.Rev. D*, 27:140–151, 1983.

[20] BRAHMS Collaboration (I. Arsene et. al.). Quark-gluon plasma and the color glass condensate at RHIC? the perspective from the brahms experiment. *Nucl. Phys. A*, 757:1–27, 2005. nucl-ex/0403005.

[21] F. Karsch. The phase transition to the quark gluon plasma: Recent results from lattice calculations. *Nucl. Phys. A*, 590:367–381, 1995.

[22] T. Matsui and H. Satz. j/ψ suppression by quark-gluon plasma formation. *Phys. Lett. B*, 178, 1986.

[23] M. C. Abreu *et al.* Charmonium production in Pb—Pb interactions at 158 GeV/c per nucleon. *Nucl. Phys A*, 638, 1998.

[24] NA50 Collaboration. A new measurement of j/psi suppression in Pb-Pb collisions at 158 GeV/c per nucleon. *Eur. Phys. J. C*, 39, 1995.

[25] Thomas Vik. λ og $\bar{\Lambda}$ produksjon i bly-bly kollisjoner ved 158 GeV/c per nukleon. Master's thesis, University of Oslo, 2001.

[26] F. Antinori et al. Production of strange and multistrange hadrons in nucleus-nucleus collisions at sps. *Nucl. Phys A*, 661:130c–139c, 1999.

[27] J. Cronin et al. Production of hadrons with large transvers momentum at 200-GeV, 300-GeV, and 400-GeV. *Phys. Rev. D*, 11:3105–3123, 1975.

[28] I.Arsene et al. Evolution of the nuclear modification factors with rapidity and centrality in d+Au collisions at $sqrts_{NN} = 200$ GeV. *Phys. Rev. Lett*, 93(242303), 2004.

[29] J. Breitweg et. al. *Eur. Phys. J.*, 67:609, 1999.

[30] C. Klein-Boesing for the PHENIX Collaboration. PHENIX measurement of high p_T particles in Au+Au and d+Au collisions at $\sqrt{s_{NN}}$=200 GeV. *J.Phys.G*, 30:S975–S978, 2004. nucl-ex/0403024.

[31] M. Adamzyck et al. The brahms experiment at RHIC. *Nucl. Instr. Meth. A*, 449, 2003.

[32] C. O. E. Jørgensen. *High p_{T} Charged Hadron Production at RHIC.* PhD thesis, University of Copenhagen, 2003.

[33] H. Hahn et al. The RHIC design overview. *Nucl. Instrum. Meth. A*, 499:245–263, 2003.

[34] http://www.phenix.bnl.gov/. webpage.

[35] http://www.phobos.bnl.gov/. webpage.

[36] http://www.star.bnl.gov/. webpage.

[37] H.Appelshäuser et al. Spectator nucleons in Pb+Pb collisions at 158 a·GeV. *European Physical Journal A*, 2, 1998.

[38] http://root.cern.ch/. webpage.

[39] http://www4.rch.bnl.gov/ brahmlib/. webpage.

[40] H.Ito. *Charged-Particle Production in Au+Au Collisions at $\sqrt{s_N N} = 130$ GeV.* PhD thesis, University of Kansas, 2002.

[41] B. H. Samset. Vertex determination in the brahms experiment and measurements of centrality dependent charged particle production in Au-Au collisions at $\sqrt{s_{NN}} = 130a$ GeV. Master's thesis, University Of Oslo, 2003.

[42] F. Jundt et al. Time projection chambers for ultra-relativistic heavy-ion experiments with a mid-rapidity spectrometer. *Nucl. Phys. A*, 566, 1994.

[43] http://cernlib.web.cern.ch/cernlib/libraries.html. webpage.

[44] BRAHMS Collaboration. Rapidity dependence of charged anti-particle-to-particle ratios in Au+Au collisions at $\sqrt{s_{NN}} = 200$ GeV. *Phys. Rev. Lett.*, 90(102301), 2003.

[45] P. H. L. Christiansen. *Stopping in central $\sqrt{s_{NN}}$=200 GeV Au + Au collisions at RHIC.* PhD thesis, Niels Bohr Institute, 2003.

[46] I.G.Bearden et al. Charged meson rapidity distributions in central Au+Au collisions at $\sqrt{s_{NN}} = 200$ GeV. *Phys.Rev.Lett.*, 94(162304), 1995.

[47] BRAHMS Collaboration (I. G. Bearden et al.). Forward and midrapidity like-particle ratios from p+p collisions at $\sqrt{s_{NN}} = 200$ GeV. *Phys. Lett.*, 607:42–50, 2005. nucl-ex/0409002.

[48] B.B.Back et al. Centrality dependence of charged antiparticle to particle ratios new midrapidity in d+Au collision at $\sqrt{s_{NN} = 200}$ GeV. *Phys.Rev.C*, 70(01901), 2004.

[49] K. Kadija et al. Strange particle production in p+p, p+Pb and Pb+Pb interactions from NA49. *J. Phys. G*, 28:1675, 2002.

[50] B. Alper et al. Production spectra of $pi^{\pm}, k^{\pm}, p^{\pm}$ at large angles in proton-proton collisions in the CERN intersecting storage rings. *Nucl. Phys. B*, 100:237, 1975.

[51] H.Bøggild et al. Charged kaon and pion production at midrapidity in proton-nucleus and sulphur nucleus collisions. *Phys. Rev. C*, 59:328, 1999.

[52] F. Becattini et al. Features of particle multiplicities and strangeness production in central heavy ion collisions between 1.7A and 158A GeV/c. *Phys. Rev. C*, 64(024901), 2001.

[53] I. Kraus (for the NA49 Collaboration). System size dependence of strange particle yields and spectra at $\sqrt{s_{NN}} = 17.3$ GeV. *J.Phys. G*, 31:S147, 2005.

[54] S.V.Afanasiev et al. Energy dependence of pion and kaon production in central Pb+Pb collisions. *Phys. Rev. C*, 66(054902), 2002.

[55] J. Bächler et al. Hadron production in nuclear collisions from the NA49 experiment at 158 GeV/c·a. *Nucl.Phys A*, 661:45–54, 1999.

[56] I.G.Bearden et al. Particle ratios from central Pb+Pb collisions at CERN SPS. *J.Phys.G*, 23:1865, 1997.

[57] L.Ahle et al. Antiproton production in Au+Au collisions at 11.7A GeV/c. *Phys.Rev.Lett*, 81:2650, 1998.

[58] I.Arzene. Private communication.